Fall 2017

Preparation of Benzoxazine Monomers and Prepolymers from Continuous Reactor: Effects of Molecular Architecture on Properties

Andrew S. Frazee
University of Southern Mississippi

PREPARATION OF BENZOXAZINE MONOMERS AND PREPOLYMERS FROM CONTINUOUS REACTOR: EFFECTS OF MOLECULAR ARCHITECTURE ON PROPERTIES

by

Andrew S. Frazee

A Dissertation
Submitted to the Graduate School,
the College of Science and Technology,
and the School of Polymers and High Performance Materials
at The University of Southern Mississippi
in Partial Fulfillment of the Requirements
for the Degree of Doctor of Philosophy

December 2017

PREPARATION OF BENZOXAZINE MONOMERS AND PREPOLYMERS FROM CONTINUOUS REACTOR: EFFECTS OF MOLECULAR ARCHITECTURE ON PROPERTIES

by Andrew S. Frazee

December 2017

Approved by:

_____
Dr. Jeffrey S. Wiggins, Committee Chair
Associate Professor, Polymers and High Performance Materials

_____
Dr. Robson F. Storey, Committee Member
Distinguished Professor, Polymers and High Performance Materials

_____
Dr. Derek L. Patton, Committee Member
Associate Professor, Polymers and High Performance Materials

_____
Dr. William L. Jarrett, Committee Member
Research Associate Professor, Polymers and High Performance Materials

_____
Dr. Gopinath Subramanian, Committee Member
Assistant Professor, Polymers and High Performance Materials

_____
Dr. Jeffrey S. Wiggins
Director, School of Polymers and High Performance Materials

_____
Dr. Karen S. Coats
Dean of the Graduate School

Published by the Graduate School

ABSTRACT

PREPARATION OF BENZOXAZINE MONOMERS AND PREPOLYMERS FROM CONTINUOUS REACTOR: EFFECTS OF MOLECULAR ARCHITECTURE ON PROPERTIES

by Andrew S. Frazee

December 2017

Despite the modularity in molecular design and high-performance properties of benzoxazine thermoset chemistries, there are two primary shortcomings of benzoxazine marketability. Firstly, multifunctional benzoxazines are unfavorable for processing as they are glassy solids at ambient temperature. Secondly, benzoxazine chemistries are commercially synthesized using batch reactors, which are energy intensive and require the use of environmentally unfavorable solvents.

The purpose of the work herein is to address these shortcomings, which include:

1.) interrelationships between molecular architectures of synthesized monofunctional benzoxazine monomers and their ambient temperature physical states (i.e. liquid or solid) using molecular dynamics simulations and experimental comparisons,
2.) continuous high-shear reactor designs to synthesize high-purity benzoxazine monomers and prepolymers, and
3.) correlations between the molecular architecture and percent loading of fluorinated monofunctional benzoxazine reactive diluent isomers on the thermal and bulk mechanical properties of BPABOX networks.

In Chapters I and II, research motives and all experimental and characterization methods are provided.

Chapter III of this work involved synthesizing and simulating a library of monofunctional benzoxazine monomers varied by substituent placement and identity. Annealing simulations demonstrated a discontinuity that provided a qualitative prediction of the physical state of benzoxazine monomers. *Ab initio* calculations demonstrated that electron rich domains align with electron poor domains providing localized order within a monomeric system and a solid physical state.

In Chapter IV, a novel continuous high-shear reactor design, CHSR, for the synthesis of benzoxazine monomers and prepolymers is provided. Validated by ^{1}H NMR, the CHSR demonstrated throughputs that are 6-40x faster with improved target monomer conformation as compared to current reactor technologies. Proton NMR comparisons of monomers synthesized and purified from a batch reactor versus unpurified monomers from the CHSR demonstrated that the CHSR yields a high purity product eliminating the need for post-processing purification.

Chapter V of this work involved the preparation of benzoxazine alloys to elucidate the effects of molecular architecture and percent loading of fluorinated reactive diluent isomers on the BPABOX bulk matrix properties. Contrastingly, 49 wt.% of diluent was determined as the critical loading for an isomer effect on the cured network properties. Despite the increasing molecular weight between crosslinks with increasing diluent loading, plasticization was prevented up to 30 wt.% diluent. The added fluorine content afforded increased secondary interactions that could provide added energy

dissipation modes to toughen the inherently brittle neat BPABOX network as demonstrated via dynamic mechanical analyses and uniaxial compression results.

ACKNOWLEDGMENTS

I would like to thank my advisor Dr. Jeffrey Wiggins for all of the unique opportunities, support, and training during graduate school. As my advisor, mentor, and friend I am inspired by his superior work ethic, trustworthy character, and commitment to ensure the success of his students. Professionally, he provided me with the opportunity and freedom to grow as an independent technical contributor. Personally, Dr. Wiggins always reminded me that the definition of success is comprised of two components: work and family. Regardless of the day, time, or his schedule the doors to his office and house were always open. The support given by he and his wife, Jody Wiggins, made me feel like I was part of their family. The Wiggins family will always be my Mississippi family. Words cannot express my gratitude and I will always be thankful.

I would also like to thank my committee members, Dr. Robson Storey, Dr. Derek Patton, Dr. William Jarrett, and Dr. Gopinath Subramanian for their support throughout my research. I would especially like to thank Dr. Jinhai Yang for all of his guidance and help with reactor designs and process engineering. I would also like to sincerely thank Dr. Olivia McNair for being a mentor in my technical and professional development. You have been not only been a mentor, but also a great friend and I cannot thank you enough.

Most of this work would not be possible without the support of collaborators from the The Boeing Company, Dr. Sam Tucker and Dr. Stephen Heinz, and Cytec Aerospace Materials, Dr. Matthew Jackson, Dr. Rob Maskell, Dr. Peter Mills, Dr. Mark Harriman, Dr. Paul Cross, and Dr. Dominic Wadkin-Snaith. I would especially like to thank Dr. Matthew Jackson for being an excellent technical mentor and a great friend. Words

cannot express how thankful I am for the impact he had on my development as a scientist. I will forever be thankful.

WRG Administrative Staff, Mrs. Charlene McMillin, Mrs. Stephanie Patton, and Mrs. Nicky Harrison. These women are the heart of WRG and without them our daily operations would be impossible. Furthermore, these women and Mrs. Jody Wiggins were, and always will be, my Mississippi moms as they were always providing love, support, guidance, and motivation. I will forever be grateful.

WRG family, namely John Misasi, Brian Greenhoe, Jeremy Moskowitz, Kyler Knowles, Andrew Janisse, Xiaole Cheng, Matthew Patterson, Jeremy Weigand, and Travis Palmer, thank you for all of your support and help. The lab would not have been nearly as productive or fun without all of you. USM graduate student community, namely April Fogel, Corey Parada, Craig Machado, Doug Amato, Dahlia Amato, thank you for all of your support and making graduate school fun and full of laughter. Additionally, I am forever grateful for Hunter Cooke and Austin Maples for their support and friendship. Through the best and worst times we prevailed and I look forward to continuing our "brainstorming" sessions on the golf course.

I would also like to thank my Grandparents, Jim Collier, Sandy Collier, Brad Sowders, and Glenda Sowders, Uncles, Chris Collier and Christopher Reintz, Cousin, Sebastian Collier, and Maellen Langlois. Without your support and love over the years I would not be the person I am today. Thank you for always being there for me and giving the support needed to overcome life's obstacles.

I am especially grateful for my Parents, Kem Frazee, and Steve Frazee, and Sister, Madisyn Frazee. Words cannot express how thankful I am for the love and support you

provide daily. My parents have always been the best role models for hard work, dedication, and perseverance. In addition to your support, I believe these traits will continue fueling my journey toward achieving all of my personal goals.

Saving the best for last, I want to especially thank Farrar Langlois for believing in me and supporting me through the good and challenging times. Regardless of flood or ice storm, you and our dogs, Hank and Tess, have been by my side making life full of laughter and love. I am truly grateful and love you all very much.

DEDICATION

This dissertation is dedicated to my sister, Madisyn Frazee. Your strength, courage, and positive outlook has taught me how to persevere under the best and worst conditions. I am blessed and proud to have you as my sister.

Love,

Andy

TABLE OF CONTENTS

LIST OF TABLES

LIST OF ILLUSTRATIONS

LIST OF SCHEMES

CHAPTER I - INTRODUCTION

1.1 Background

The evolution of early mankind has been categorized into eras based on the preferred materials of choice for that time period. From the Stone and Bronze Ages, through the Iron Age and into the present, technology and innovation within materials science has been driven by mankind's need for light weight and high performance materials. In this respect, carbon fiber reinforced polymer (CFRP) matrix composites have proliferated to fulfill consumer demands for high performing, reduced-weight, ease of manufacturing, and cost-effective product portfolios. These demands can be dated back to WWII, when the development of fiber reinforced composites for reduced-weight replacement parts in metal aircrafts were a focal point of research and development in the United States.[1] Fiber reinforced polymer matrix technology is still considered in "critical to quality (CTQ)" projects focused on providing innovative manufacturing solutions and improving the product quality of current matrix and fiber benchmark standards of the aerospace industry.

Glassy amorphous high glass-transition temperature (T_g) epoxy matrices are the dominant product portfolio for thermosetting matrices in aerospace applications due to their high moduli, processability, and low-cost.[1] However, most epoxy matrices require curing agents, commonly amines and anhydrides, which have poor storage stability and can require catalysts for improved reaction kinetics favorable for processing.[2] Hence, the development of highly processable and stable matrices is a critical objective for next generation composites. Recent interest has shifted toward a potential alternative thermosetting matrix to the traditional epoxy portfolios, polybenzoxazines.

Polybenzoxazines are considered to favorably couple thermal and fire retardance properties of phenolic matrices with the modular molecular design of epoxies.[3-6] This combination renders benzoxazines, or BOX, an attractive matrix chemistry for aerospace applications. Furthermore, polybenzoxazines possess the ability to form alloys with other matrix chemistries affording tailorable physical properties and solvent-free processing, which provide the added benefit of environmentally favorable manufacturing.

This research will develop a novel platform from which BOX alloys, comprised of monofunctional and multifunctional monomers, will be synthesized and formulated via continuous chemical reactor. Our review of the scientific and patent literature revealed a significant gap of knowledge between molecular design and physical state prediction (i.e. solid or liquid). Liquid monofunctional benzoxazines are commonly used as reactive diluents to reduce the viscosity of multifunctional BOX monomers for improved processability without diluting the inherent thermal and mechanical properties. There is value in understanding how factors such as functional group identity (i.e. electron withdrawing vs. electron donating) and substitution (i.e. meta vs. para) on the monofunctional BOX affect its physical state, as well as the thermal and mechanical properties of the cured thermoset matrices is extremely valuable. In parallel, we will reduce the cost and environmental footprint of processing BOX monomers, prepolymers, and alloys thereof using a novel continuous chemical reactor design.

1.1.1 Benzoxazine Developments

Initially reported by Holly and Cope in 1944, BOX monomers are heterocyclic compounds synthesized by reacting a phenolic derivative, primary amine, and paraformaldehyde.[7] From this breakthrough came fundamental and exploratory studies

investigating BOX chemistries and applications, leading to the discovery of benzoxazines as thermosetting chemistries in the 1980's by Higginbottom.[8-15] Although advancements in BOX matrix chemistries continued to proliferate, the novelty and unique properties of benzoxazines were not realized until the 1990's by Ishida *et al.* following a thermally activated ring-opening polymerization study.[6, 16, 17] Although the ring-opening mechanism is not clearly understood, a proposed mechanism by Brunovska *et al.*is provided in Scheme 1.1.[18] The unique properties of multifunctional BOX chemistries for thermoset matrices include modular molecular design, long shelf-life, cost-effectiveness, high Tg, high modulus, good fire resistance properties, low moisture absorption, zero by-

products during cure, near-zero chemical shrinkage, and can be self-curing upon thermal activation.[2, 4-6, 19, 20]

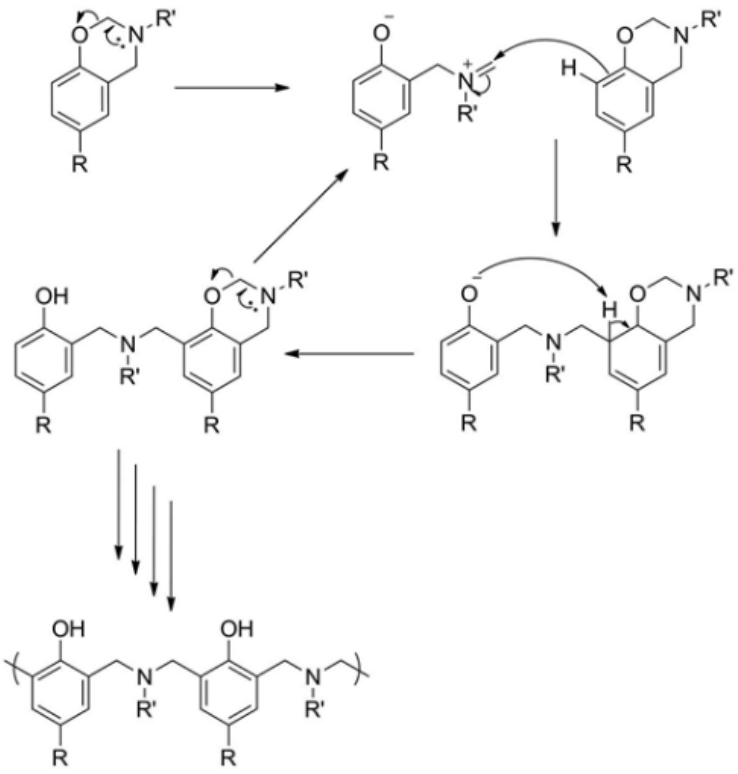

Scheme 1.1 Benzoxazine cationic ring opening polymerization mechanism.[18]

Despite the remarkable properties of multifunctional benzoxazines, their unfavorable processability is a major hurdle preventing commercialization of BOX monomers and prepolymers.

Multifunctional BOX monomers are typically glassy solid powders at temperatures below 120 °C, a common processing temperature in the production of composite prepreg materials, making them difficult to process via aerospace manufacturing methods such as filming and prepregging. Researchers focused on

improving the processability of multifunctional monomers discovered their ability to form alloys with other matrix chemistries affording tailorable physical properties and solvent-free processing. Currently, multifunctional BOX monomers blended with reactive diluents, such as epoxies, are commercially available; however the desirable properties of benzoxazines are significantly reduced by the high dilution of epoxies needed to achieve liquid physical states favorable for processing.[2, 19] Alternatively, studies by Ishida *et al.*[4, 6, 21-23] and Cytec Engineered Materials[19] focused on adding liquid monofunctional BOX monomers as reactive diluents to glassy solid multifunctional BOX monomers to improve their processability. Despite their pioneering results, nature of the interrelationship between chemical structure and physical state for monofunctional monomers has been unreported.

1.1.2 Monofunctional Benzoxazine Monomer Design

As depicted in Scheme 1.2, monofunctional BOX monomers are synthesized from a phenolic derivative, primary amine and paraformaldehyde where the amine and phenol can be substituted with electron donating and withdrawing groups. Furthermore, monomer synthesis can proceed by solution or melt techniques. The ability to use solvent-less processing methods is a key advantage for BOX matrix chemistries. However, liquid feed stocks are necessary for improved processability for their intended applications. The aforementioned studies by Ishida *et al.*[4, 6, 21-23] and Cytec Engineered Materials[19] have reported that monofunctional BOX monomers can be synthesized with solid, semi-solid, or liquid physical states at room temperature. However, an overall review of the scientific and patent literature reveals a significant gap of knowledge between molecular design and physical state prediction (i.e. solid vs. liquid) of

monofunctional BOX monomers. A Fundamental understanding of this correlation allows the use of predictive modelling (i.e. molecular dynamics simulations) to reduce the cost and time associated with synthesizing libraries of BOX monomers.

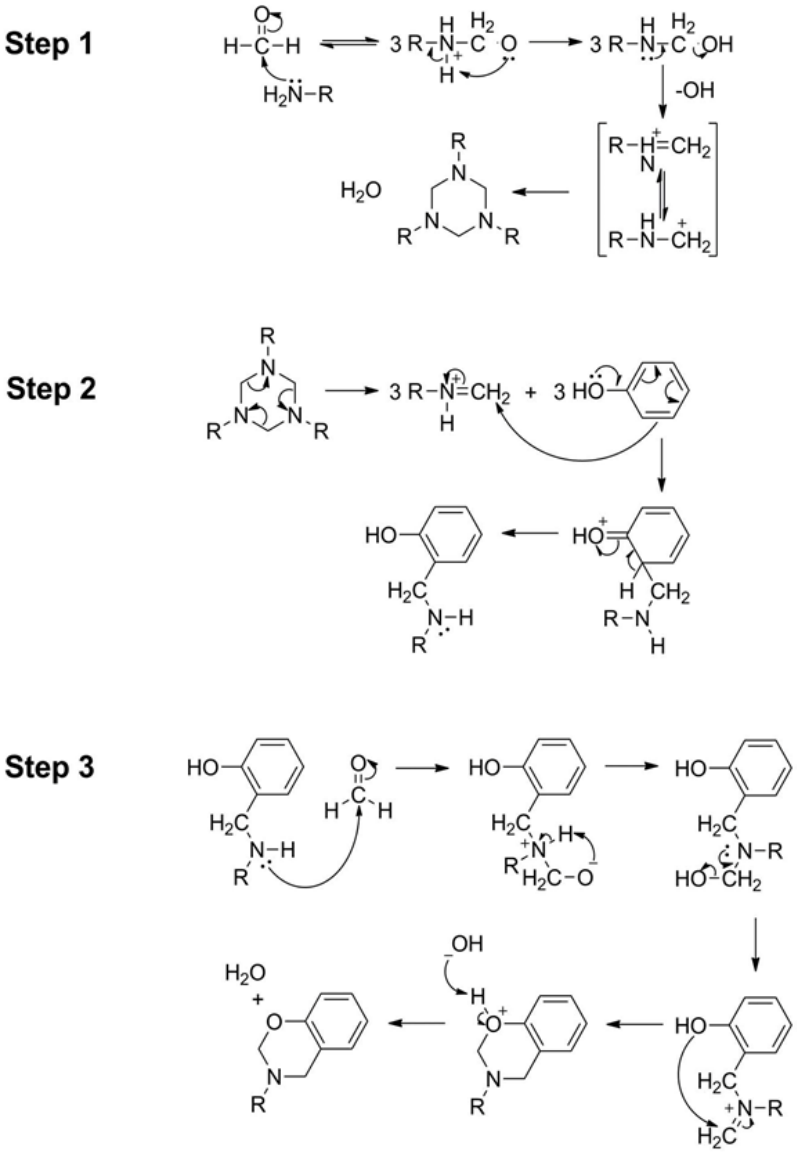

Scheme 1.2 General mechanism for benzoxazine monomer synthesis.[20]

The flexibility in molecular design afforded through substitutions about the phenolic and amine reactants provide the opportunity to logically structure monofunctional monomers and evaluate the effect of substituent species and location on the resulting physical states. Previous work by Ishida *et al.* investigated the effect of substituent type and placement on an aromatic primary amine, while keeping paraformaldehyde and 3-methylphenol constant. Results indicated that monosubstituted or disubstituted primary aromatic amines with electron donating groups in the meta-position yielded reduced-viscosities of 5.6 – 17.5 Pa·s at room temperature.[4] Patented work by Cytec Engineered Materials[19] conducted similar studies and reported that electron donating groups in the meta-position of the aromatic amine have a higher propensity of forming liquid monomers, but explanations regarding the correlation between the monomer's chemical structure and physical state were not reported. Additional knowledge regarding the effect of substituent and its location on the phenolic reactant would be useful, yet unreported. The ability to predict physical state given the chemical structure will provide pertinent information for predicative studies *via* molecular modeling and opportunities for efficient up-scaled processing designs of the studied BOX systems.

1.1.3 Continuous Chemical Reactors

With international attention of media and consumers focused on sustainability, "green" manufacturing is an area of technology that government agencies and corporations are willing to pay a premium to reduce emissions, energy consumption, and toxic waste. Batch polymerization reactors, currently used in aerospace matrix processes, are energy intensive and produce inconsistent product quality. For example,

the production of epoxy and amine prepolymers are synthesized in batch reactors. In this process, a batch reactor is charged with large volumes of monomers (epoxy and amine) and tougheners (thermoplastic) to which heat is applied to advance the molecular weight forming "b-staged" epoxy prepolymers. The prepolymers are then discharged and stored in freezers to stop reaction progression until the batch is reheated and applied as a thin film for prepreg manufacturing. The energy consumption from batch heating, sub-ambient storage, and filming results in substantial production costs. Nonetheless, elevations in direct manufacturing costs incur from batch-to-batch variations in material quality and opportunity costs from downtime and accumulated inventory during the sub-ambient storage.

Advancements in twin screw extrusion technology for thermoplastic compounding and continuous polymerization reactors have matured since the initial concepts proposed by Wunsche[24] and Easton[25, 26] in the early 1900's. As reported in the literature by Brown and Orlando[27] and Xanthos[28], process capabilities for twin screw extruders (TSE) have expanded as continuous reactors[29, 30], bulk polymerization reactors[31], polymer grafting reactors[32], and polymer blend compatibilization reactors[33]. Compared to batch reactors, the primary advantages of using continuous reactors are credited to the extruder's ability to transport a broad range of viscosities and molecular weights simultaneously. Furthermore, the absence of solvent coupled with low volume processing and high throughputs improve energy consumption affording an environmentally favorable reactive process. TSE process designs are extremely modular offering precision feeding, mixing, controlled shear energies, excellent heat transfer, insensitivity to viscosity changes, and devolatilization.[34]

1.1.4 Modular Processing Designs of Continuous Chemical Reactors

It is well documented that fully intermeshing co-rotating TSE provide the uppermost level of mixing and dispersing, which makes them a valuable component for continuous chemical reactor design.[35] Intermeshing co-rotating TSE are comprised of two identical screws (twin-screw) perfectly meshed together and enclosed within a barrel. The barrel consists of independently heated and cooled sections, or zones, that are interchangeable providing the flexible design of inlets to various liquid reactants, solid reactants and catalysts, as well as vacuum ports for devolatilization along the reactor. A common processing section of a continuous chemical reactor is annotated in Figure 1.1.

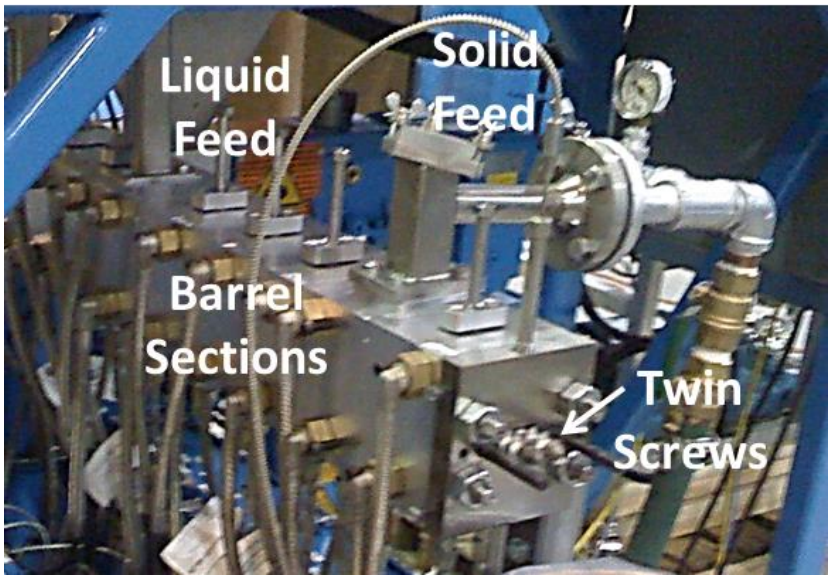

Figure 1.1 Modular components of the Wiggins Research Group continuous reactor

The screws also contain a high-level of modularity as they are designed and built using a multitude of screw elements logically sequenced to achieve effective material transport, mixing and shear.[36, 37] Examples of typical intermeshing co-rotating modular screw

elements are shown in Figure 1.2. The most common continuous reactor screw design includes conveying, high-shear mixing (kneading), and low-shear mixing (ZME) elements.

Figure 1.2 Types of screw elements for TSE

Reactor screws are designed specifically for the material and the targeted function of the process (i.e. blending, dispersing, etc.). Reactor screws are precision tolerance fit within a series of barrel sections that are independently temperature controlled.

Despite the remarkable properties and opportunities for high-volume continuous processing of BOX matrices, fundamental knowledge regarding the effect of chemical structure on physical state and the development of a platform from which BOX alloys with predictable physical properties can be designed are lacking from the current scientific literature. Furthermore, knowledge regarding the development of an environmentally favorable and cost-effective continuous reactive process from which the

aforementioned BOX monomers and alloys can be produced is missing from the scientific literature as well. There is valuable knowledge to be gained from the process design to synthesize BOX monomers and alloys in addition to identifying processing inputs to target prescribed physical states and properties.

1.2 Research Motives

1.2.1 Predicting Physical States of BOX monomers via Molecular Dynamics Simulations (Chapter III)

Benzoxazines are an attractive matrix chemistry for high performance composite applications, combining the excellent thermal stability and fire resistance of phenolic chemistries with the flexible molecular design of epoxies.[20, 38] The flexibility in molecular design is afforded through the wide range of reactants used to synthesize BOX monomers, which include paraformaldehyde and any substituted phenol and primary amine in the presence or absence of solvent. Despite the advantages of benzoxazines, their shortcoming in commercial applications result from their lack of processability as they are usually glassy solids at ambient temperatures with small differences between their melt and onset of cure temperatures.[6] These shortcomings are especially highlighted in aerospace manufacturing processes such as prepregging and resin infusion, because reduced viscosities are required to form parts prior to cure.[19]

To reduce the viscosity of glassy solids or powders for prepregging, there are two types of diluents used, reactive and non-reactive. A non-reactive diluent, such as solvent, is reactively inert and reduces the base monomer's viscosity. However, with stricter environmental regulations concerning the release of volatile organic compounds (VOC) and the post-processing difficulties of removing the solvent prior to cure, non-reactive

diluents are increasingly restrictive and cost-prohibitive.[39] A reactive diluent is a co-reactant that will reduce the viscosity and in a second function it will react with the base monomer system. The most common reactive diluents for BOX chemistries are epoxies and polyurethanes, but large dilutions are required to reduce the viscosities of multifunctional BOX monomers; therefore, the desirable properties of benzoxazines are also diluted.[19, 40] Alternatively, several studies have focused on the use of liquid monofunctional benzoxazines as reactive diluents with the aim of reducing the dilution factor needed to improve processability and preserve the desirable properties.[4, 6, 19, 21-23] However, the ambient temperature physical state (i.e. solid or liquid) of monofunctional benzoxazines varies with chemical composition and even between isomers.

Despite the findings from previous work regarding the electronic effect of substituents on the viscosity of monofunctional and multifunctional BOX monomers, explanations regarding the correlation between chemical structures and physical states of these monomers remain unreported.[4, 19] Molecular-level knowledge, obtained from predictive modeling, regarding the effect of substituent identity (coulombic charge) and orientation (ortho, meta, and para) about the phenolic reactant on the physical state of the monomer is also missing in the current scientific literature and critical to the understanding of the interrelationship between chemical structure and physical state of monofunctional BOX reactive diluents.

Molecular dynamics (MD) simulations are predictive modeling tools that enable studies of molecules in atomistic resolution. Advances in hardware technologies and experimental validations have improved the predictive capability of this method over the past few decades.[41] Several predictive studies have been reported on the reaction kinetics

of BOX monomers and structure versus property relationships of polybenzoxazines.[42] However, to the best knowledge of the author, there is no reported literature on the interrelationship between chemical structure/composition and physical state of BOX monomers. Despite the lack of literature precedent, MD simulations are based on fundamental framework. In this respect, physical state is fundamentally defined by the amount of localized order for a given experimental specimen. For example, a solid system has the most localized order and a gaseous system has the least, Figure 1.3. Monofunctional benzoxazines can either be liquids or glassy solids at ambient temperature. Glassy solids exhibit localized, or short-range, molecular order due to intermolecular interactions between molecules, but lack long range order or translational invariance.[43] The degree of order in which the monomers can achieve to form an amorphous solid are dependent on factors such as the electrostatic interactions between molecules, Figure 1.3.

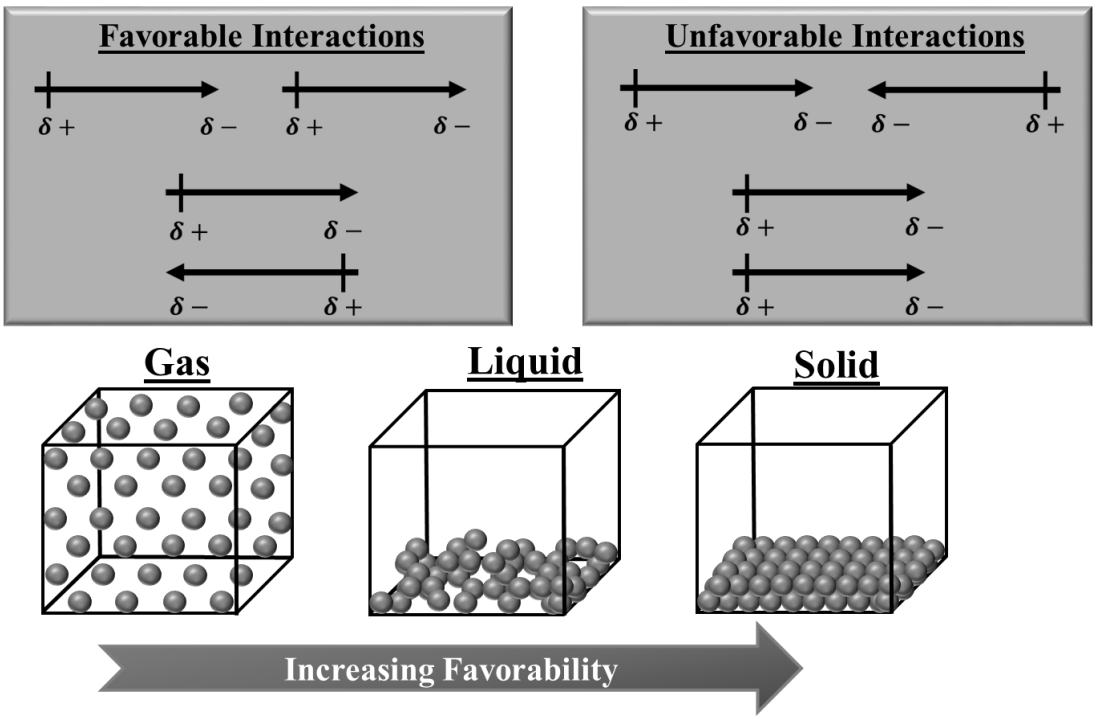

Figure 1.3 Favorable vs. Unfavorable electrostatic interactions and their effect on physical state

It is a key objective of this work to establish a predictive research tool correlating the relationship between the physical state and chemical structure/composition of monofunctional BOX monomers.

Chapter III describes *ab initio* calculations that were conducted to demonstrate the utility of molecular dynamics simulations as research tools to predict the physical state of synthesized BOX monomers. Constitutional BOX isomers, varied by the substituent identity of the phenolic reactant, were synthesized to independently investigate the effect of molecular orientation (i.e. *ortho, met*a, and *para*) and coulombic charge distribution on the monomer's physical state. Having the ability to associate chemical structure and resulting monomeric physical state provides pertinent information for predictive studies

via molecular modeling; these in turn are important for efficient up-scaled processing designs of the studied BOX systems.

1.2.2 Continuous Reactor Design for Synthesizing Benzoxazine Monomers and Prepolymers (Ch. IV)

Recent interest in high performance composites has shifted toward a potential alternative thermosetting matrix to the traditional epoxy portfolios, benzoxazines. Benzoxazines are identified by their characteristic oxazine, or heterocyclic, ring containing oxygen and nitrogen. This unique structure couples the thermal properties and fire retardance of phenolic matrices with the flexible molecular design of epoxies.[3-6] An example of the modularity in designing BOX chemical structures is depicted in the reaction in Scheme 1.3.

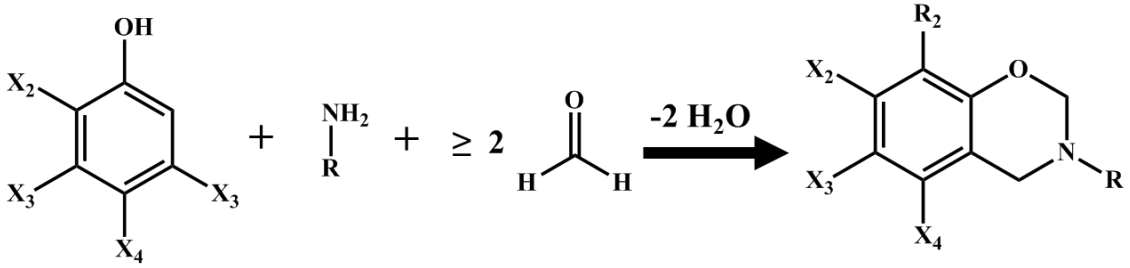

X = Electron Withdrawing Group
Electron Donating Group
H

R = Aryl, Cycloalkyl, Alkyl, or Cycloalkyl & Aryl substituted with:
- Electron Withdrawing Group
- Electron Donating Group
- H

Scheme 1.3 Reaction scheme of monofunctional BOX and various reagent combinations

The combination of molecular-level customization and high-performance properties make benzoxazines an attractive matrix chemistry for aerospace applications.

Ishida reported a method to synthesize benzoxazines in the absence of solvent, which provided an environmentally-favorable synthetic protocol.[44] Commercial polymerization reactors and processes (i.e. batch reactors) are commonly energy intensive and produce inconsistent product quality. Advancements in twin-screw extrusion (TSE) technology for thermoplastic compounding and continuous polymerization reactors have matured since the initial concepts proposed by Wunsche[24] and Easton[25, 26] Compared to batch reactors, the primary advantage of reaction extrusion is credited to the extruder's ability to transport a broad range of viscosities and molecular weights simultaneously. Furthermore, the absence of solvent coupled with low volume processing and high throughputs improve energy consumption affording an environmentally-favorable reactive process. TSE process designs are extremely modular offering precision feeding, mixing, controlled shear energies, excellent heat transfer, insensitivity to viscosity changes, and devolatilization.[34]

In Chapter IV, because the authors are synthesizing monomers from raw materials or reagents, the TSE process is named "continuous high-shear reactor" (CHSR) method. This research will demonstrate the patent pending platform whereby BOX monomers and prepolymers will be synthesized by a continuous, high-shear, solvent-free, and one-step chemical reactor providing an environmentally-favorable and cost-effective synthetic method.[45] The functionality of reagents used for each monomer and prepolymer synthesis will be reported. However, substituents of the phenol and amine in the monofunctional BOX synthesis will not be provided for the monofunctional BOX syntheses because the functional group identity had no effect on the ability to synthesize monomers in this work. Moreover, the most interesting findings were exhibited by meta-

substituted monofunctional phenols (*m*-phenol), which yielded an isomer blended monomeric product. These findings will be highlighted in the monofunctional and difunctional BOX syntheses.

1.2.3 Benzoxazine Network Architecture and Properties (Ch. V)

The attractive properties of multifunctional BOX chemistries for thermoset matrices include modular molecular design, long shelf-life, cost-effectiveness, high T_g, high modulus, good fire resistance properties, low moisture absorption, no by-products formed during cure, near-zero chemical shrinkage, and can be self-curing upon thermal activation.[2, 4-6, 19, 20] Despite the remarkable properties of multifunctional BOX, their unfavorable processability is a primary shortcoming for applications where reduced viscosities are needed during manufacturing.

Multifunctional BOX monomers are typically glassy solid powders at temperatures below 120 °C making them difficult to process in aerospace manufacturing methods (i.e. prepreg). Research focused on improving the processability of multifunctional monomers discovered their ability to form an alloy with other matrix chemistries affording tailorable physical properties and solvent-free processing. Currently, alloys comprised of multifunctional BOX monomers blended with liquid reactive diluents (i.e. epoxies) are commercially available, but the desirable properties of BOX are significantly reduced by the high dilution of epoxies needed to achieve liquid physical states favorable for processing.[2, 19] Alternatively, studies by Ishida *et al.*[4, 6, 21-23] and Cytec Engineered Materials[19] focused on utilizing liquid monofunctional BOX monomers as reactive diluents to solubilize the glassy solid multifunctional benzoxazines, thereby yielding 100% BOX liquid alloys. Despite the pioneering results

from these groups, knowledge regarding the interrelationships between loading levels and chemical structures of reactive BOX diluents on the viscosity and cured matrix properties were unreported.

In Chapter V, correlations between the molecular architecture and weight percent loading of reactive diluent isomers 6-fluoro-3-(m-tolyl)-3,4-dihydro-2H-benzo[e][1,3]oxazine versus 7-fluoro-3-(m-tolyl)-3,4-dihydro-2H-benzo[e][1,3]oxazine, or 4FBOX and 3FBOX, on the uncured rheological and cured thermal and mechanical properties of BPABOX. As the author defines a "diluent" as any non-primary component in a formulation (i.e. $\leq$ 49 wt.%), the diluent loading levels chosen for this work were 13, 30, and 49 wt.%.

The chapters presented in this dissertation are organized according to the objectives listed below.

Synthesize logically structured monofunctional BOX reactive diluent monomers.

Determine interrelationships between liquid versus solid physical states and chemical structures using molecular dynamics simulations as a research tool.

Establish solubility limitations of benzoxazine alloys comprised of monofunctional and difunctional monomers at varied diluent loadings to retain liquid physical states at ambient temperature.

Evaluate the reaction kinetics of monofunctional monomer formation and network formation of benzoxazine alloys.

Develop a continuous chemical reactor to synthesize monofunctional monomers and blend with a difunctional monomer forming alloys that can be reacted to controlled prepolymer conversions.

Correlate reactive diluent structures and loadings on properties of cured benzoxazine alloys and compare to the neat benzoxazine matrix.

CHAPTER II - EXPERIMENTAL

2.1 Materials

All chemicals used for monomer and prepolymer syntheses were used without further purification.

2.1.1 Synthetic Reagents for Monofunctional Benzoxazine Monomers

The following chemicals were used for synthesizing monofunctional benzoxazine monomers, which were screened for use as reactive diluents in this work. The paraformaldehyde powder (95%) was purchased from Sigma-Aldrich Co. The amine, m-toluidine (99%), was purchased from Fisher Chemical Co. Except for the m-cresol (99%, Sigma-Aldrich Co.), all the 4-cyanophenol (99%), 4-methoxyphenol, 3-methoxyphenol (97%), 2-methoxyphenol (≥ 98%), 4-fluorophenol (99%), and 3-fluorophenol (98%) were purchased from Fisher Chemical Co. For purification, sodium hydroxide (NaOH) beads, anhydrous diethylether, and anhydrous magnesium sulfate ($MgSO_4$) were also purchased from Fisher Chemical Co.

2.1.2 Synthetic Reagents for Difunctional Benzoxazine Monomers

The following chemicals were used for synthesizing difunctional benzoxazine monomers, bisphenol-A (≥ 99%, Sigma-Aldrich Co.), 4,4'-diaminodiphenylsulfone or 44DDS (97%, Royce Chemical Corp.), 4,4'-(1,3-phenylenedioxy)dianiline or APB134 (> 98%, Wakayama Seika Kogyo Co.), m-cresol (99%, Sigma-Aldrich Co.), m-toluidine (99%, Fisher Chemical Co.), and paraformaldehyde powder (95%, Sigma-Aldrich Co.).

2.1.3 Baseline Difunctional Monomer

The 6,6'-(propane-2,2-diyl)bis(3-phenyl-3,4-dihydro-2H-benzo[e][1,3]oxazine), or BPABOX, was used as the baseline neat matrix chemistry for all alloy formulations

and cured network studies reported in Chapter V. BPABOX was graciously donated by Huntsman Advanced Materials and is depicted in Figure 2.1.

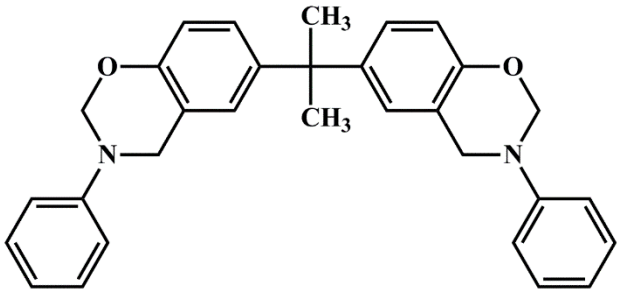

Figure 2.1 Chemical structure of BPABOX

2.2 Batch Reactor (BR) Synthetic Procedures

Syntheses of Monofunctional Benzoxazine Monomers - Batch Reactor (Chapter III & IV)

For all monofunctional benzoxazine monomer (MoBOX) syntheses, the amine (m-toluidine) and paraformaldehyde were kept constant. The phenolic reagent was varied by substituent identity and substitution, Scheme 2.1.

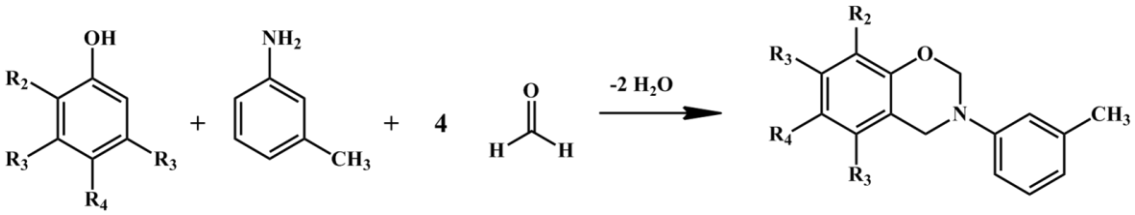

Scheme 2.1 Synthesis of monofunctional benzoxazine monomers

For these reasons, the monomers will be named according to the phenolic reagent used. For example, the monomer synthesized using 4-fluorophenol will be referenced as

4FBOX, whereas 4CyBOX was synthesized using 4-cyanophenol. The names by which all monomers synthesized in this section will be referenced herein are summarized in Table 2.1.

Table 2.1

Monofunctional benzoxazine naming, chemical structures, and physical states for Ch. III.

Monomer Name	Phenolic Reagent	Monomer Structure	Purified Room Temperature Physical State
4-CyBOX	4-cyanophenol	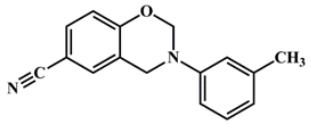	Solid
4-MBOX	4-methoxyphenol	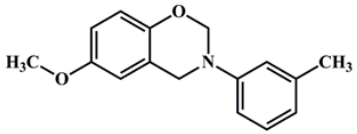	Liquid
3-MBOX	3-methoxyphenol	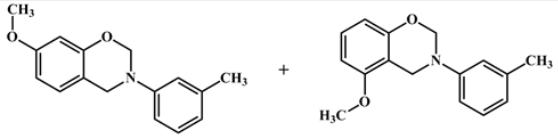	Solid
2-MBOX	2-methoxyphenol	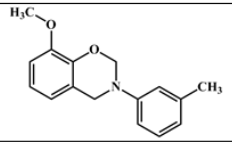	Liquid
4-FBOX	4-fluorophenol	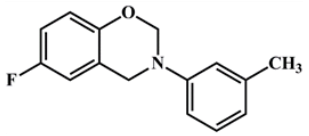	Liquid
3-FBOX	3-fluorophenol	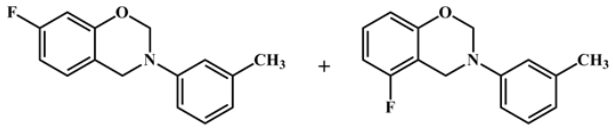	Liquid
2-FBOX*	2-fluorophenol	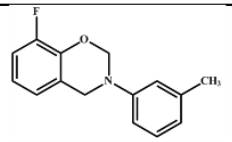	Liquid

*2-FBOX physical state was obtained from literature source[19]

The synthetic procedures listed below were based on heterogeneous BOX syntheses previously reported in the literature and their ^{1}H NMR and FTIR spectra are listed in Appendix A.[19, 44, 46, 47]

2.2.2 Synthesis of 3-(m-tolyl)-3,4-dihydro-2H-benzo[e][1,3]oxazine-6-carbonitrile, 4CyBOX

To a 50 mL glass vessel equipped with an over-head electric mixer (Arrow Electric Mixer, Model 1750), paraformaldehyde (6.006 g, 0.200 mol), m-toluidine (5.356 g, 0.050 mol), and *m*-cyanophenol (5.93 g, 0.050 mol) were charged and mixed for 30 min at room temperature to obtain a brown chalky heterogeneous mixture. The synthetic procedure was comprised of a two stage reaction. In the first stage the glass vessel was submerged in an oil bath preheated to 115 °C and reacted for 40 min. In the second stage, the temperature of the oil bath was increased to 135 °C and reacted for 20 min. Purification was accomplished by washing the crushed solid orange product with 1N NaOH and rinsing with dH_2O three times. The purified product was then dried in a vacuum oven overnight. The purified product was characterized by ^{1}H NMR spectroscopy and all aliquot concentrations were held constant at 7 m/m%. 3-(m-tolyl)-3,4-dihydro-2H-benzo[e][1,3]oxazine-6-carbonitrile, 4CyBOX: (69.3% yield) ^{1}H NMR ($CDCl_3$), ppm: δ= 2.33 (3H, s, CH_3), 4.64 (2H, s, -N-CH_2-Ar-), 5.43 (2H, s, -O-CH_2-N-), 7.04 (7H, m, aromatic). FTIR (KBr) v: Asymmetric stretching at 1240 cm^{-1} and symmetric stretching at 1178 cm^{-1} of ether bond in the BOX moiety, BOX moiety at 933 cm^{-1}, and tri-substituted benzene at 891 cm^{-1}.

2.2.3 Synthesis of 6-methoxy-3-(m-tolyl)-3,4-dihydro-2H-benzo[e][1,3]oxazine, 4MBOX

To a 50 mL glass vessel equipped with an over-head electric mixer (Arrow Electric Mixer, Model 1750), paraformaldehyde (4.004 g, 0.133 mol), m-toluidine (3.580 g, 0.033 mol), and *p*-methoxyphenol (4.136 g, 0.033 mol) were charged and mixed at room temperature for 20 min to obtain a brown chalky heterogeneous mixture. The synthetic procedure was comprised of a two stage reaction. In the first stage the glass vessel was submerged in an oil bath preheated to 115 °C and reacted for 40 min. In the second stage, the temperature of the oil bath was increased to 120 °C for 20 min. Purification of the brown or amber viscous liquid product was accomplished by dissolving the product in anhydrous diethylether. The ether solution was filtered from the precipitant, composed of ring opened dimers, into a separatory funnel. The solution was washed and rinsed three times in 100 mL portions of 1N NaOH and dH_2O, respectively. The purified product was then dried over magnesium sulfate ($MgSO_4$) to obtain a brown viscous liquid, which was filtered into a round bottom flask, and connected to a rotary evaporator to remove residual ether. The purified product was characterized by ^1H NMR spectroscopy and all aliquot concentrations were held constant at 7 m/m%. 6-methoxy-3-(m-tolyl)-3,4-dihydro-2H-benzo[e][1,3]oxazine, 4MBOX: (72.3% yield) ^1H NMR ($CDCl_3$), ppm: δ= 2.36 (3H, s, CH_3), 3.78 (3H, s, -O-CH_3), 4.64 (2H, s, -N-CH_2-Ar-), 5.34 (2H, s, -O-CH_2-N-), 6.92 (7H, m, aromatic). FTIR (KBr) v: asymmetric stretching at 1493 cm^{-1} and symmetric stretching at 1216 cm^{-1} of ether bond in the BOX moiety, BOX moiety at 947 cm^{-1}, and tri-substituted benzene at 844 cm^{-1}.

2.2.4 Synthesis of 7-methoxy-3-(m-tolyl)-3,4-dihydro-2H-benzo[e][1,3]oxazine, 3MBOX

To a 50 mL glass vessel equipped with an over-head electric mixer (Arrow Electric Mixer, Model 1750), paraformaldehyde (4.002 g, 0.133 mol), m-toluidine (3.583 g, 0.033 mol), and *m*-methoxyphenol (4.113 g, 0.033 mol) were charged and mixed at room temperature for 35 min to obtain a brown chalky heterogeneous viscous liquid. The synthetic procedure was comprised of a two stage reaction. In the first stage the glass vessel was submerged in an oil bath preheated to 115 °C and reacted for 40 min. In the second stage, the temperature of the oil bath was increased to 120 °C and reacted for 20 min. Purification was accomplished by washing the crushed solid amber product with 1N NaOH and rinsing with dH_2O three times. The purified product was then dried in a vacuum oven overnight. The purified product was characterized by ^1H NMR spectroscopy and all aliquot concentrations were held constant at 7 m/m%. 7-methoxy-3-(m-tolyl)-3,4-dihydro-2H-benzo[e][1,3]oxazine, 3MBOX: (83.9% yield) ^1H NMR ($CDCl_3$), ppm: δ= 2.30 (3H, s, CH_3), 3.72 (3H, s, -O-CH_3), 4.58 (2H, s, -N-CH_2-Ar-), 5.29 (2H, s, -O-CH_2-N-), 6.91 (7H, m, aromatic). FTIR (KBr) v: asymmetric stretching at 1492 cm^{-1} and symmetric stretching at 1197 cm^{-1} of ether bond in the BOX moiety, BOX moiety at 929 cm^{-1}, and tri-substituted benzene at 831 cm^{-1}.

2.2.5 Synthesis of 8-methoxy-3-(m-tolyl)-3,4-dihydro-2H-benzo[e][1,3]oxazine, 2MBOX

To a 250 mL glass vessel equipped with an over-head electric mixer (Arrow Electric Mixer, Model 1750), paraformaldehyde (12.413 g, 0.413 mol), m-toluidine (10.801 g, 0.101 mol), and *o*-methoxyphenol (12.513 g, 0.101 mol) were charged and mixed at room temperature for 35 min to obtain a brown chalky heterogeneous mixture. The synthetic procedure was comprised of a two stage reaction. In the first stage the

glass vessel was submerged in an oil bath preheated to 115 °C and reacted for 40 min. In the second stage, the temperature of the oil bath was increased to 150 °C for 20 min. Purification of the dark brown viscous liquid product was accomplished by dissolving the product in anhydrous diethylether. The ether solution was filtered from the precipitant, composed of ring opened dimers, into a separatory funnel. The solution was washed and rinsed three times in 100 mL portions of 1N NaOH and dH_2O, respectively. The purified product was then dried over magnesium sulfate ($MgSO_4$) to obtain a brown viscous liquid, which was filtered into a round bottom flask, and connected to a rotary evaporator to remove residual ether. The purified product was characterized by ^1H NMR spectroscopy and all aliquot concentrations were held constant at 7 m/m%. 8-methoxy-3-(m-tolyl)-3,4-dihydro-2H-benzo[e][1,3]oxazine, 2MBOX: (73.1% yield) ^1H NMR ($CDCl_3$), ppm: δ= 2.28 (3H, s, CH_3), 3.82 (3H, s, -O-CH_3), 4.60 (2H, s, -N-CH_2-Ar-), 5.41 (2H, s, -O-CH_2-N-), 6.91 (7H, m, aromatic). FTIR (KBr) v: asymmetric stretching at 1486 cm^{-1} and symmetric stretching at 1168 cm^{-1} of ether bond in the BOX moiety, BOX moiety at 932 cm^{-1}, and tri-substituted benzene at 765 cm^{-1}.

2.2.6 Synthesis of 6-fluoro-3-(m-tolyl)-3,4-dihydro-2H-benzo[e][1,3]oxazine, 4FBOX

To a 250 mL glass vessel equipped with an over-head electric mixer (Arrow Electric Mixer, Model 1750), paraformaldehyde (17.778 g, 0.592 mol), m-toluidine (15.858 g, 0.148 mol), and *p*-fluorophenol (16.628 g, 0.0.148 mol) were charged and mixed at room temperature for 35 min to obtain a brown chalky heterogeneous viscous liquid. The synthetic procedure was comprised of a two stage reaction. In the first stage the glass vessel was submerged in an oil bath preheated to 115 °C and reacted for 40 min. In the second stage, the temperature of the oil bath was increased to 120 °C and reacted

for 20 min. Purification was accomplished by washing the crushed solid amber product with 1N NaOH and rinsing with dH_2O three times. The purified product was then dried in a vacuum oven overnight. The purified product was characterized by ^1H NMR spectroscopy and all aliquot concentrations were held constant at 7 m/m%. 6-fluoro-3-(m-tolyl)-3,4-dihydro-2H-benzo[e][1,3]oxazine, 4FBOX: (76.3% yield) ^1H NMR ($CDCl_3$), ppm: δ= 2.29 (3H, s, CH_3), 4.56 (2H, s, -N-CH_2-Ar-), 5.29 (2H, s, -O-CH_2-N-), 6.90 (7H, m, aromatic). FTIR (KBr) v: asymmetric stretching at 1244 cm^{-1} and symmetric stretching at 1131 cm^{-1} of ether bond in the BOX moiety, BOX moiety at 923 cm^{-1}, and tri-substituted benzene at 860 cm^{-1}.

2.2.7 Synthesis of 7-fluoro-3-(m-tolyl)-3,4-dihydro-2H-benzo[e][1,3]oxazine, 3FBOX

To a 250 mL glass vessel equipped with an over-head electric mixer (Arrow Electric Mixer, Model 1750), paraformaldehyde (17.802 g, 0.593 mol), m-toluidine (15.583 g, 0.145 mol), and *m*-fluorophenol (16.211 g, 0.145 mol) were charged and mixed at room temperature for 35 min to obtain a brown chalky heterogeneous viscous liquid. The synthetic procedure was comprised of a two stage reaction. In the first stage the glass vessel was submerged in an oil bath preheated to 115 °C and reacted for 40 min. In the second stage, the temperature of the oil bath was increased to 120 °C and reacted for 20 min. Purification was accomplished by washing the crushed solid amber product with 1N NaOH and rinsing with dH_2O three times. The purified product was then dried in a vacuum oven overnight. The purified product was characterized by ^1H NMR spectroscopy and all aliquot concentrations were held constant at 7 m/m%. 7-fluoro-3-(m-tolyl)-3,4-dihydro-2H-benzo[e][1,3]oxazine, 3FBOX: (85.2% yield) ^1H NMR ($CDCl_3$), ppm: δ= 2.30 (3H, s, CH_3), 4.62 (2H, s, -N-CH_2-Ar-), 5.32 (2H, s, -O-CH_2-N-),

6.90 (7H, m, aromatic). FTIR (KBr) v: asymmetric stretching at 1259 cm^{-1} and symmetric stretching at 1134 cm^{-1} of ether bond in the BOX moiety, BOX moiety at 914 cm^{-1}, and tri-substituted benzene at 846 cm^{-1}.

2.2.8 Synthesis of Monofunctional Benzoxazines in Chapter IV, MoBOX

To a 250 mL glass vessel equipped with an over-head electric mixer (Arrow Electric Mixer, Model 1750), a 50 g batch comprised of paraformaldehyde (4 mol), amine (1 mol), and phenol (1 mol) were charged and mixed at room temperature to obtain a brown chalky heterogeneous solution. The glass vessel was then submerged in an oil bath preheated at 115 °C for 40 min. The temperature of the oil bath was then increased to 120 °C and reaction was progressed for 20 min and viscous light brown fluid was formed. Purification of the fluid product was accomplished by dissolving the product in 250 mL diethyl ether. The ether solution was filtered from the precipitant, composed of ring opened dimers, into a 500 mL separatory funnel. The solution was washed and rinsed three times in 100 mL portions of 1N NaOH and dH_2O, respectively. The purified product was then dried over magnesium sulfate ($MgSO_4$) to obtain a brown viscous liquid, which was filtered into a round bottom flask, and connected to a rotary evaporator to remove residual ether. The purified product was characterized by ^1H NMR spectroscopy and all aliquot concentrations were held constant at 7 m/m%. (79.1% yield)
Synthesis of Difunctional Benzoxazine Monomer - Batch Reactor (Chapter IV)

2.2.9 Synthesis of 1,3-bis(4-(7-methyl-2H-benzo[e][1,3]oxazin-3(4H)-yl)phenoxy)benzene, DiBOX

To a 250 mL glass vessel equipped with an over-head electric mixer (Arrow Electric Mixer, Model 1750), paraformaldehyde (24.287 g, 0.809 mol), *m*-cresol (21.746

g, 0.201 mol), and 4,4'-(*p*-phenylenedioxy)dianiline (29.170 g, 0.100 mol) were charged and mixed at room temperature for 40 min to obtain a brown chalky heterogeneous solution. The glass vessel was then submerged in an oil bath preheated at 115 °C for 40 min. The temperature of the oil bath was then increased to 150 °C and reaction was progressed for 40.25 min and a brown viscous liquid was formed. Purification of the fluid product was accomplished by dissolving the product in diethyl ether. The ether solution was filtered from the precipitant, composed of ring opened dimers, into a separatory funnel. The solution was washed and rinsed three times in 100 mL portions of 1N NaOH and dH_2O, respectively. The purified product was then dried over magnesium sulfate ($MgSO_4$) to obtain a brown viscous liquid, which was filtered into a round bottom flask, and connected to a rotary evaporator to remove residual ether. The purified product was characterized by ^1H NMR spectroscopy and all aliquot concentrations were held constant at 7 m/m%. 1,3-bis(4-(7-methyl-2H-benzo[e][1,3]oxazin-3(4H)-yl)phenoxy)benzene, DiBOX: (58.9% yield) ^1H NMR ($CDCl_3$), ppm: δ= 2.25 (6H, s, CH_3), 4.53 (4H, s, -N-CH_2-Ar-), 5.27 (4H, s, -O-CH_2-N-), 6.92 (18H, m, aromatic). FTIR (KBr) v: asymmetric stretching at 1240 cm^{-1} and symmetric stretching at 1178 cm^{-1} of ether bond in the BOX moiety, BOX moiety at 955 cm^{-1}, and tri-substituted benzene at 1503 and 685 cm^{-1}.

2.3 Continuous High-Shear Reactor (CHSR) Synthetic Procedures

2.3.1 Safety Considerations for Lab-Scale CHSR (Chapter IV)

Due to the toxicity and health hazards associated with the reactants for benzoxazine syntheses, all lab-scale reactor trials were conducted in a walk-in fume

hood. An annotated depiction of the lab-scale, or 16 mm, CHSR reactor design enclosed in said walk-in fume hood is shown in Figure 2.2.

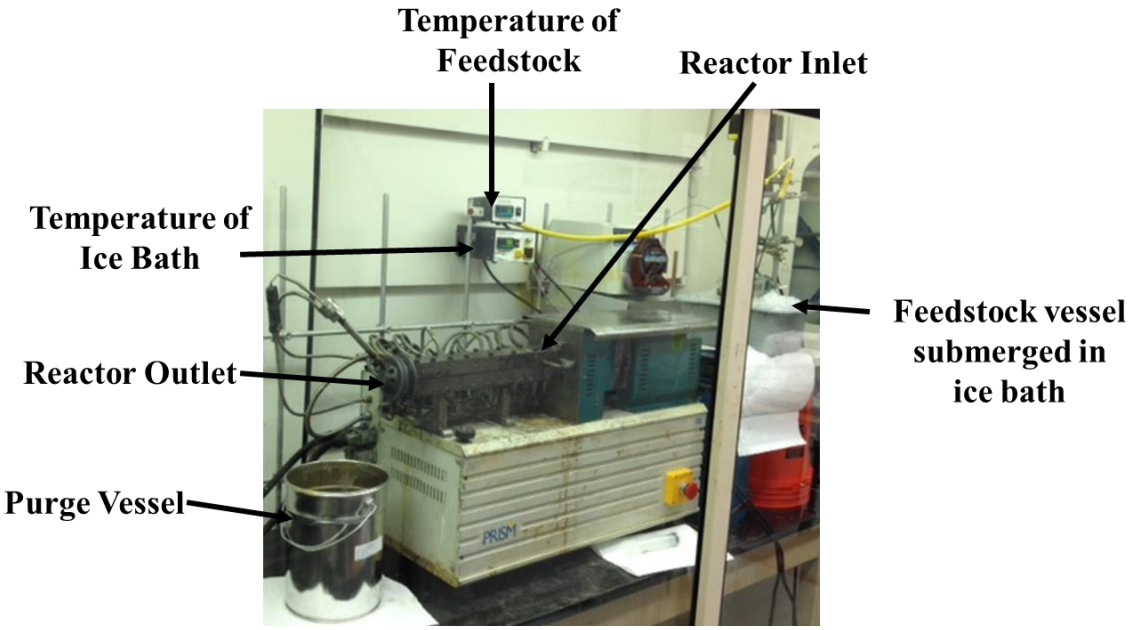

Figure 2.2 General process design of lab-scale continuous high shear reactor

Additional protective equipment (i.e. respirator and Tyvek chemical suit) and chemical detectors were used to prevent chemical exposure and monitor the concentration of chemicals in the walk-in fume hood, respectively. Said safety items and their purpose during each trial are listed in Table 2.2.

Table 2.2

Recommended safety equipment and materials 16 mm CHSR trials

Equipment	Purpose/Utilization
Respirator	Personal protection from chemical vapor
Formaldehyde Cartridges for Respirator	Personal protection from chemical vapor
Tyvek Chemical Suits	Personal protection from chemical vapor
Chemical Vapor Pump	Used for passive chemical vapor detector tubes

2.3.2 Synthesis of Monofunctional Benzoxazine Monomers – Lab-Scale CHSR (Chapter IV)

The patent pending continuous high-shear reactor (CHSR) method used for all lab-scale trials, shown in Figure 2.2, consisted of a Prism 16 mm co-rotating intermeshing twin-screw extruder (L/D = 25) and enclosed by a walk-in fume hood. The screws were enclosed by 5 zones, each independently heated and cooled. The screw design used for all 16 mm CHSR trials is depicted in Figure 2.3.

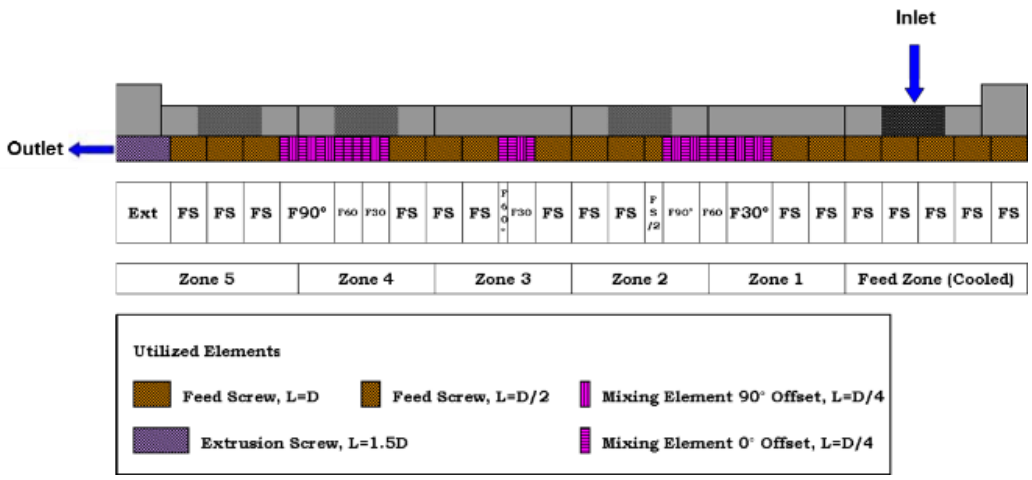

Figure 2.3 Screw design used for all lab-scale CHSR trials

The screw configuration was designed to promote the conversion of reactants to monomers by balancing high-shear mixing and residence time. High-shear mixing was isolated to three sections of the screw, as illustrated in Figure 2.3. The efficacy of transporting the feed through the reactor was qualitatively determined by the lack of agglomerated feed in the final product as well as the absence of build-up or clogs on the screws or inside the barrel of the reactor (Figure 2.4).

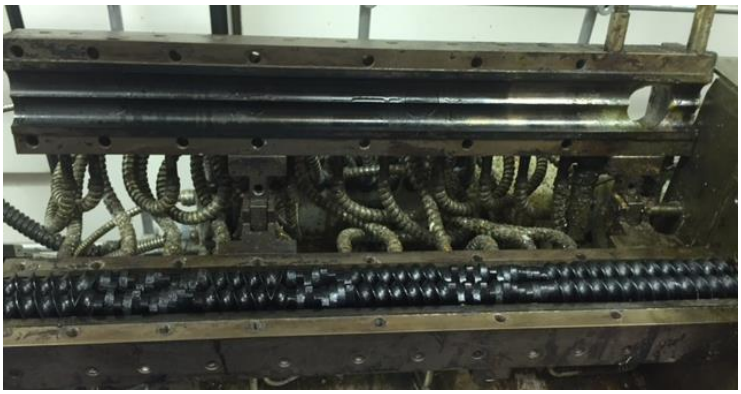

Figure 2.4 Post-trial image of the screws and inside the barrel of the 16 mm CHSR where no build-up or clogs were observed

Two methods were used to feed the reactants (i.e. phenol, amine, and paraformaldehyde) into the reactor, manual or automatic. For the manual feeding method, the paraformaldehyde (4 mol), aromatic monofunctional amine (1 mol), and phenol (1 mol) were charged at a 0.5 kg scale into a 1.0 L glass vessel that was submerged in an ice bath and equipped with an over-head electric mixer (Arrow Electric Mixer, Model 1750). After 40 min of mixing, the reaction mixture was manually pumped into the inlet of the reactor, or zone 1, using a 60 mL syringe. Due to the high viscosity of the mixture, the connection port for a needle on the syringe was hollowed to increase the inner diameter to promote a constant feed flow. The feed rate was held relatively constant at 11 g/min.

The automatic feeding method was comprised of individually feeding each reactant separately into zone 1 of the reactor. As the phenol and amine were ambient temperature liquids, they were fed individually from their original containers (Figure 2.5A & B, respectively) via peristaltic pumps (Figure 2.5C & D, respectively). The paraformaldehyde powder was charged to and fed using a volumetric solids feeder Figure 2.5E). The reactants were all fed to zone 1 of the reactor (Figure 2.5F).

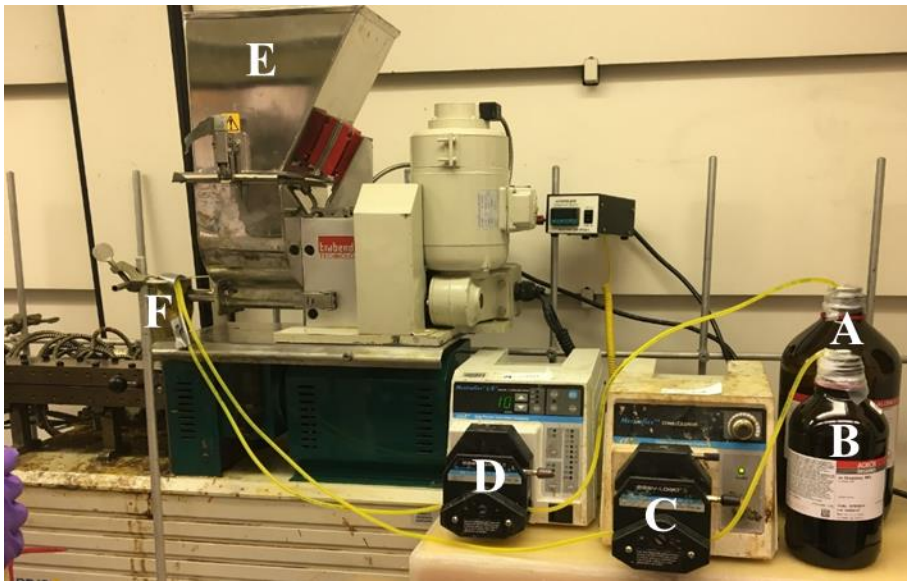

Figure 2.5 Annotated image of the automatic feed design

To ensure the targeted molar ratios of phenol (1 mol), aromatic monofunctional amine (1mol), and paraformaldehyde (4 mol) and throughput of 11 g/min were fed to the reactor, both peristaltic pumps and the volumetric solids feeder were calibrated. The calibration curves and linear feed rates and settings for the phenol, aromatic monofunctional amine, and paraformaldehyde are displayed in Figure 2.6, Figure 2.7, and Figure 2.8, respectively.

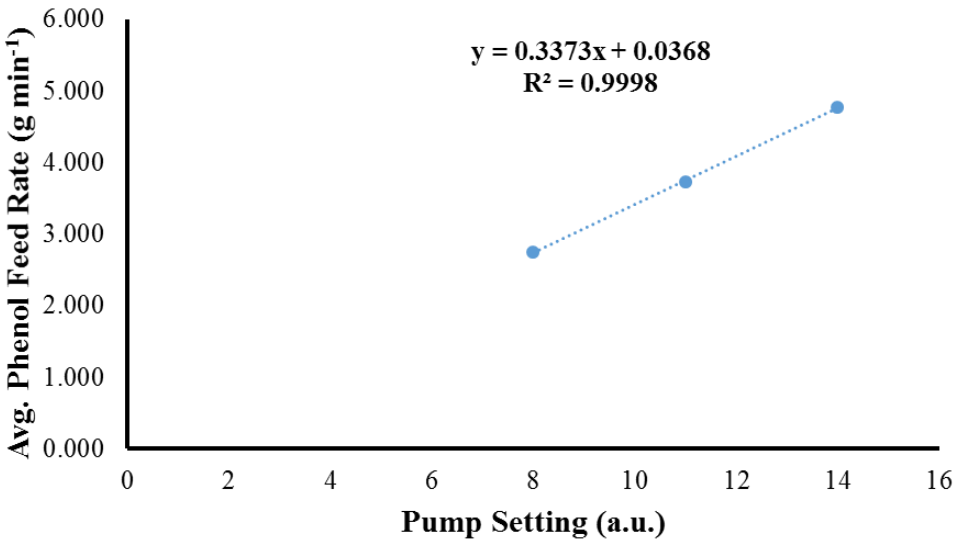

Figure 2.6 Calibration curve for the peristaltic pump of the phenol

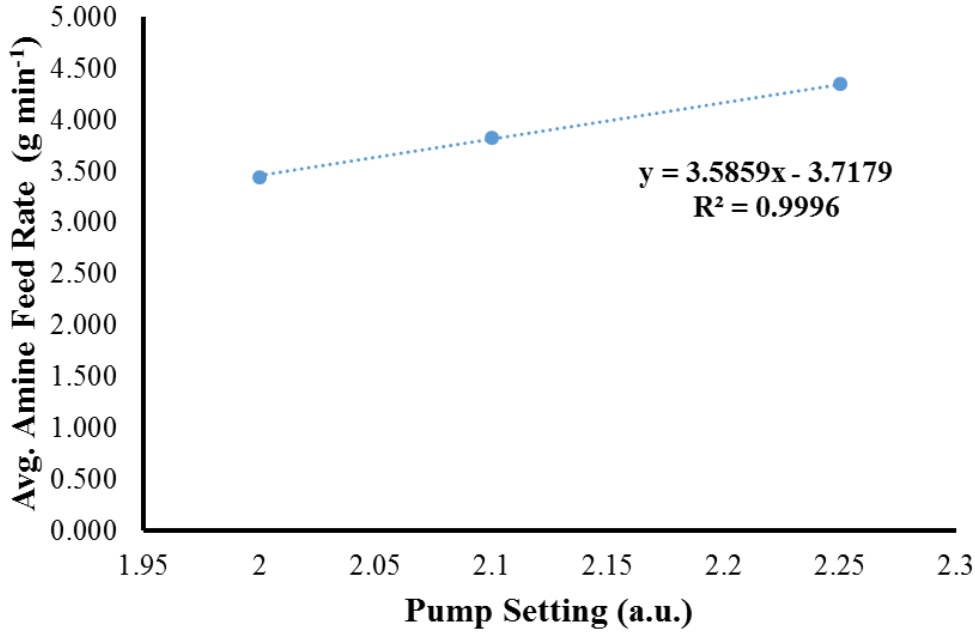

Figure 2.7 Calibration curve for the peristaltic pump of the aromatic monofunctional amine

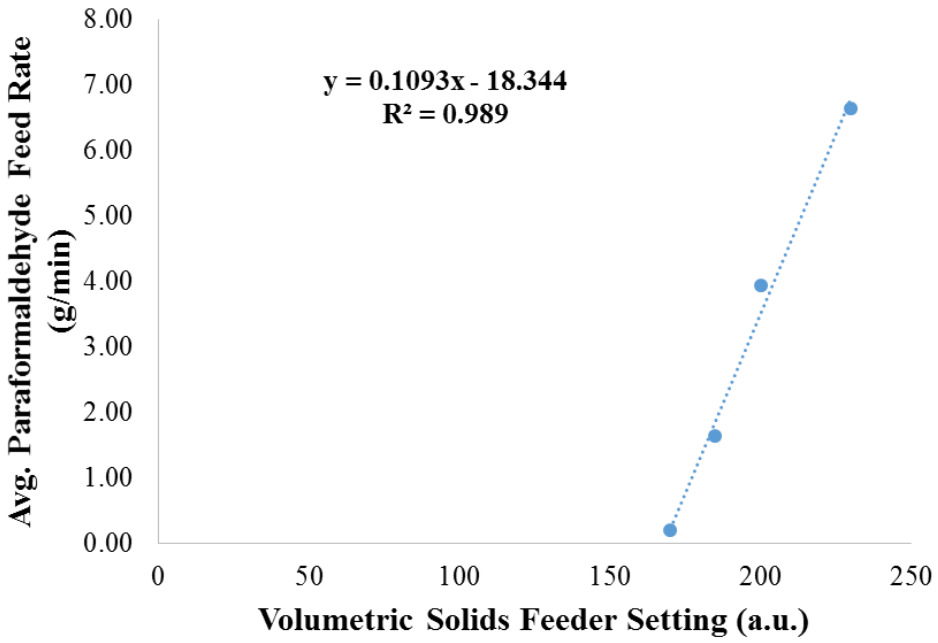

Figure 2.8 Calibration curve for the volumetric solids feeder of the paraformaldehyde

All reactants were fed, manually, or automatically, into zone 1 of the reactor, and kinetic studies were conducted by varying the processing temperatures in zones 1-5 as summarized in Table 2.3.

Table 2.3

Lab-scale CHSR processing temperatures for monofunctional benzoxazine synthesis

	Reactor Zone Temperatures per Lot # (°C)					
Zone #	**Lot 1**	**Lot 2**	**Lot 3**	**Lot 4**	**Lot 5**	**Lot 6**
1	90	90	90	90	90	90
2	90	90	90	90	90	90
3	120	140	160	180	200	220
4	120	140	160	180	200	220
5	120	140	160	180	200	220

The throughput, screw speed, and residence time were held constant at 1.5 lbs/hr, 60 rpm, and approximately 60 s, respectively. The aliquots, or Lots, collected during the trial were characterized by ^{1}H NMR spectroscopy without post-processing purification. A color change was clearly observed with increasing monomer conversion as shown in Figure 2.9.

Figure 2.9 Color change per Lot # from CHSR monofunctional BOX monomer trial

2.3.3 Synthesis of Difunctional Benzoxazine Monomer – Lab-Scale CHSR (Chapter IV)

The same patented continuous reactor design in Figure 2.2, screw design in Figure 2.3, and manual feeding method used for the monofunctional BOX syntheses were used for the difunctional BOX monomer (DiBOX) syntheses.

To a 1.0 L glass vessel that was submerged in an ice bath and equipped with an over-head electric mixer (Arrow Electric Mixer, Model 1750), paraformaldehyde (8 mol), *m*-cresol (2 mol), and 4,4'-(*p*-phenylenedioxy)dianiline (1 mol) were charged at a 0.5 kg scale. After mixing for ~ 30 min, the feed was manually pumped into zone 1. Kinetic studies were conducted by varying the processing temperatures in zones 1-5 as listed in Table 2.4.

Table 2.4

Lab-Scale CHSR processing temperatures for difunctional benzoxazine synthesis

	Reactor Zone Temperatures per Lot # (°C)					
Zone #	**Lot 1**	**Lot 2**	**Lot 3**	**Lot 4**	**Lot 5**	**Lot 6**
1	90	90	90	90	90	90
2	90	90	90	90	90	90
3	150	190	205	180	200	220
4	150	190	205	180	200	220
5	150	190	205	180	200	220

The throughput, screw speed, and residence time were held constant at 1.5 lbs/hr, 60 rpm, and approximately 60 s, respectively. The aliquots collected during the trial were amber solids and characterized by ^{1}H NMR spectroscopy without post-processing purification.

A color change was clearly observed with increasing monomer conversion as shown in Figure 2.10.

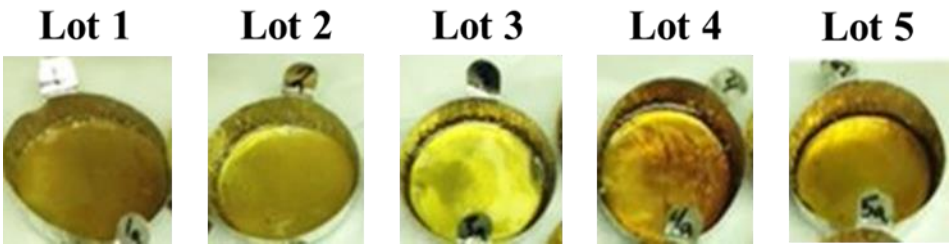

Figure 2.10 Color change per Lot # from lab-scale CHSR difunctional BOX monomer trial

2.3.4 Safety Considerations for Pilot-Scale CHSR (Chapter IV)

The safety modifications of the pilot-scale, or 26 mm, CHSR depicted in Figure 2.11 were redesigned for all pilot-scale trials to limit the chemical exposure of researchers while charging the feed vessels, running trials, and post-trial cleaning and repairs.

Figure 2.11 Recommended safety modifications for pilot-scale CHSR

An overall depiction of the reactor and primary safety modifications are depicted in Figure 2.11, image 1. The reactor can be considered a closed system except at the discharge. To address concerns of potentially releasing formaldehyde vapor into the air as material is discharged from the reactor, a fume hood was built around the discharge and plumbed directly to the snorkel hood exhaust (Figure 2.11, image 2). Additionally, it was hypothesized that formaldehyde vapor could be released from the exhaust of the vacuum pump and leak through the feed throat between the reactor and gear pump. To address these concerns, the vacuum pump's exhaust was plumbed directly to the snorkel hood exhaust and the drain of the knock out pot was plumbed directly to a sealed bucket (Figure 2.11, image 3). The feed throat between the reactor and gear pump was sealed with vacuum bag

material and tape (Figure 2.11, image 4). It should be noted that the vacuum bag material will degrade at the operating temperatures of the reactor and this modification was determined unnecessary. Lastly, there was concern with reducing the release of chemical vapor from the liquid and solid feed vessels. This was addressed by fully sealing and connecting a snorkel arm exhaust to the sealed inlet of the liquid vessel and sealing the solid vessel using vacuum bags and tape (Figure 2.11, images 5 and 6).

Additional protective equipment (i.e. respirator and Tyvek chemical suit) and chemical detectors were used to prevent chemical exposure and monitor the concentration of chemicals in the pilot plant, respectively. Building materials for the recommended safety modifications and safety items and their purposes are listed in Table 2.5.

Table 2.5

Recommended safety equipment and materials pilot-scale CHSR trials

Equipment	**Purpose/Utilization**
Respirator	Personal protection from chemical vapor
Formaldehyde Cartridges for Respirator	Personal protection from chemical vapor
Tyvek Chemical Suits	Personal protection from chemical vapor
Chemical Vapor Pump	Used for passive chemical vapor detector tubes
Chemical Vapor Detection Tubes	Monitors concentration of chemicals to rate for OSHA safety
LEXAN Fume Hood	Encloses discharge of reactor & plumbed to ventilation to contain any vapor
Aluminum Air Duct	Connected to snorkel hood exhaust to be plumbed to vacuum vent, lexan fume hood, and liquid vessel inlet
Roofing vent	Clamped to reactor and controls flow of by-product out of vacuum vent to snorkel arm
5 gal bucket	Store Liquid Vessel Material and Catch purge material at discharge of reactor
Vacuum Bag Material	Wrap completely around solid feed vessel
Vacuum bag tape	Wrap around solid feed vessel to seal vacuum bag material to vessel

2.3.5 Synthesis of Monofunctional Benzoxazine Monomer – Pilot-Scale CHSR (Chapter IV)

The patent pending continuous reactor method used in this work, Figure 2.12, consisted of a Coperion ZSK 26 mm co-rotating intermeshing twin-screw extruder (L/D = 40) and the aforementioned safety modifications for all pilot-scale trials. The screws were enclosed by 10 independently heated and cooled zones.

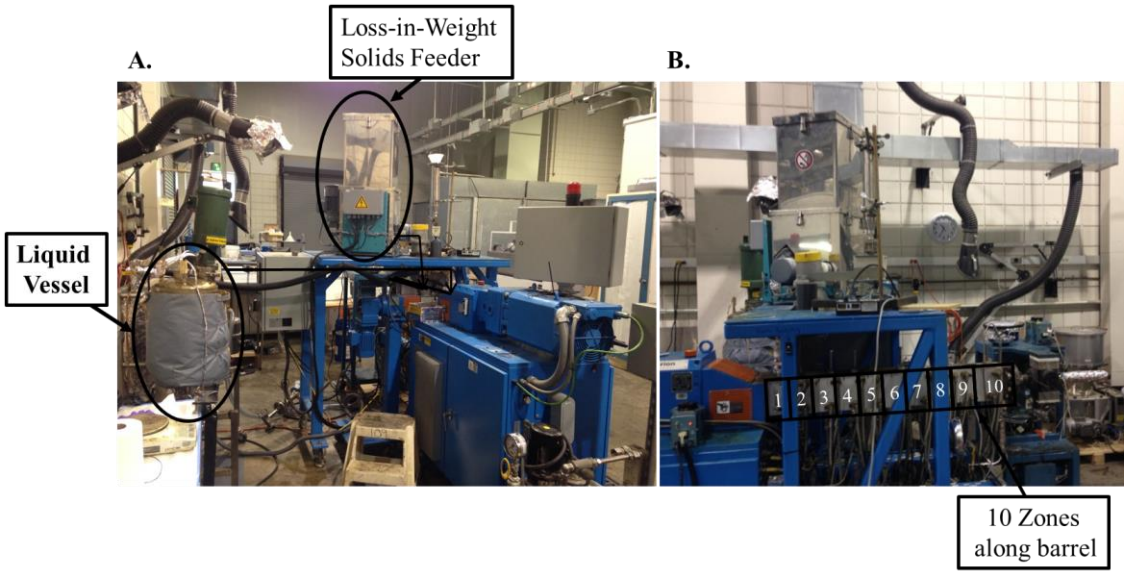

Figure 2.12 Annotated 26 mm CHSR (A.) rear and (B.) side views

The screw designs used during the pilot-scale CHSR trials are discussed in Chapter IV to highlight the influence of screw design on the reactor's ability to synthesize BOX monomers.

All feeds were charged to the reactor via automated feed systems. For example, the phenol and amine used for the monofunctional BOX synthesis were low viscosity liquids at room temperature. Therefore, they were charged at a 1:1 molar ratio and mixed

in the 10 L liquid vessel shown in Figure 2.12A. The mixed liquid feed was pumped using a precalibrated melt pump into zone 1 of the reactor, Figure 2.12B. Less than 0.5% error existed between the set and actual liquid feed rates.

The paraformaldehyde powder was charged to the loss-in-weight feeder and fed into zone 2 via a 26 mm side-stuffer, Figure 2.12A and Figure 2.12B. Powdered sugar was substituted for paraformaldehyde to calibrate and qualify the robustness of the solids feeder due to the health hazards associated with paraformaldehyde. Powdered sugar was chosen because it is lower in toxicity and has a similar bulk density to paraformaldehyde (i.e. 500-800 kg/m3). The calibration results demonstrated that less than 7% error existed between the set and actual feed rates. Moreover, the lower limit of the feeder's capability was determined to be 2 lbs/hr, as shown Figure 2.13. Additionally, it was determined that when changing the feeding rate of the solids feeder, approximately 50 seconds was needed for the feed rate to equilibrate, Figure 2.13.

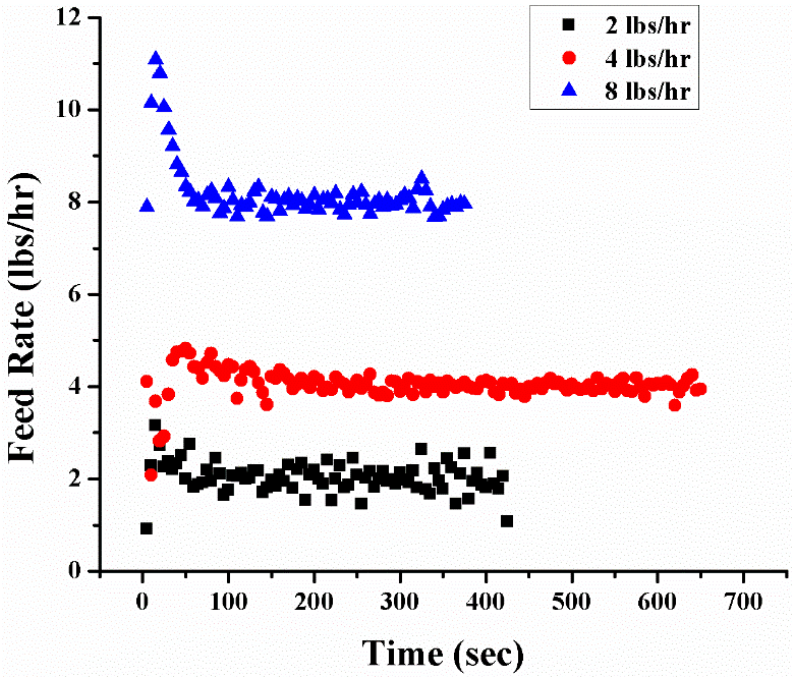

Figure 2.13 Robustness of powdered sugar feed rate

For all pilot-scale CHSR trials, the throughput was kept constant at 10 lbs/hr. Chapter IV will summarize the effect of zone temperature, screw speed, stoichiometry on conversion and purity of the product.

2.4 Preparation of FBOX/BPABOX Alloys

2.4.1 Preparation of FBOX+BPABOX Alloys (Chapter V)

Alloys were formulated by charging FBOX diluents at varied loadings (13, 30, and 49 wt.%) to 20 g of BPABOX in a 250 mL filtering flask. Since the FBOX monomers are "diluents" the authors chose 49 wt.% as the upper limit before the monomer should theoretically be considered a primary component in the formulation. Neat BPABOX, depicted in Figure 2.14, was used as the control for all analytical comparisons. Attached to the filter flask was an over-head electric mixer (Arrow Electric Mixer, Model 1750) vacuum sealed in the inlet of the neck and a vacuum pump

connected to the side-arm. The flask was submerged in an oil bath preheated to 130 °C to melt the BPABOX and overhead stirring was used to mix the formulation for ~5 min. After the formulation was solubilized, the vacuum was applied and mixing was continued for an additional 60 min to degas and devolatilize.

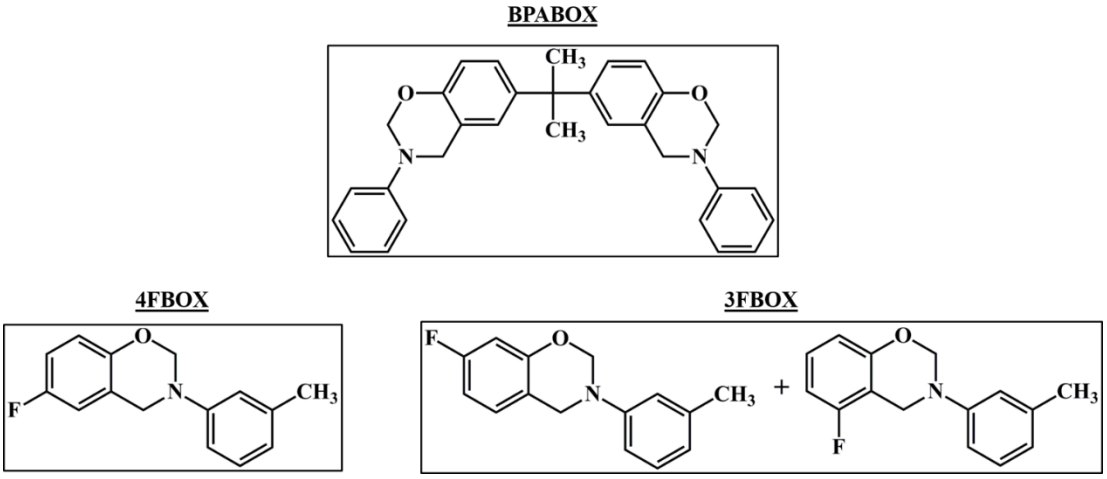

Figure 2.14 Chemical structures of BPABOX and the reactive diluents, 4FBOX and 3FBOX

2.4.2 Sample Preparation (Chapter V)

Degassed alloys were cast into silicon molds (35 mm x 5 mm x 2 mm) for DMA testing and (10 mm x 10 mm x 10 mm) for compression testing. After curing, all compression samples were machined to 7 mm x 7 mm x 7 mm cubes. Casted alloys were cured similarly to the Huntsman recommended cure prescription, which entails heating from 90 °C to 180 °C at 1 °C/min, soak at 180 °C for 2 hours, ramp to 200 °C at 1 °C/min, and soak at 200 °C for 2 hours.

2.5 Characterization

2.5.1 Proton Nuclear Magnetic Resonance Spectroscopy (^{1}H NMR)

Structural and purity validations of the synthesized monomers were obtained from ^{1}H NMR spectroscopy. Samples were dissolved in deuterated chloroform ($CDCl_3$) and a Varian Mercury Plus 300 MHz NMR spectrometer operating at a proton frequency of 300 MHz was used with tetramethylsilane added as an internal standard. The concentration of all aliquots tested in this work was held constant at 7 m/m%. Proton NMR spectra were acquired using 32 transients and a relaxation time of 7 s. For benzoxazine monomer characterizations via ^{1}H NMR, a singlet around 5.5 ppm and 4.5 ppm are representative of the protons on the two methylene linkages of the oxazine moiety (i.e. -O-CH_2-N- and -N-CH_2-Ar).

2.5.2 Attenuated Total Reflectance Fourier Transmission Infrared (ATR-FTIR) Spectroscopy

Structural validations of synthesized monomers were validated using a Thermo Scientific Nicolet 6700 with a Smart Orbital diamond crystal ATR attachment between 4,000-650 cm^{-1}. A white light source was utilized with a potassium bromide (KBr) beam splitter and DTGS KBr detector. For each spectrum, 32 scans were taken at a resolution of 2 cm^{-1} and analyses were conducted using OMNIC 7.0 Software.

2.5.3 In-situ Fourier Transform Infrared Spectroscopy (ReactIR)

All ReactIR spectra and analyses were collected using a Mettler Toledo ReactIR 45M equipped with fiber optic probe and silicon probe tip. Spectral analyses were performed using ICiR software version 4.2, which afforded reaction kinetics characteristics and reaction temperature monitoring in real-time. Sampling was conducted in the range 2800-650 cm^{-1} while acquiring 16 scans at 8 cm^{-1}. Using each reactant and a previously synthesized BOX sample as reference spectra, the ConcITt

feature calculated relative concentrations by deconvoluting peaks during the batch reactor synthesis.

2.5.4 Rheological Analyses

All rheological measurements were performed using a TA instruments ARES-G2 rheometer equipped with an 8 mm parallel plate fixture in dynamic oscillation mode at an angular frequency of 10 rad s^{-1}. Temperature ramp experiments were performed at a heating rate of 3 °C/min from 80 – 120 °C degassed and devolatilized alloys.

2.5.5 Thermal Gravimetric Analysis (TGA)

Thermal gravimetric analyses (TGA) were conducted using a TA Instruments Q50 to determine the temperatures at which each cured alloy experienced 5 and 10 wt.% mass loss, as well as, the residual char at 400 °C. All tests were performed using the same thermal profile, heating from 25 – 500 °C at a rate of 10 °C/min.

2.5.6 Differential Scanning Calorimetry (DSC)

Cured and uncured specimens from each alloy and neat BPABOX were tested via differential scanning calorimetry (DSC). Approximately 5-10 mg of degassed sample was charged to a tzero hermetic aluminum pan for all DSC measurements. Characterizations of uncured specimens were conducted by heating from 40 °C to 300 °C at a heating rate of 10 °C/min. By integrating the area under the exothermic peak, the total heat of reaction, H_T, was calculated. Cured FBOX/BPABOX samples were heated from 40 °C to 300 °C at a heating rate of 10 °C/min. By integrating the exothermic peak of each uncured specimen, H_T, to the residual cure reaction heat, H_C, of its corresponding cured alloy the degree of cure, α, was calculated using Equation 1.

$$\alpha = \frac{H_C}{H_T} * 100 \quad \text{(Equation 1)}$$

Similarly to the isoconversional analysis method reported by Anders *et al*, activation energies, Ea, were calculated as a function of conversion for all alloys, as well as neat BPABOX, using data from three distinct ramp rates: 1, 5, and 10 °C/min.[48] Although many traditional approaches cannot accurately model the reaction of complex resin formulations, an alternative, purely phenomenological method can be employed. This isoconversional method requires no specific knowledge of chemistry and only assumes that the reaction rate displays Arrhenius-type temperature dependence at all degrees of cure. To meet these requirements, a modified Arrhenius equation , as shown in Equation 2, is needed.

$$\frac{d\alpha}{dt} = A'(\alpha)e^{\frac{-E_a(\alpha)}{RT(t)}} \quad \text{(Equation 2)}$$

where

$$A'(\alpha) = A(\alpha) * f(\alpha) \quad \text{(Equation 2a)}$$

$$f(\alpha) = (1-\alpha)^n \quad \text{(Equation 2b)}$$

$$f(\alpha) = \alpha^m(1-\alpha)^n \quad \text{(Equation 2c)}$$

and f(α) in Equation 2b for nth order reactions and as in 2c for autocatalytic systems. By taking the natural log of Equation 2, Equation 3 is obtained as a linear function.

$$\ln\left(\frac{d\alpha}{dt}\right) = \ln\big(A'(\alpha)\big) - \frac{E_a(\alpha)}{RT(t)} \quad \text{(Equation 3)}$$

Therefore, by plotting $ln\left(\frac{d\alpha}{dt}\right)$ versus 1000/T of the reaction exotherm from DSC traces at various ramp rates, and applying a linear fit to corresponding α values at each rate the activation energy and modified Arrhenius factor can be extracted from the slope and

intercept, respectively. Linear fits are applied for 1000 evenly spaced increments between α=0 and α=1. An example is shown in Figure 2.15 with the fits for α=0.94, α=0.96, and α=0.98 labelled.

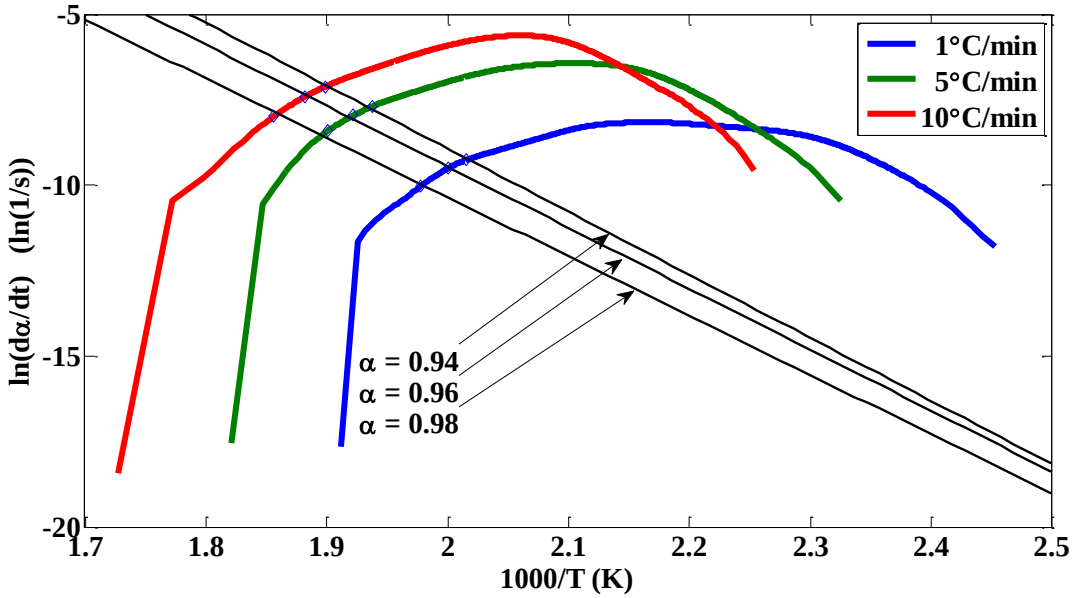

Figure 2.15 Linear fits were calculated for 1000 points between α=0 and α=1 and used to establish Ea and A' for all conversions.

Limits are defined as the onset and end temperatures of the DSC exotherm, and all reactions are assumed to occur between these temperatures. Ea and collision frequencies, A', were then plotted for all conversions and R^2 calculated from the linear fit. Fits were found to be very close, with the exception of higher conversions (i.e. α > 0.95), when diffusion limitations lead to increased error.

2.5.7 Dynamic Mechanical Analysis (DMA)

Dynamic mechanical analysis (DMA) was conducted using a TA Instruments Q800. DMA testing was performed in film tension mode with a strain of 0.05 % and a

frequency of 1 Hz. The temperature was ramped from -120 °C to 250 °C at 2 °C/min. Testing was conducted in a nitrogen atmosphere. The glass transition temperatures (T_g) were determined from the maximum of the Tanδ peak. Rubbery crosslink density (υ_e) determinations were calculated using Equation 4:

$$\upsilon_e = \frac{E'}{3RT} \quad \text{(Equation 4)}$$

where E' is the storage modulus in the rubbery region (Tg + 40 ˚C); R is the gas constant; and T is the absolute temperature (Tg + 40 ˚C).[49] It should be noted that the use of Equation 4 is a qualitative consideration because it is limited to lightly crosslinked systems. From the calculated crosslink densities and cured bulk densities (ρ), the molecular between entanglments (M_c) were caulated using Equation 5.

$$M_c = \frac{\rho}{\upsilon_e} \quad \text{(Equation 5)}$$

The activation energies (E_a) for each of the thermally-activated Tanδ transitions (i.e. α, β, and γ) were calculated from time-dependency analyses. This was accomplished using the same DMA parameters previously mentioned, except four specific frequencies (0.1, 1, 10, 100 Hz) were tested on four separate specimens and separately analyzed using Equation 6

$$log\,\frac{f}{f_0} = -\frac{2.3E_a}{\mathrm{R}}\left[\frac{1}{T} - \frac{1}{T_0}\right] \quad \text{(Equation 6)}$$

where T and T_0 are the temperatures at which frequencies f and f_0 exhibit the maximum in Tanδ and R is the universal gas constant. Lastly, activation energies for each thermal transition can be calculated from the slope of Arrhenius plots by plotting Log($\frac{f}{f_0}$) versus $\frac{1000}{T}$ for each thermal transition.

2.5.8 Monomer & Network Density Measurements

Ambient condition densities were obtained using Archimedes' Principle for solid specimen and weight per gallon for liquid specimen. Using Archimedes' Principle and a XS104 Mettler Toledo microbalance, measurements were conducted at 21 °C in air and deionized water with an accuracy of ± 0.002 g/cm^3. Weight per gallon density measurements were conducted according to ASTM D1475-98 protocol.

2.5.9 Uniaxial Compression Testing

Uniaxial compression testing was performed according to the ASTM D695 protocol using an MTS Systems Corporation Model 810 servo-hydraulic universal test frame equipped with a 15 kN load cell. Compression specimens were machined to 7 mm x 7 mm x 7 mm cubes. The specimens were tested at 25 °C using a displacement controlled test rate of 1.27 mm/min with a sampling rate of 10 Hz until a strain value of 30 % was reached. A minimum of four specimens were tested and the results averaged averaged to determine the Young's modulus and "toughness" as calculated by the area under the stress versus strain curve to 25% strain or on-set of fracture.[50]

2.5.10 Atomic Force Microscopy (AFM)

Quantitative nano-mechanical mapping (QNM) was conducted on a Bruker Dimension Icon 3000 scanning probe microscope in tapping mode at 23 °C and 50% humidity using a standard Veeco RTESP silicon probe (cantilever length, 125 μm; nominal force constant, 40 N/m; and resonance frequency, 350 kHz). Height and phase images were collected simultaneously. One cryo-fractured surface from each formulation was studied, and at least three macroscopically separated segments of the surface were

analyzed (representative images are shown). All image processing was conducted via Nanoscope version 5.30 r2 image analysis software.

2.6 Molecular Dynamics Simulations (Chapter I)

The monofunctional benzoxazine (BOX) monomers used in this work are depicted in Figure 2.16. Monomers were varied with respect to the functional group identity and substitution on the phenolic portion of each monomeric structure.

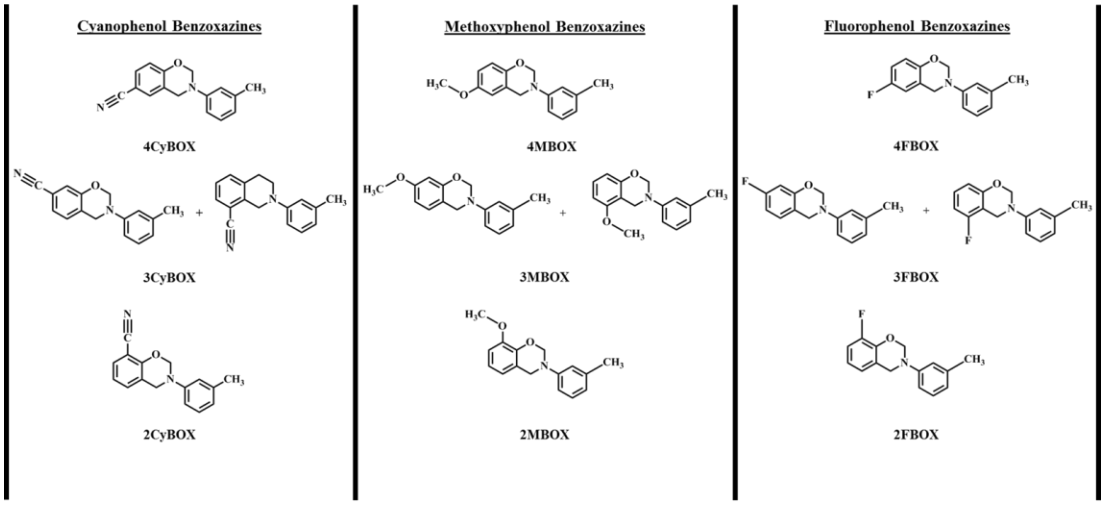

Figure 2.16 Chemical structures of simulated monofunctional benzoxazine monomers

To determine the confidence in the simulated results, comparisons were made to the synthesized monofunctional benzoxazine monomers 4CyBOX, 4MBOX, 3MBOX, 2MBOX, 4FBOX, and 3FBOX.

2.6.2 Simulation Methods (Chapter I)

Molecular simulations and graphical displays were generated on a 96-core Linux cluster using Materials Studio® v8.0 software from Dassault Systèmes BIOVIA Corp.[51]

The *ab initio* calculations were performed using the DMol[3] program. All energies and interatomic forces were calculated using the proprietary COMPASSII forcefield and "Medium" quality setting, while temperature was controlled by the Andersen thermostat and where applicable the pressure was controlled with the Parrinello barostat.[52,53]

For each BOX monomer, a Dynamic calculation using a NVT ensemble and Nosè-Hoover-Langevin thermostat[54] was conducted on the 300 K annealed cells by individually running each cell through a series of 250,000 time steps of 1 fs and a dynamic time of 250 ps yielding 100 frames to generate trajectory files (1 frame captured every 2,500 steps).

CHAPTER III – CORRELATING MOLECULAR ARCHITECTURE TO PHYSICAL STATE VIA MOLECULAR DYNAMICS SIMULATIONS

3.1 Abstract

Liquid monofunctional benzoxazines, utilized as reactive diluents, can improve the processability of glassy solid multifunctional benzoxazines. However, their physical state can vary as a solid or liquid when their molecular architecture is varied between isomeric configurations. Through the use of molecular dynamics simulations, this chapter of work attempts to develop a correlation between molecular architecture and physical state of monofunctional benzoxazine monomers for use as a predictive molecular design research tool. *It was hypothesized that room temperature liquid benzoxazine monomers are formed when a meta-substituted phenol is used to synthesize a benzoxazine isomer blend that can disrupt localized order*.

To elucidate the interrelationship between molecular architecture and physical state, a library of monofunctional benzoxazine monomers was synthesized. These monomers were varied only by the substituent placement (i.e. *ortho*, *meta*, and *para*) and substituent identity (i.e. nitrile, fluorine, and methoxy) according to heterogeneous syntheses reported in the literature.[19, 44, 46, 47] Using molecular dynamics simulations as a research tool and complemented with experimental observation and validations, correlations between the molecular architectures and physical states of synthesized monomers were established. Annealing simulations demonstrated a discontinuity in coefficient of thermal expansion and provided a qualitative prediction of the physical state of benzoxazine monomers. *Ab initio* calculations demonstrated that at ambient temperature electron rich domains align with electron poor domains between neighboring monomers, which

provide localized order within the monomeric system and a solid physical state. Results from this work were used to down-select the reactive diluents for use in Chapter V to demonstrate the effect of molecular architecture and loading level of reactive diluents on the bulk network properties.

3.2 Simulation Results & Discussion

3.2.1 Validation of Simulation Parameters for Annealed Cells

For each monofunctional benzoxazine reactive diluent in Figure 2.16, five random configurations of each BOX monomer (approx. 4,500 atoms) was loaded into a periodic cell using the Amorphous Cell module within Materials Studio. Each configuration was geometry optimized and the three lowest energy cells were selected for further analysis (i.e. RDF, MSD, and electron density mapping). Said geometrically optimized unit cells were then annealed from 600 – 10 K in 10 K increments. A strict density convergence criteria was used at each temperature before the system could cool to the next temperature.[55] At 300 K the simulation will output a "300 K annealed cell" or the most energetically favored, relaxed, and unstrained system. To validate that the simulation parameters were properly chosen to afford the most accurate results possible, the simulated room temperature densities of each BOX monomer were compared to the experimentally measured room temperature densities of the synthesized monomers. Since the present work will focus primarily on 4CyBOX and 4MBOX, the data in Table 3.1 confirmed that the room temperature simulated densities only deviated 2% from the experimental measurements, which provides substantial confidence in the analyses and conclusions made from these simulations.

Table 3.1

Simulated and experimental room temperature densities of benzoxazine monomers

BOX Monomer	Simulated Avg. Density (g/cm^3)	Simulated Density Standard Deviation (g/cm^3)	Experimental Avg. Density (g/cm^3)	Experimental Density Standard Deviation (g/cm3)	Percent Difference (%)
4CyBOX[a]	1.1579	0.0007	1.1332 [a]	0.0051[a]	2.18
4MBOX[b]	1.1479	0.0016	1.1462 [b]	0.0004[b]	0.15

*All simulated and experimental results were measured in triplicate for statistical analyses. The standard deviation values are 1 standard deviation of the mean.

a. Experimental densities were measured at room temperature via Archimedes' Principle method

b. Experimental densities were measured at room temperature via Weight per Gallon method

3.2.2 Physical State Prediction

Outputs from the annealing simulations included density values as a function of the anneal temperatures for each amorphous cell. The averaged density values were plotted versus the anneal temperatures and analyzed using a bi-linear fit to identify the discontinuity, Figure 3.1.

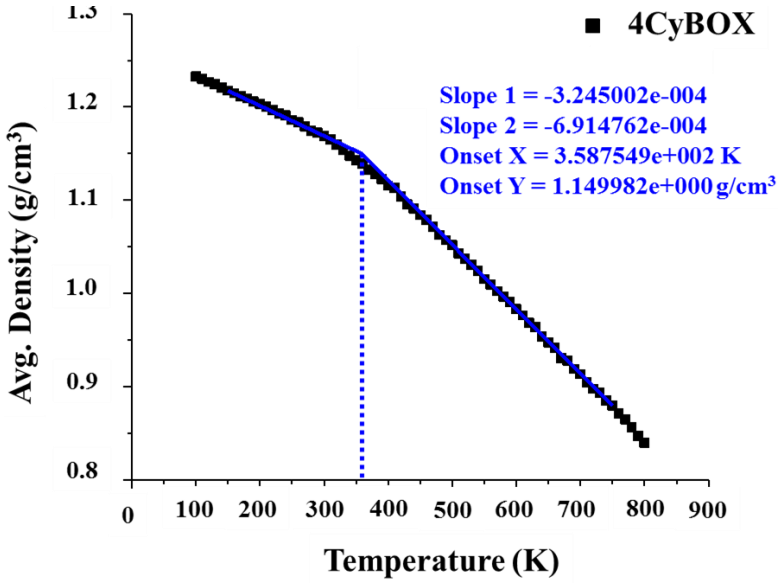

Figure 3.1 Averaged density versus temperature values of 4CyBOX annealed in triplicate

The discontinuity is a common method in molecular dynamics to predict the glass transition temperature of amorphous polymers.[56, 57] However, it was found that the discontinuity provided a qualitative prediction of the physical state for the monomeric systems reported in this work. For example, if the discontinuity was below room temperature (i.e. 300 K) then the monomer system was assumed to be a liquid; whereas, above room temperature the monomer system was assumed to be a solid. This method appears to be applicable to the BOX monomers because of their amorphous nature, even in the solid state.

To determine the efficacy of using the discontinuity points obtained from annealing simulations to predict the physical state of BOX monomers, the observed physical states of synthesized monomers are compared to their simulated discontinuity, Table 3.2.

Table 3.2

Simulated and experimental physical states of benzoxazine monomers

BOX Monomer	Avg. Simulated Discontinuity (°C)	Simulated Physical State	Experimental Physical State
4CyBOX	85.61 ± 9.31	Solid	Solid
4MBOX	28.73 ± 9.69	~ Liquid	Viscous Liquid
4FBOX	29.18 ± 9.95	~ Liquid	Viscous Liquid
3FBOX	3.32 ± 2.54	Liquid	Viscous Liquid
2FBOX	3.32 ± 2.77	Liquid	Viscous Liquid

*All simulated and experimental results were measured in triplicate for statistical analyses. The standard deviation values are 1 standard deviation of the mean. All experimental physical states were recorded at room temperature.

Traditionally, said discontinuities have been reported for polymeric systems as T_g values, which are associated with the torsional degrees of freedom (chain stiffness) that are dependent on the nonbonded Lennard-Jones potential (i.e. dipole-dipole, dipole-induced dipole, and London interactions).[58] This concept can be applied to the monomer systems herein as the intermolecular forces of attraction and repulsion were varied based on the phenolic substituent identity, which yields variations in localized order between monomers within a simulated cell. For example, the simulated density, Table 3.1, and discontinuity, Table 3.2, of 4CyBOX is higher than 4MBOX providing evidence that stronger intermolecular attractions are present in 4CyBOX affording a more ordered system and justification for the simulated prediction of a solid physical state. The simulated predictions of physical states for each constitutional isomer in this work

exhibited no trend with respect to molecular orientation as shown by comparing 4FBOX, 3FBOX, and 2FBOX in Table 3.2. However, more insight regarding the interrelationships between the monomers and their simulated predictions were needed.

3.2.3 Radial Distribution Function Analyses

Since the physical state of the monomers in this work correlated to the discontinuities from the anneal simulations, the next phase of work was to determine why their physical states varied. Fundamental understandings of solids and liquids are defined as systems of localized order and disorder, respectively. Localized order can be simulated to obtain a quantitative evaluation that is computed via the radial distribution function (RDF). Figure 3.2A is comprised of a system of molecules within an amorphous cell at time step, t_n.The RDF, or $g(r)$, is computed by Equation 7

$$g(r) = \frac{1}{4\pi r^2 \rho_{bulk} N N_t} \sum_n^{N_t} \sum_{i=1}^{N} g_i(r, t_n) \qquad \text{(Equation 7)}$$

where one molecule, i, is labeled at its center of mass, which is defined as the origin. Around the origin a sphere is drawn with a radius, r. This computational analysis is not restricted to one molecule in a system as represented in the simplified pictorial description show in Figure 3.2A, but rather to every molecule i in the system from 1 to N, where N is the total number of molecules is included. Consequently, the number of molecules whose centers of mass lie within said sphere are computed by $g_i(r, t_n)$.[59, 60] The results are averaged over each time step of the simulation, N_t, and molecule, and then normalized by the bulk density, ρ_{bulk}. The output of this analysis is a plot of $g(r)$ versus r averaged over the entire system, Figure 3.2B, which represents the probability

that one molecule's center of mass will find another particle's center of mass at distance, r, away.[61]

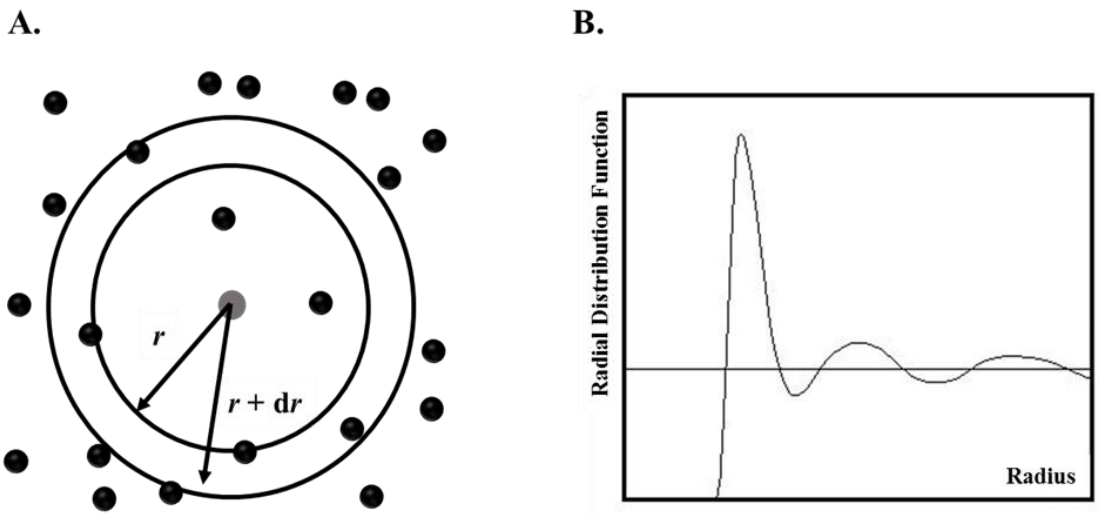

Figure 3.2 Pictorial representation of radial distribution function calculation and graphical output[61]

At short distances, r, of 1-3 Å the probability of finding another origin is essentially zero as this is typically the size of most atoms or molecules.[62, 63] At distances greater than 3 Å, definitive peaks and troughs are apparent in the RDF versus r plot, Figure 3.2B. Peaks are representative of molecular-level packing or localized ordering of the centers of mass at a certain distance, r. This defines a systems as a solid.[64, 65] In the case of a gas, no regularity between the centers of mass will be present; therefore, only one coordination event will be detected and it will rapidly decay to the ρ_{bulk}, or $g(r)$=1.[62, 63] Lastly, the intermediate of these trends defines a liquid system, when broadening distributions of coordination with increasing distance r are representative of a less ordered and more diffusive system.[62, 63] For each monofunctional BOX diluent in

Figure 2.16, three repeats of the room temperature annealed and most thermodynamically favored cell were averaged and plotted. The focus herein will be narrowed down to FBOX constitutional isomers, 4CyBoX, and 4MBOX as these systems demonstrated the most interesting results.

Upon synthesizing the FBOX monomers, it was found that regardless of the fluorine substitution on the phenol all monomers were liquids at room temperature. Comparing these observations to their RDF results stacked in Figure 3.3 and Figure 3.4, it is difficult to draw definitive conclusions with respect to the accuracy of the simulation results. For example, in Figure 3.3 the overlaid RDF peak max for 2,3, and 4-FBOX trends closer to 1, around 3-5 Å, and then quickly decays to $g(r)$=1. Quantitatively, this trend is similar in behavior to a gas which is not accurate as these systems were liquids at room temperature.

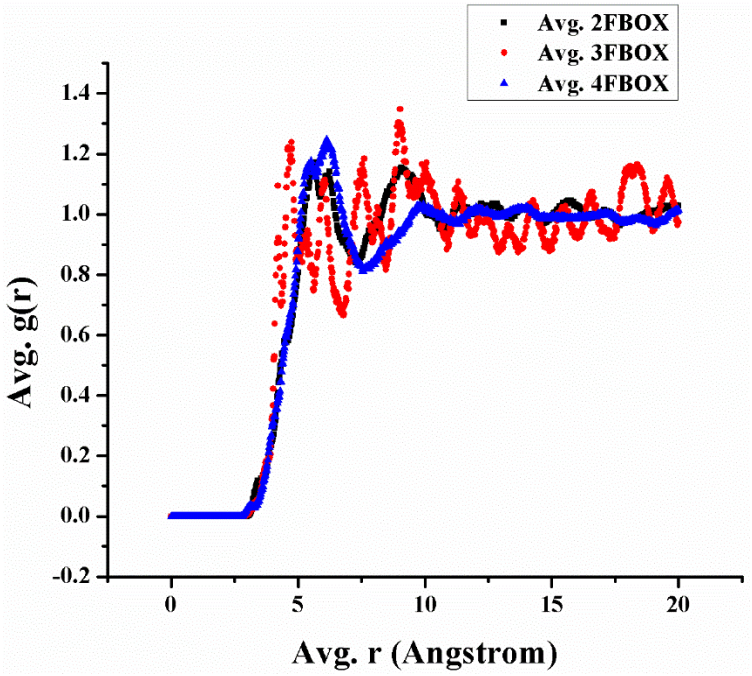

Figure 3.3 Averaged RDF results overlaid for the liquid FBOX constitutional isomers. Averaged data was collected for 3 replicates.

Qualitatively, the stacked trends in Figure 3.4 that are offset to view their peak shapes provide evidence that the RDF values could represent the physical state of these monomers as the 2FBOX and 4FBOX monomers were of lower viscosity than 3FBOX at room temperature. In this respect, the 3FBOX peak shape contains the most peaks, which is indicative of the localized order. Contrastingly, the 2FBOX and 4FBOX trends have broader peaks that is indicative of a more diffusive behavior or a liquid.

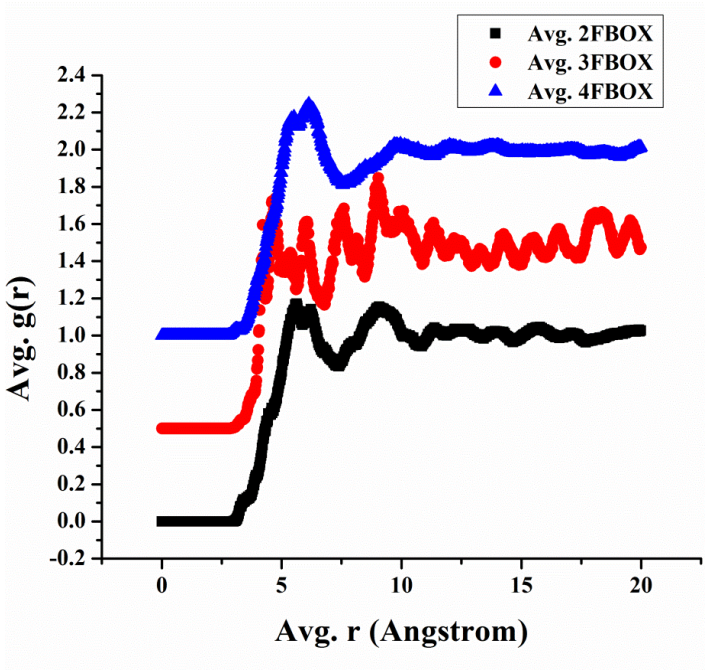

Figure 3.4 Averaged RDF results stacked for the liquid FBOX constitutional isomers. Averaged data was collected for 3 replicates.

Although the qualitative observations could be predicting the physical state, there is not a quantitative reasoning to defend this analysis. This shortcoming is believed to be well explained when comparing the RDF results for 4CyBOX, solid at room temperature, and 4MBOX, liquid at room temperature, as shown in Figure 3.5A and Figure 3.5B, respectively. Overall, the 4CyBOX contains broader peaks, similar to a liquid, and the 4MBOX has sharper peaks like a solid. Since the experimental observations prove that the simulated analyses are not accurate, it is believe that low resolution in the simulations are a cause of said discrepancies. RDF analyses are well reported in the literature, but often times they are only utilized for crystalline systems or systems with well defined regularity.[63, 66, 67]

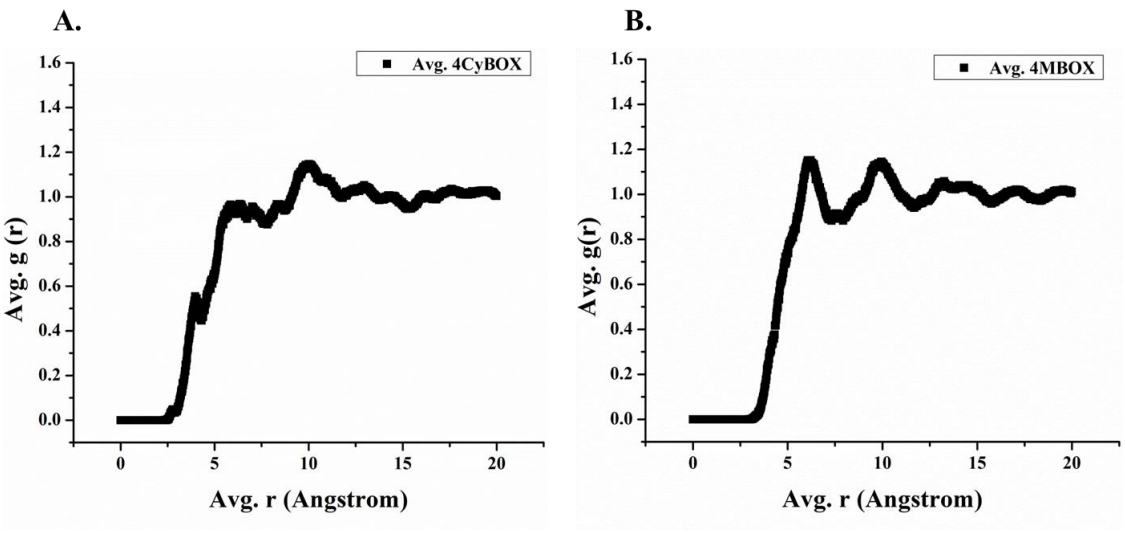

Figure 3.5 Averaged RDF results for solid 4CyBOX versus liquid 4MBOX. Averaged data was collected for 3 replicates.

It is believed that the lack of definition in the obtained curves could also be attributed to insufficient data collection. Larger systems and longer simulation times would likely reduce variability and produce more defined RDF curves. Future work will include rerunning the RDF calculations on more updated hardware with more computational ability. Moreover, the radial distribution may not be the most effective analysis method since these systems are considered to be mainly glassy amorphous solids. Sharp peaks and order in RDF calculations are better represented by systems with a crystalline lattice.[63] Additional computational analyses are available to characterize diffusive and non-diffusive characteristics at a molecular-level such as the mean square displacement (MSD).[68]

3.2.4 Mean Square Displacement Analyses

The mean squared displacement function, $\langle \Delta^2 r(t) \rangle$, is computed by the Equation 8

$$\langle \Delta^2 r(t) \rangle = \frac{1}{N} \sum_{i=1}^{N} \langle [R_i(t) - R_i(t=0)]^2 \rangle \quad \text{(Equation 8)}$$

where the diffusion of molecules, N, in a system is defined as the distance they are able to move from their initial position over a certain time period, $\Delta R^2(t)$.[69, 70] As derived by Einstein, the MSD contains information on the diffusion coefficient, D, as shown in Equations 9-10.[71, 72]

$$D = \lim_{n \to \infty} \frac{1}{6t} \langle r^2(t) \rangle \quad \text{(Equation 9)}$$

$$D = \frac{k_B T}{\gamma} \quad \text{(Equation 10)}$$

When the MSD is plotted versus time, as shown in Figure 3.6, the diffusion coefficient can be obtained from the slope at long times due to the linear time dependency of correlation times among molecules in the system. The difference between a solid and liquid is clearly defined by said linear behaviors. For example, a solid is comprised of regularity and localized order resulting in only small amplitude particle vibrations and ultimately no kinetic energy or diffusive behavior and results in a slope of zero, D=0.[68, 71] Contrastingly, liquid systems contain collisions between molecules and demonstrate a Brownian motion behavior.[68, 71]

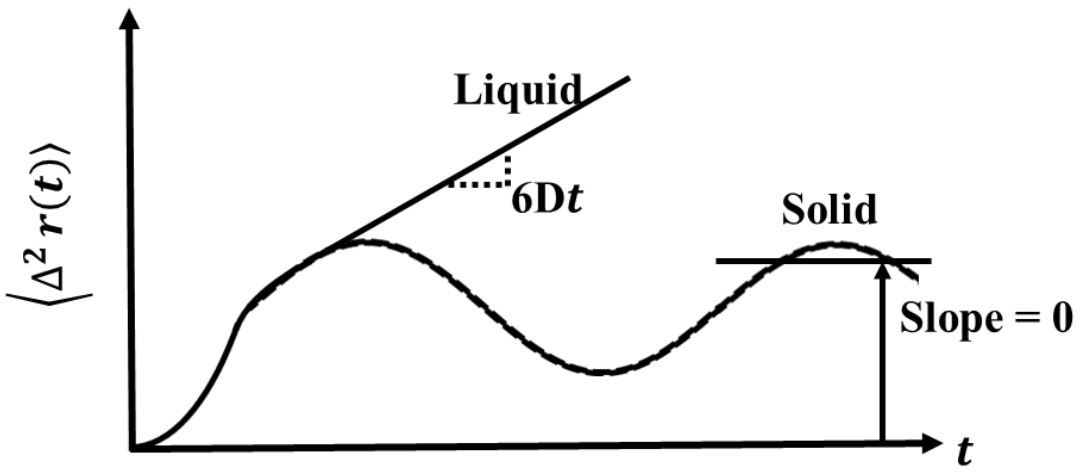

Figure 3.6 MSD vs. time of gas, liquid, and solid

For liquid systems, the denominator in Equation 4 is comprised of η, viscosity, as shown in Equation 11. By substituting Equation 11 into Equation 10, a predicted or simulated viscosity can be calculated for each system.[68]

$$\gamma = 6\pi\eta R \qquad \text{(Equation 11)}$$

As shown in Figure 3.7, the averaged MSD results were plotted versus time for the 4CyBOX, 4MBOX, and 4FBOX. The room temperature physical states of the 4CyBOX, 4MBOX, and 4FBOX were solid, liquid, and liquid, respectively. The trends provide just that, a trend. Due to the differences in time-scale probed in MD simulations, error between simulated and experimental results was expected in the dependent value obtained for η. For example, the experimental viscosity measured at 27 °C was 1.0 Pa*s and the simulated viscosity was 0.1 Pa*s.

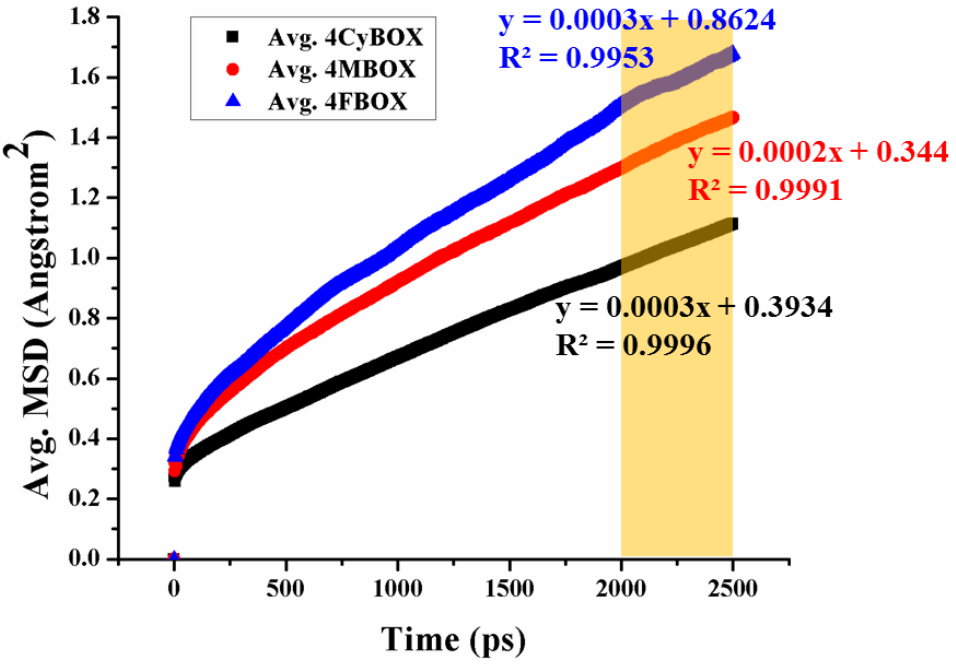

Figure 3.7 Averaged MSD versus time of para-substituted CyBOX, MBOX, and FBOX. Averaged data was collected for 3 replicates.

Although a direct quantitative prediction was not possible due to the large difference between the experimental and simulated viscosity, trends for qualitative predictions could be obtained. Such trends were well highlighted when comparing the FBOX constitutional isomers, as plotted in Figure 3.8. For example, the 3FBOX was almost solid-like and the 4FBOX was almost water-like. Comparatively, these trends are accurately depicted below where the 3FBOX has a slope close to zero, which indicates the lack of kinetic energy needed to demonstrate diffusive behavior like the trend for 4FBOX.

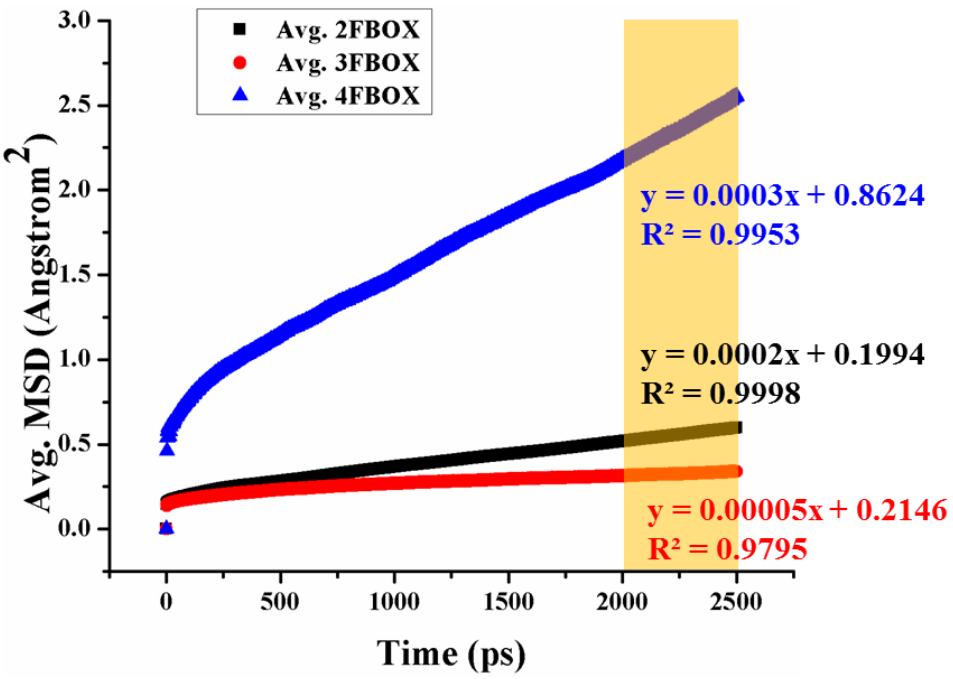

Figure 3.8 Averaged MSD versus time of 4FBOX constitutional isomers. Averaged data was collected for 3 replicates.

Overall, the use of MSD proved more accurate for qualitative predictions than the RDF and it is believed that running these simulations at times greater than 5,000 ps will yield more accurate viscosity predictions. However, there was no clear relationship between monomer structures and physical states or diffusivities of the monomer systems tested.

3.2.5 Electron Density Mapping & Analyses

Previously reported work has demonstrated that systems with high-order resulting from intermolecular attractions had a larger impact on the physical state as opposed to molecular orientation.[73, 74] In fact, the short-range intermolecular interactions, such as dipole-dipole attractions to afford ordered or dispersion forces to yield disordered systems, were found to control the physical state (i.e. solid, liquid, or gas) of a system.[75]

This finding was well exemplified in the partial charge maps for the 4CyBOX and 4MBOX systems displayed in Figure 3.9A and Figure 3.9B, respectively. In the map of 4CyBOX, Figure 3.9A, there are well isolated domains that are electron poor in the aromatic regions highlighted in red and orange, whereas the nitrile and heterocyclic atoms are electron rich and highlighted in yellow, green, and blue. The presence of well confined regions of opposite charge are postulated to induce strong dipole-dipole attractions yielding a high density ordered system, or solid physical state. An example of the hypothesized dipole-dipole attractions yielding order and packing (high density) is depicted in Figure 3.10A. Said postulation is supported by the experimentally observed solid physical state of 4CYBOX reported in Table 3.2.

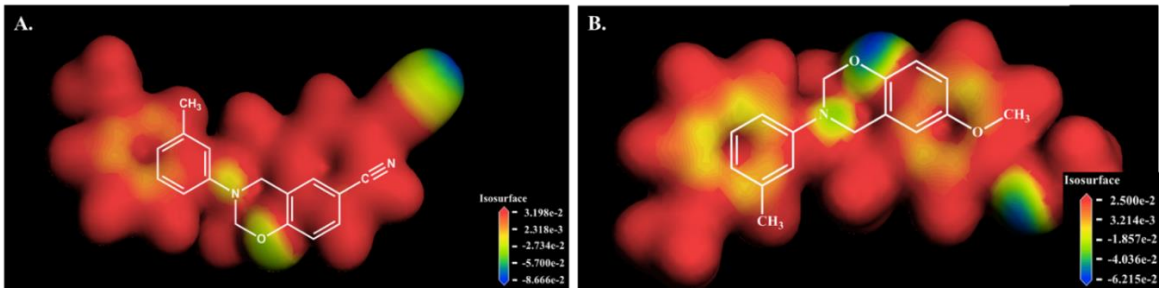

Figure 3.9 Partial charge maps of (A.) 4CyBOX and (B.) 4MBOX

Contrastingly, 4MBOX depicted in Figure 3.9B is comprised of well distributed regions that are electron rich and electron poor. Although intermolecular attractions and repulsions will be relatively equal, previous work by Arya in polyelectrolyte and colloidal particles found that mutually, or weakly, charged particle surfaces and polyelectrolyte chains experienced an overall net repulsion because the intermolecular attraction was not strong enough to overcome the entropic penalty resulting from a more

ordered system.[76] Similar to the findings of Arya, well distributed regions of electron densities in 4MBOX are postulated to promote stronger intermolecular repulsions affording a lower density disordered system, a liquid physical state, as simulated in Figure 3.10B.

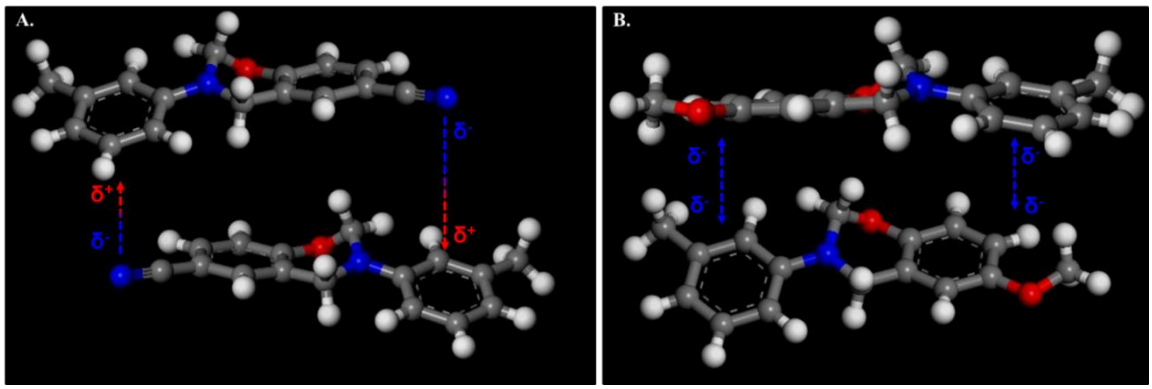

Figure 3.10 Theoretical representation of intermolecular attraction (A.) and repulsion (B.) in 4CyBOX and 4MBOX systems, respectively

This finding is complemented by the experimentally observed liquid physical state of 4MBOX reported in Table 3.2.

Qualitative observations of alignment between the electron rich and electron poor domains of the annealed 4CyBOX cell were made, Figure 3.11A; Figure 3.11a. Comparatively, no qualitative observations of alignment were made in the 4MBOX annealed cells, thus providing evidence that the simulated hypotheses in Figure 3.10 are true. To validate the hypotheses that intermolecular attractions in 4CyBOX and repulsions in 4MBOX are present, dynamic tests were conducted while monitoring the distance between the intermolecularly aligned regions of the 4CyBOX, Figure 3.11a. It should be noted that this test was not conducted for 4MBOX to eliminate experimental

bias as the coulombic charges were well distributed across the monomer; as opposed to, being isolated into electron rich and poor domains as in 4CyBOX.

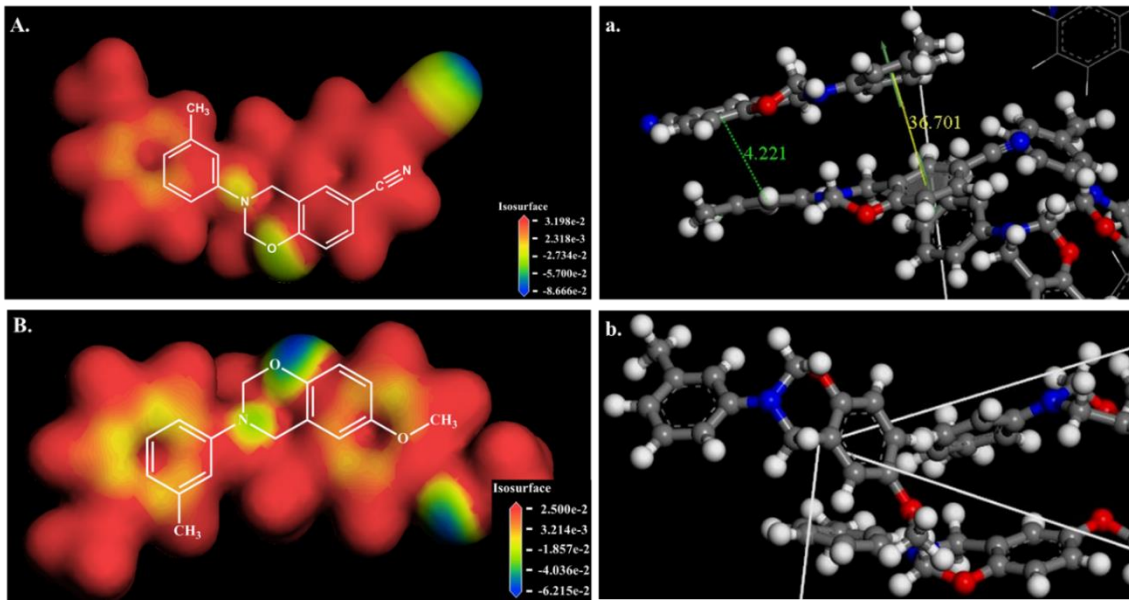

Figure 3.11 Electron density maps (A. 4CyBOX; B. 4MBOX) and dynamic test results (a. 4CyBOX; b. 4MBOX)

As a result of the dynamic test of 4CyBOX, Figure 3.11a, the intermolecularly aligned domains were maintained throughout the test. In the annealed cell of 4CyBOX, approximately 70% of the cell was aligned by intermolecular attractions, see Figure 3.12A and Figure 3.12B.

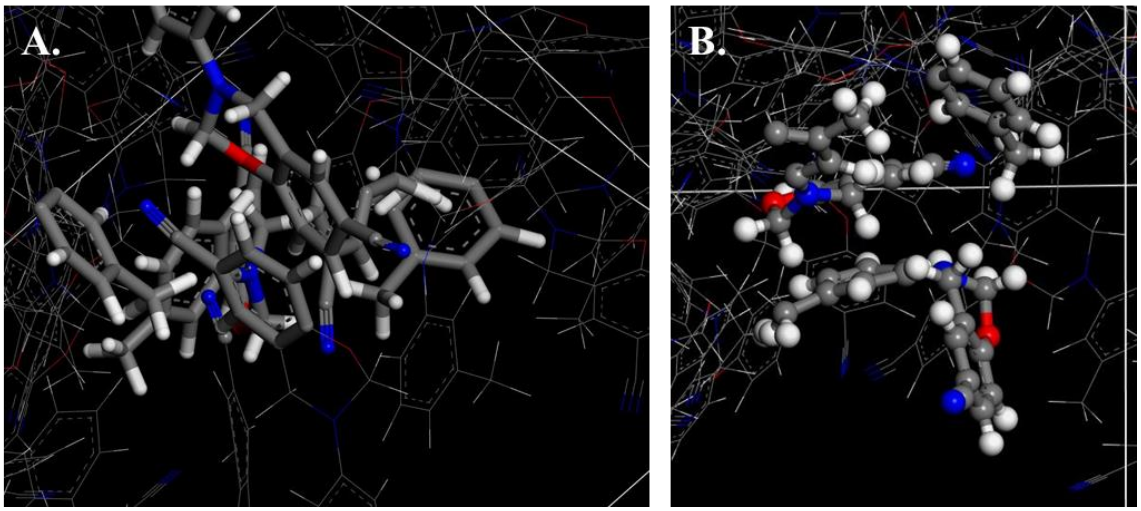

Figure 3.12 Additional examples (A & B) of localized order in the annealed 4CyBOX cell

Said aligned regions are observed throughout the cell, whereas no specific alignment can be identified in the annealed 4MBOX cell, Figure 3.11b. To further validate the differences in intermolecular attractions present in the 4CyBOX cell and repulsions in the 4MBOX cell, the percentages of molecules present within each cell were calculated after annealing. Since the cell dimensions were held constant and intermolecular attractions are believed to be higher for 4CyBOX than 4MBOX, then the percentage of molecules within the cell after annealing would be expected to be higher. In fact, the percentage of molecules within the 4CyBOX cell was higher, 93%, than 4MBOX, 75%.

3.3 Conclusions

In this work we provide new insight to the interrelationships between molecular architecture and physical state of monofunctional BOX monomers via molecular dynamics simulations. The simulated densities of geometrically optimized amorphous cells for each BOX monomer were within 2% error of the experimental densities; thus,

validating the confidence of the analyses and conclusions drawn from these cells. Annealing simulations conducted on each optimized BOX cell yielded a discontinuity that was identified from a bi-linear fit. It was found that the discontinuity provided a qualitative prediction of the physical state. For example, if the discontinuity is below room temperature (i.e. 300 K) then the monomer system should be a liquid; whereas, above room temperature the monomer system is predicted to be a solid.

Correlations between the predicted physical states and molecular architectures of the simulated BOX monomers were not quantitatively determined when analyzed by RDF and MSD. However, qualitative trends were obtained via MSD analyses where the slope provided insight to the diffusive behaviors of each system. This provided a comparative approach to predicting the ambient temperature flow behaviors of monomers based on previously analyzed systems. Comparing the results for the discontinuities obtained from anneal simulations and the diffusive comparisons to the molecular architectures in this work, no clear correlation was made. This provides evidence that substituent placement (ortho, meta, and para substitutions) and isomerism are not the dominate approaches for designing solid or liquid monofunctional BOX monomers. However, these evaluations did not consider the electronic characteristics of each monomer system.

Ab initio calculations demonstrated that the substituent identity and electron density distributions across BOX monomers have the most control over the BOX monomer physical state. Said calculations provided evidence that intermolecular attractions between isolated electron rich domains aligning with isolated electron poor domains provided localized order between BOX monomers systems, or a solid physical

state. Contrastingly, if the electron rich and poor domains were evenly distributed across the monomer then an overall net repulsion occurred because the intermolecular attraction was not strong enough to overcome the entropic penalty of creating order in a system. Said order and disorder can be qualitatively observed in the annealed simulations. Therefore, the anneal simulations and *ab initio* calculations presented in this work can guide the molecular-level design of monofunctional BOX monomers with predictable physical states.

Future work will include extending the findings from the electron density mapping and MSD results to design an approach to predict the viscosity of monofunctional benzoxazine monomers via MD simulations. Additionally, MD simulations will be used to correlate the effect of reactive diluent structure and loading on the bulk network properties of BPABOX.

CHAPTER IV – BATCH VERSUS ONE-STEP CONTINUOUS HIGH-SHEAR REACTOR FOR SYNTHESIZING BENZOXAZINE MONOMERS AND PREPOLYMERS

4.1 Abstract

This chapter of work develops a continuous high-shear reactor (CHSR) adept to synthesize benzoxazine monomers under solvent-free conditions. Validated by ^{1}H NMR, the continuous high-shear reactor demonstrates throughputs that are 6-40 times faster with increased efficiency in reaction kinetics, such as targeting specific monomeric conformations, as compared to current batch and continuous reactor technologies. Comparison of purified ^{1}H NMR spectra of monomers synthesized in a batch reactor to the unpurified ^{1}H NMR of monomers synthesized in the aforementioned reactor design, demonstrates that utilization of the continuous high-shear reactor for benzoxazine monomer synthesis yields a high purity product eliminating the need for post-processing purification. Synergistically, these attributes significantly increase throughput, synthetic control, and reduce the cost of melt synthesized benzoxazine monomers using the one-step continuous reactor presented in this work.

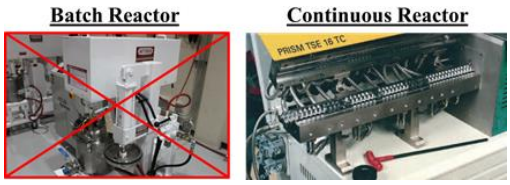

4.2 Results and Discussion

4.2.1 Monofunctional Benzoxazine (MoBOX) Monomer Syntheses

To date, a library of monofunctional benzoxazine monomers, MoBOX, have been synthesized under solvent-free conditions using the batch reactor, BR, and continuous high-shear reactor, CHSR, methods presented in this work, outlined in Appendix A. The substituent identity and location on the phenol and amine reagents did not limit the ability to synthesize MoBOX monomers using the CHSR method. This data is not provided as the novelty and most interesting results were demonstrated by monomers synthesized using meta-substituted phenols. For this reason, the following MoBOX sections will focus on the results and findings from syntheses using a meta-substituted phenol. Additionally, the effects of stoichiometry, processing temperature, and the reactor's screw design will be presented in the pilot-scale work in this chapter because the lab-scale reactor was limited in modularity at the time of this work. Herein, the meta-substituted MoBOX monomer synthesized by the batch reactor and continuous high-shear reactor methods will be referenced as MoBOX-BR and MoBOX-CHSR, respectively.

4.2.1.1 Monofunctional Benzoxazine Batch Reactor (BOX-BR) Synthesis

The reaction scheme of MoBOX heterogeneous syntheses, depicted in Scheme 4.1, is comprised of reacting any substituted phenol, primary amine, and paraformaldehyde in molar ratios of 1:1:4, respectively.

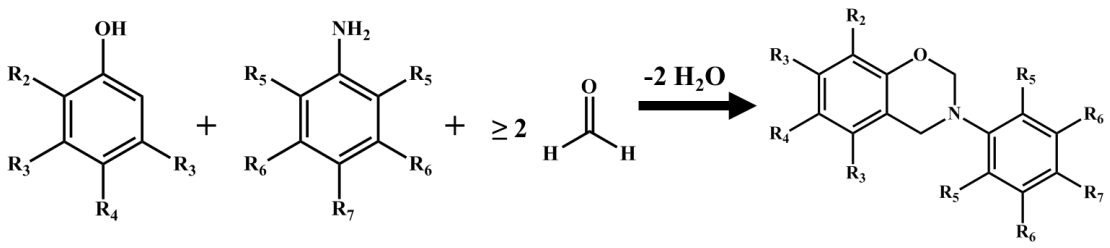

Scheme 4.1 Monofunctional benzoxazine reaction

For the syntheses in this chapter, the meta-substituted phenol yields an isomer blend; the major product is the kinetically favored monomer, along with the thermodynamically favored minor monomer product (Scheme 4.2). The major isomer is kinetically favored due to the reduced steric hindrance from the substituent of the phenol.

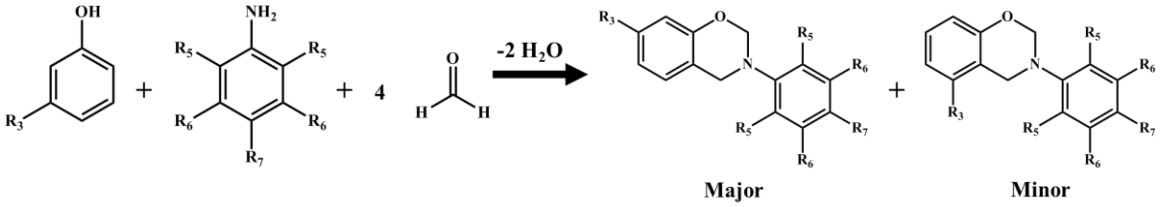

Scheme 4.2 Isomeric product formed in MoBOX heterogeneous syntheses

The absence of solvent in this melt synthesis affords the maximum kinetic efficiency, as the collision frequency is maximized. However, kinetic control is almost impossible, because the solventless protocol creates a heterogeneous system whereby gas-liquid, liquid solid, and gas-solid interactions occur during the reaction.[46] Furthermore, the poor heat transfer of the BR method accentuates the competition between benzoxazine ring formation and oligomerization. This yields a narrow temperature range for high-purity monomer synthesis.

Although the mechanism of benzoxazine formation is still debated, the scientific and patent literature report that the benzoxazine moiety is synthesized via a two stage reaction, characterized by the formation of two methylene linkages (i.e. –O-CH_2-N and –N-CH_2-Ar-). Each stage of the reaction occurs at two different temperature ranges that depend on the scale of the reaction.[19, 46] The reaction temperatures used for the MoBOX batch reactor trials in this chapter were chosen based on a patented solvent-free protocol where the reaction temperature for stage 1 was 115 °C and 120 °C for stage 2.[19] Although the reaction product's composition at each stage of the heterogeneous synthesis remains under dispute, the functionalities of the reactants in this work were comprised of two nucleophiles (i.e. phenol and amine) and one electrophile (i.e. aldehyde). This provided an opportunity to stage the reaction, or control the mechanism by which the benzoxazine ring formation can occur, by varying the reactant composition at each stage of the reaction (Table 4.1). For example, in trial 1 the reactants were charged to the batch reactor at the same time and then reacted at 115 °C for 40 min (Stage 1) and then at 120 °C for 20 min (Stage 2). In trial 2, the staged reaction was conducted by reacting phenol and paraformaldehyde at Stage 1 and then adding the amine was added to the mixture and reacted at Stage 2. Similarly, in trial 3 the staged reaction was performed by reacting amine and paraformaldehyde at Stage 1 followed by phenol addition to the mixture at Stage 2.

Table 4.1

Variations tested in reactant composition at each stage of the reaction. Phenol, amine, and paraformaldehyde are referenced in this table as P, A, and PF, respectively

Trial #	Stage 1 Reactant Composition	Stage 2 Reactant Composition
1	P+A+PF	
2	P+PF	A
3	A+PF	P

The effect of reaction mixture composition (i.e. staged versus unstaged) on the overall reaction time and purity of the MoBOX product was characterized by ^{1}H NMR analysis. Percent conversions were calculated by adding the integration values of the BOX methylene linkages and dividing by 4, which are the total number of protons possible for these linkages in a monofunctional BOX monomer. Said conversions are plotted as a function of total reaction time in Figure 4.1. In this plot, stage 1 of the reaction occurs from 0-40 min and stage 2 from 40-60 min.

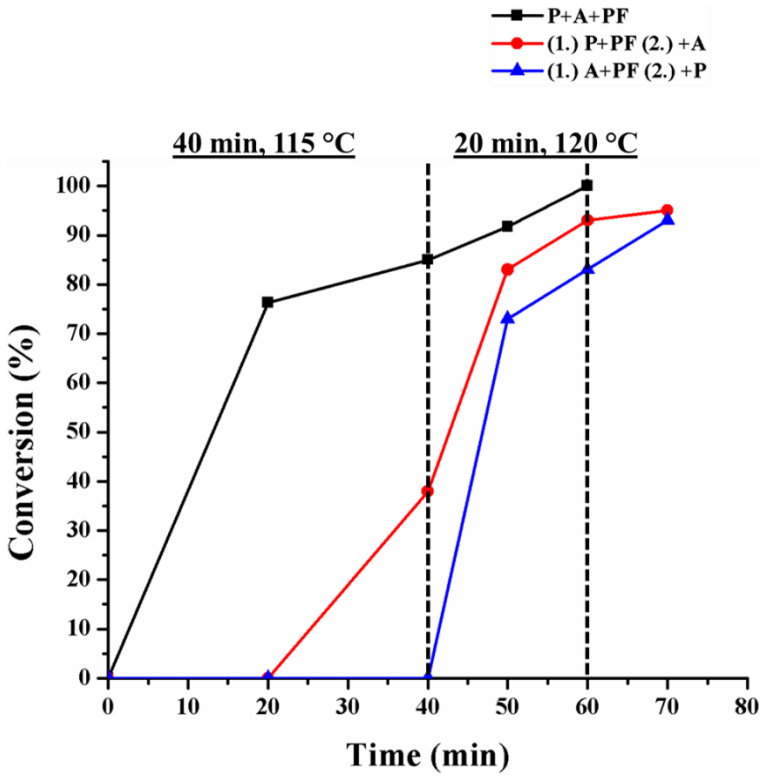

Figure 4.1 Conversion of reactants into monomer as a function of total reaction time for trials 1-3. Dotted lines indicate the reaction temperatures used during the reaction.

Although determining the reaction mechanism was outside the scope of this work, the data shown in Figure 4.1 provided evidence that the phenol was more reactive with paraformaldehyde than the amine. However, for both staged reactions 100% conversion was never achieved. When only the amine and paraformaldehyde were reacted in stage 1, as opposed to only phenol and paraformaldehyde, the final monomer conversions were 93% and 95%, respectively. Contrastingly, when all reactants were added at the same time (i.e. P+A+PF) in stage 1, the fastest reaction time was achieved and conversion was ~75 times higher at 20 min of reaction time, and 100% conversion was reached. For the MoBOX syntheses in this chapter, it is believed that the reaction times were faster when adding all of the reactants simultaneously because the amine and phenol are both liquids

at ambient temperatures and account for ~66 wt.% of the total reaction mixture. This provides a thermodynamically favorable environment for solubilizing the paraformaldehyde powder. Ishida *et al.* reported that the solvent-less synthesis method can be used for benzoxazines if either the reactants have similar and moderate melting temperatures or if at least one reactant is a liquid.[46] Furthermore, improved solubilization reduces the time needed to homogenize the reactants since solvent was not used for any syntheses in this work. The differences in homogenization rates between the reaction mixtures are depicted in images A and B in Figure 4.2. Image B in Figure 4.2 depicts the heterogeneity of the reaction mixture after 20 min at 115 °C when the reaction was staged with amine and paraformaldehyde present only. The heterogeneity was a result of large white agglomerations of paraformaldehyde. The lack of solubilization was similar when the reaction was stage with phenol and paraformaldehyde only. Conversely, when all reactants were added simultaneously the heterogeneity disappeared after 2 minutes reaction time, yielding a completely homogenized reaction mixture after 20 min at 115 °C (Figure 4.2 image B). Due to the improved solubility, the conversion was approximately 75 times greater than the staged reactions.

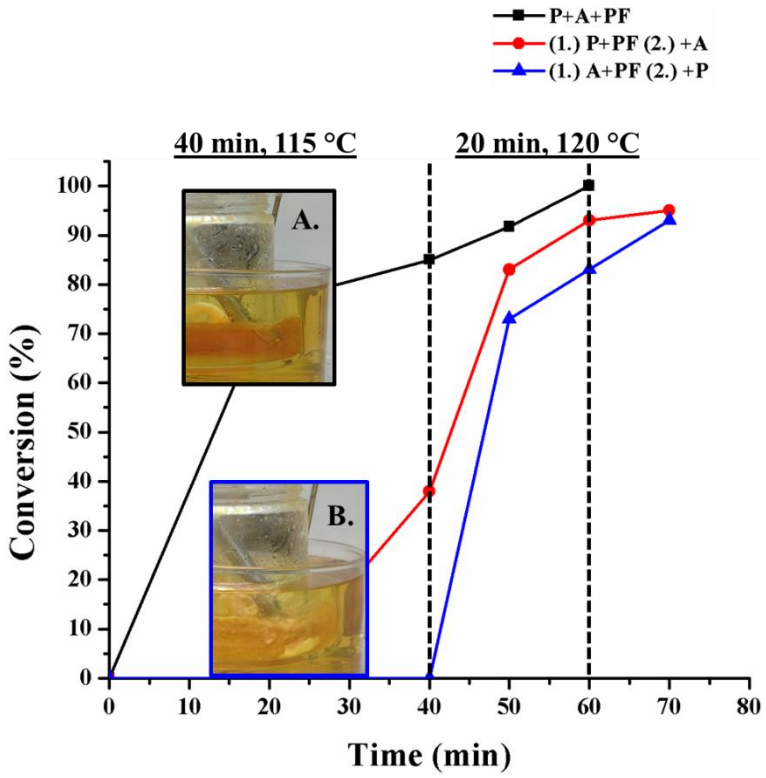

Figure 4.2 Conversion of reactants into monomer as a function of total reaction time for trials 1-3. Inset are images of (A.) Trial 1 and (B.) Trial 2 mixtures after reacting for 20 min at 115 °C

This finding is expected to be even more pronounced in the continuous high-shear reactor system because the total reaction volume will be reduced and much higher shear from the two screws will be applied to the reaction mixture. It is unknown why the staged reactions never reached 100% conversion; however the results demonstrated that all reactants can be charged to the reactor through the same inlet when scaling to the lab-scale and pilot-scale continuous high-shear reactors.

Prior to scaling the reaction to the lab-scale reactor, the reaction kinetics of adding the phenol, amine, and paraformaldehyde simultaneously to the batch reactor, was analyzed to further analyze the reaction kinetics and to obtain a purified sample of the product. ReactIR

kinetics data shown in Figure 4.3 validated that the reaction of phenol and paraformaldehyde occurs faster than the amine and paraformaldehyde. This was demonstrated by the increase in the amine's relative absorbance compared to the phenol and paraformaldehyde up to 60 min of reaction. ^{1}H NMR spectra validated that the methylene bridge between the oxygen and nitrogen of the oxazine ring formed first. Increasing the reaction temperature to 120 °C for approximately 20 min resulted in the formation of the methylene linkage between the nitrogen of the oxazine ring and the benzene ring of the phenol. Furthermore, the ReactIR kinetics study validated that the maximum conversion to monomer was achieved after approximately 25 min at 120 °C, as shown in the BOX-BR plateau in Figure 4.3.

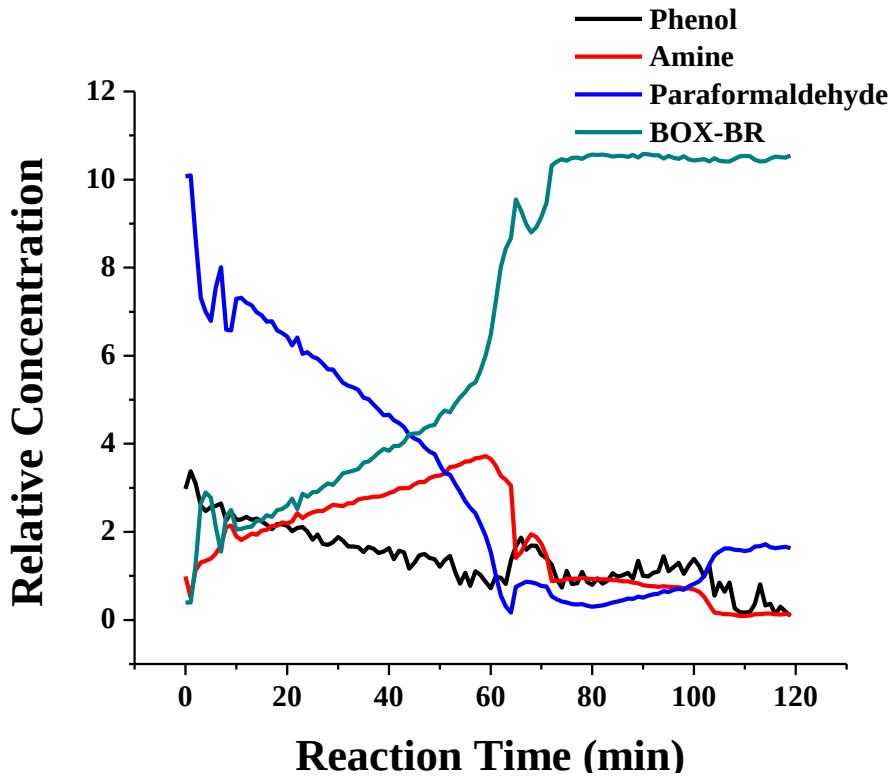

Figure 4.3 Reaction kinetics of MoBOX BR synthesis conducted at 115 °C for 40 min and 120 °C for 20 min.

The reaction product contained monomer and oligomer, as expected from the heterogeneous synthetic method; thus, purification was needed. The ^{1}H NMR spectrum of the purified product, displayed in Figure 4.4, validated that the BOX isomers were successfully synthesized at a yield of approximately 79%.

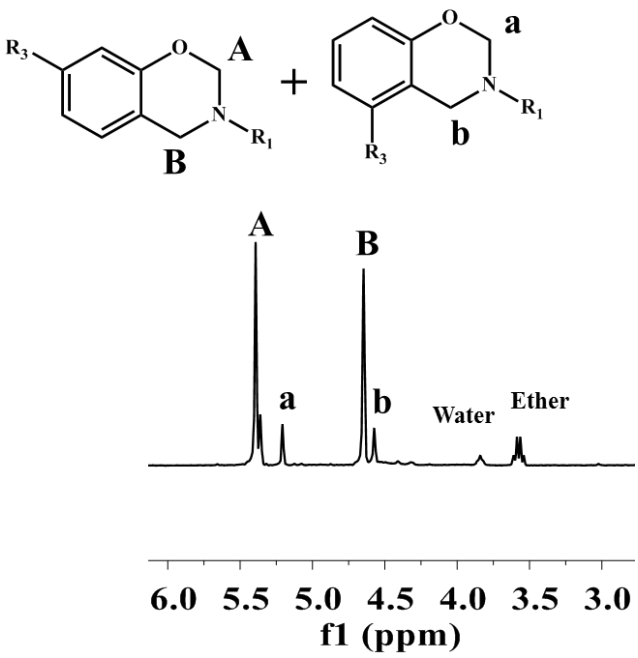

Figure 4.4 Proton NMR spectrum of purified MoBOX BR with a purity of 94% with post-processing purification

When comparing the integrated values of the characteristic benzoxazine peaks around 5.5 ppm (-O-CH_2-N-) and 4.5 ppm (-N-CH_2-Ar-) of the isomers, it was found that the purified isomer blend was comprised of approximately 80% major and 20% minor MoBOX isomers. Interestingly, after purification, as described in Chapter II, the purity of the product remained the same as before purification, or 94%. The post-purification impurities were water and diethylether that was used during purification. Additional heat could be applied to reduce the viscosity of the product and devolatilization could be continued, but increasing the heated residence time causes oligomerization (i.e. impurity) and therefore increases the overall energy consumption and cost of manufacturing. No change in the pre- and post-purification purity provided additional evidence of the difficulty in removing

solvent and the need to eliminate solvents from the synthetic protocols for these monomer systems.

4.2.1.2 Monofunctional Benzoxazine Lab-Scale Continuous High-Shear Reactor (MoBOX-CHSR) Synthesis

To provide a direct comparison between the batch reactor and the patented continuous high-shear reactor methods, the same reagents and molar ratios were used to make the feedstock that was pumped to the inlet of the reactor. The calculated error associated with both peristaltic pumps was less than 1% of the target feed rate, whereas the volumetric solids feeder error was ~ 6-8%. Higher feeding errors are generally expected for solid feedstocks as they are much less efficient to feed than liquids.[77] Despite the error determined during the calibration of the solids feeder, this error was higher during the trial. It was observed that steam was evolving from the inlet of the reactor during the trial and absorbed by the paraformaldehyde powder, which resulted in the formation of a partial plug in the feeder. As a result of the plug, the feed rate was not consistent and confidence in the molar ratios of the feed were difficult to quantitatively determine. Therefore, the manual feeding method was required because the lab-scale reactor did not have additional feeders (i.e. side-stuffer) to force feed the paraformaldehyde powder into the reactor.[78] Herein, all lab-scale reactor trials were conducted using the manual feeding method at a throughput of 1.5 lbs/hr, as reported in Chapter II, to reduce error in the reported stoichiometries for each reaction.

To determine the effect of the continuous reactor design on the reaction kinetics of the reaction and to identify an appropriate temperature to synthesize MoBOX, the processing temperature was varied from 120 – 220 °C in zones 3-5, or reaction zones, of

the reactor. Aliquots from each processing temperature were characterized via ^{1}H NMR spectroscopy. It should be noted that the processing temperature was 90 °C in zones 1-2, or mixing zones, below the reactants' boiling points while applying high-shear mixing to homogenize the reactants. The ^{1}H NMR spectra of aliquots processed at temperatures of 120 – 180 °C in the reaction zones, or Lots 1-4, demonstrated a decrease in intermediate peaks between 5.06 - 4.74 ppm with increasing processing temperature. However, the methylene bridges between the amine of the oxazine ring and benzene of the phenol (-N-CH_2-Ar-) were not fully formed, Figure 4.5.

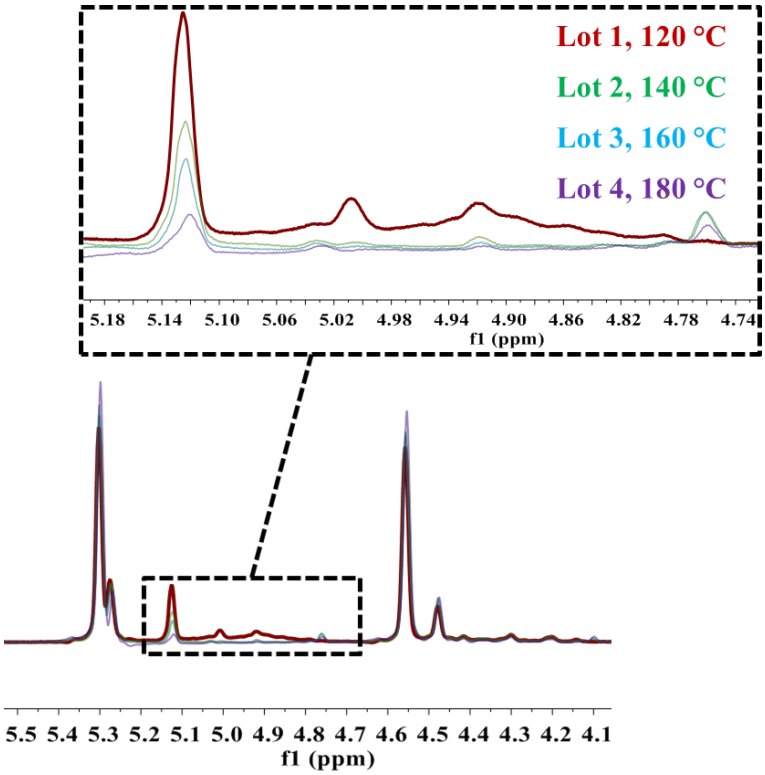

Figure 4.5 MoBOX-CHSR ^{1}H NMR spectra of Lots 1-4

However, the monomer ring opened at a processing temperature of 220 °C forming linear polymer. The MoBOX conversions as a function of processing temperature are listed in Table 4.2

MoBOX conversion per experimental processing temperature

MoBOX-CHSR	
Zones 3-5 Temperature (°C)	**Conversion (%)**
120	85.50
140	94.25
160	98.00
180	97.50
200	99.50
220	76.50

When the reaction zones were set to 180 °C and 200 °C, both ^{1}H peaks characteristic of BOX monomer integrated to approximately 2 protons, indicating a fully ring closed monomer, as depicted in the ^{1}H NMR spectrum in Figure 4.6 of the unpurified aliquot.

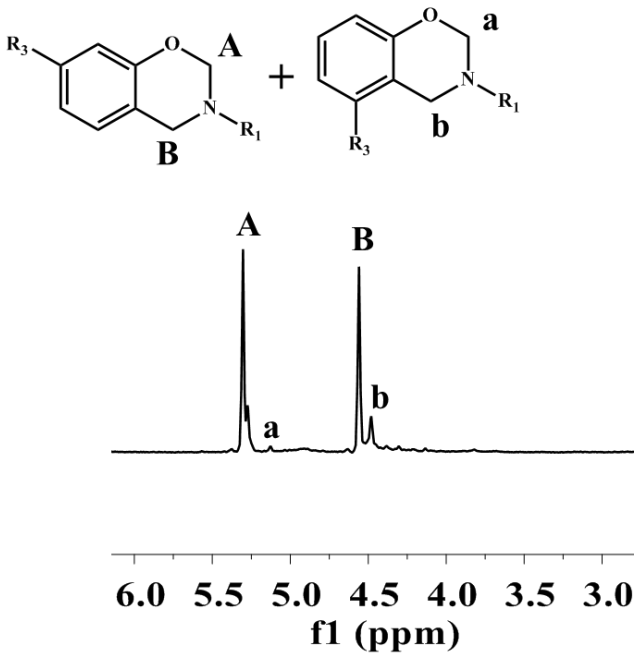

Figure 4.6 Proton NMR spectrum of unpurified MoBOX-CHSR processed at 200 °C with a purity of 99.3% without post-processing purification.

The trial was repeated at 200 °C; with all other processing parameters constant the yield was 76.8%. This value was within the reported range for benzoxazine syntheses, 70-90%.[38] It is believed that the yield was 76.8% because a 24% loss was expected due to the excess paraformaldehyde (x2 excess) with 2 mol of water lost as steam per mole of synthesized product. The CHSR method may also have a slightly lower yield than the batch reactor because low molecular weight intermediates are vaporized and exit through the outlet of the reactor. Said postulation was based on an aliquot of steam that was collected from the reactor's outlet in a plastic cup and the condensate was solubilized with acetone. The aliquot was analyzed via ^{1}H NMR and depicted in Figure 4.7. It was evident that intermediates were present by the oxazine peaks present around 5.5 and 4.5 ppm. The

presence of secondary amine and water were indicative of partially converted product, ultimately resulting in water condensation and development of a Schiff's base.[46]

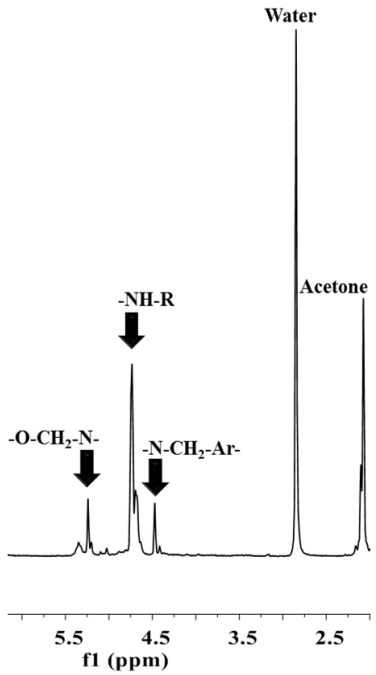

Figure 4.7 Proton NMR spectrum of steam condensate collected from outlet of CHSR method

Furthermore, a mass balance calculation, based on 500.70 g of feedstock, was conducted and it was found that up to 23.2% by mass of product was lost as by-product (Table 4.3). Investigations into devolatilization techniques were not possible using the lab-scale CHSR method and are addressed with the pilot-scale CHSR.

Table 4.3

Mass balance results from continuous high-shear reactor trial

Component	Mass (g)
Feed	500.70
Product	270.67
By-Product	124.86
Lost Product	116.16

Comparison of the ^{1}H NMR spectra of the purified MoBOX synthesized by the batch reactor with spectra of unpurified MoBOX synthesized by the CHSR method (Figure 4.8), shows that the CHSR is capable of synthesizing MoBOX without additional purification and with reduced minor isomer content (~12%) in 60 sec as opposed to 120 min required using the batch reactor.

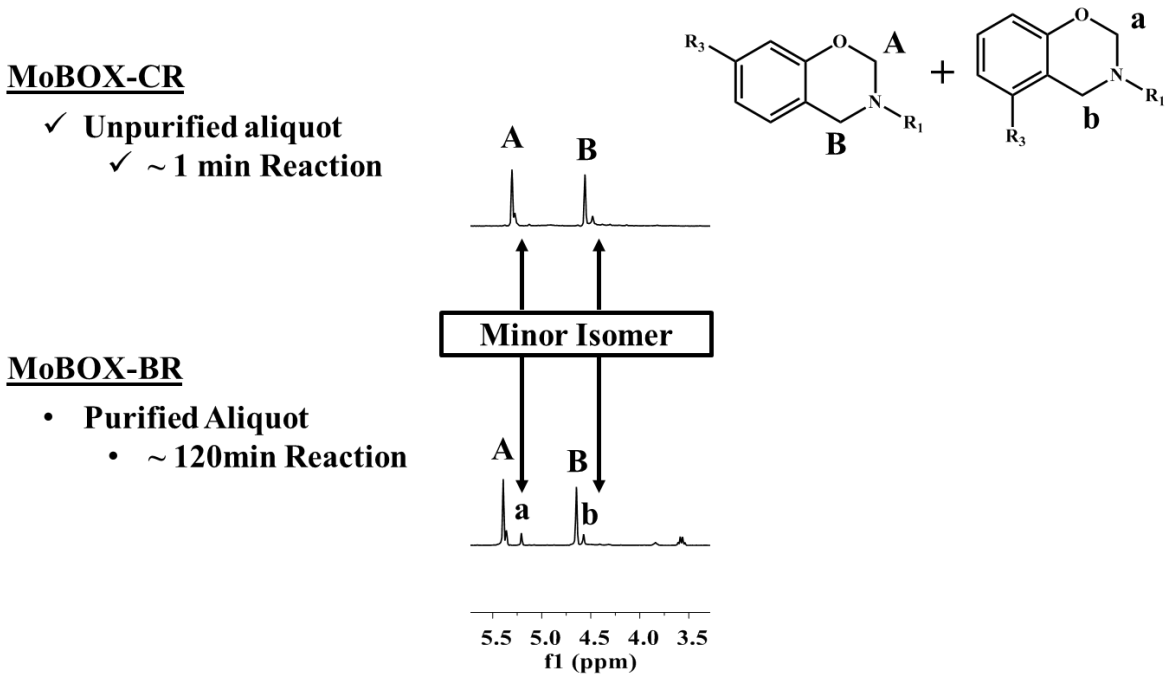

Figure 4.8 Proton NMR spectrum of unpurified MoBOX-CR versus purified MoBOX-BR

Although benzoxazine monomers have been previously melt synthesized in batch reactors[4] and single-screw extruders[44], there is no prior work or technology utilizing the truly "continuous" and single-step reactor design presented in this study. The 60 fold increase in reaction kinetics over that for batch reactors and increased reaction efficiency favoring formation of the major isomer are attributed to the reduced reaction volume, increased heat transfer, and high-shear environment in the continuous high-shear reactor. As reported by Gesser *et al.*, the reaction rates of heterogeneous syntheses are dependent on the physical state and diffusivity of the reactants.[79] With the reduced reaction volume and high-shear environment of the CHSR method in this work, the paraformaldehyde powder was solubilized much faster compared to the batch reactor, which afforded favorable thermodynamics by getting all the reactants in the same phase when the reaction

was occurring. Hence, the kinetic product, or major isomer, is favored in all CHSR trials. Furthermore, the increased solubilization rates of the reactants, reduced reaction volume, improved heat transfer, high-shear environment, and elevated temperatures explain the dramatic difference in conversion rates for the MoBOX CHSR aliquots after 60 seconds of reaction as compared to the batch reactor aliquots collected after 60 minutes of reaction, as summarized in Table 4.4.

Table 4.4

MoBOX-BR (40 min at 115 °C and 20 min at 120 °C) versus MoBOX-CHSR rate of conversion (60 sec of reaction at the tabulated temperature)

MoBOX-BR		**MoBOX-CHSR**	
Temperature (°C)	**Conversion Rate (%/min)**	**Temperature (°C)**	**Conversion Rate (%/min)**
115	0.61	120	85.50
120	2.18	140	94.25
		160	98.00
		180	97.50
		200	99.50
		220	76.50

Similar findings were reported by Yoon *et al.* where the reaction time of starch-*g*-polyacrylonitrile via continuous reactive processing was approximately 17x faster than the batch reactor synthesis despite the 25-50 wt.% solids content.[80] Additionally, the increased

solubilization rate of the heterogeneous reaction mixture in the high-temperature, high-shear, and solvent-free environment of the CHSR promotes high collision frequencies and intimate contact between the reactants in the CHSR. Considering that the continuous high-shear reactor was starve fed and Fick's first law of diffusion:

$$J = -D\frac{\partial \varphi}{\partial x} \qquad \text{(Equation 12)}$$

where J is the diffusion flux with respect to the amount of substance per unit time (mol/m^{2}s), φ is the amount of substance per unit volume (mol/m^3), and x is length (m), the diffusion coefficients were drastically increased since the volume of reagents was reduced and distributed along the barrel of the reactor increasing the reactive surface area. Liu reported that the heterogeneous synthesis of benzoxazines encompasses a series of side reactions involving gas-solid, liquid-solid, and gas-liquid reactions.[81] In this respect, reducing the reagent volume, increasing the physical contact, and having the ability to utilize a reaction temperature 80 °C above the batch reactor yielded a more homogeneous distribution of reacting phases. Although higher temperatures and shears can be tolerated via CHSR method since the residence time was 60x shorter than the BR, there is a maximum temperature above which the monomer will ring open and polymerize. When the processing temperature in zones 3-5 were set to 220 °C, the MoBOX began polymerizing, illustrated in Figure 4.9.

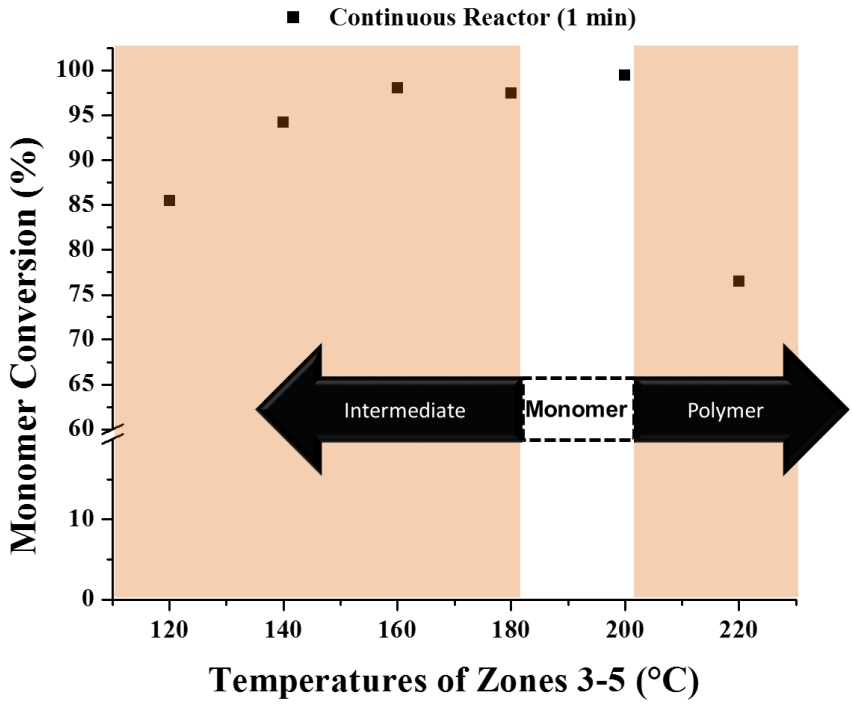

Figure 4.9 MoBOX CHSR conversions intermediates, monomer, and polymers calculated by ^{1}HNMR versus CHSR temperature

4.2.1.3 Monofunctional Benzoxazine Pilot-Scale Continuous High-Shear Reactor (MoBOX-CHSR) Synthesis

After proving that the lab-scale CHSR method is capable of synthesizing BOX monomers and prepolymers in a one-step continuous process, the focus was shifted toward determining the scalability of the CHSR design. Only the synthesis of MoBOX via the pilot-scale CHSR will be reported. Additional examples of BOX monomers successfully synthesized via the method presented are provided in Appendix A. Scaling to the pilot-scale CHSR was advantageous as it offers more modularity than the lab-scale reactor in screw design and reactant feeding methods. Furthermore, the pilot-scale reactor afforded an opportunity to evaluate the commercial viability of the reactor designs

in this work, as all trials were conducted at a throughput of 10 lbs/hr, or ~10x the throughput of the lab-scale CHSR trials.

For the first pilot-scale trial, the effect of screw design on the conversion of reactants to MoBOX monomer was evaluated. Rather than having 3 shear zones as used in the lab-scale reactor (Figure 2.3), only one shear zone was used in the first pilot-scale trial, see Figure 4.10. The shear zone, depicted in Figure 4.10, was comprised of one 45° kneading block (highlighted in blue) and two 90° kneading blocks (highlighted in grey). As indicated by their name, kneading blocks were added due to their high-shear and dispersive mixing capabilities.[82, 83] The 90 ° kneading blocks were also added because they do not promote forward conveying, hence their blocks are 90 ° off-set from each other. This increases the residence time and allows for high-shear mixing. The left handed, or reverse, conveying screw elements, highlighted in red, were added to create a melt seal so that sufficient vacuum could be applied to devolatilize the reactor.

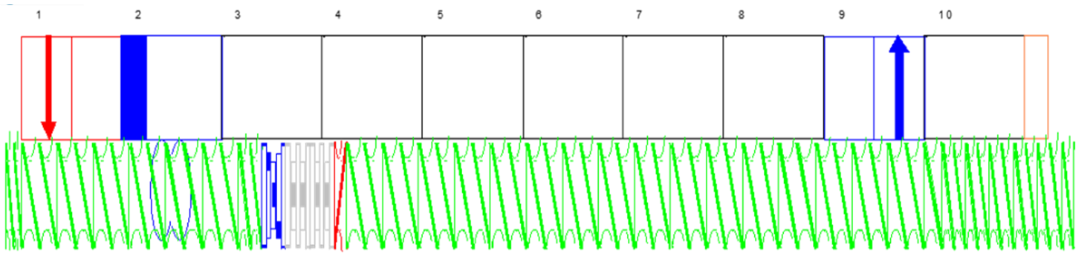

Figure 4.10 Screw design for Trial 1 with one shear zone as highlighted in blue and grey

Furthermore, the first shear zone of the screw was selected because it was specifically in the mixing zone of the barrel. The mixing zones, zones 1-5, is where the reactants enter the barrel, mixing, and solubilizing just before the temperature is increased to drive the

reaction to completion in zones 6-10, the reaction zones. Moreover, this temperature profile for the mixing and reacting zones was strategically selected so that all reactants are in the same or similar phase prior to reacting.

To determine the effect of the screw design outlined in Figure 4.10, the throughput, molar ratios of phenol:amine:paraformaldehyde, screw speed, and residence time were held constant at 10 lbs/hr, 1:1:4, 200 RPM, and 3 min, respectively. The temperatures in reaction zones 6-9 were increased, with aliquots collected for ^{1}H NMR analysis to determine the degree of conversion and purity. The temperature for zones 1-5 were held constant at 90 °C for all trials because this temperature was below the boiling points of the reactants. The first reaction zone temperature tested was 60 °C, to ensure materials were mixed and the flow rates were robust. Conversion values were not able to be calculated for aliquots collected for reaction zone temperatures of 60 °C and 160 °C due to solubility restrictions; the paraformaldehyde solids content was too high. Comparison of the color and solids content for the collected aliquots are depicted in Figure 4.11.

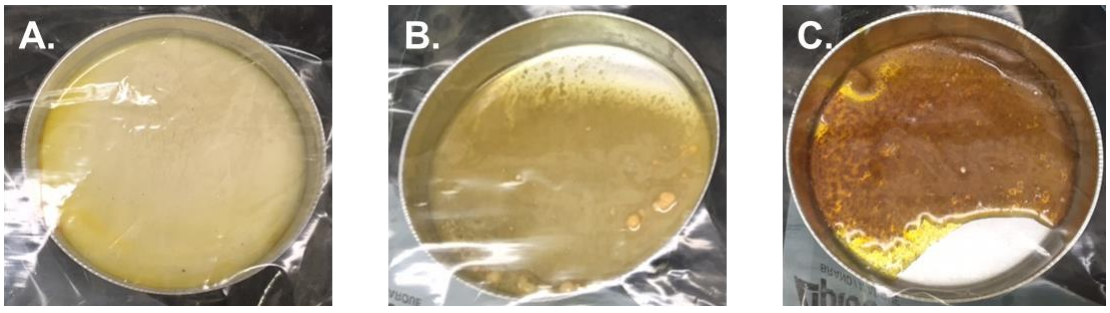

Figure 4.11 MoBOX pilot-scale aliquots collected in trial 1 with zones 6-9 set to (A.) 60 °C, (B.) 160 °C, (C.) 200 °C

The aliquot collected at a reaction zone temperature of 200 °C was much darker in color and had a reduced residual solid white powder content as shown in Figure 4.11, which was an indication that reaction occurred. The percent conversion was 88%; the results for all three temperatures are given in Table 4.5. Nevertheless, the presence of solid agglomerates in the aliquots, Figure 4.11 images A-C, suggest that more shear is needed in the screw design.

Table 4.5

Trial 1 processing parameters and conversions collected. Throughput, screw speed, and residence time were held constant at 10 lbs/hr, 200 RPM, and 3 min, respectively.

Zones 6-9 Temperature (°C)	**Linkage Integration -O-CH_2-N-**	**Linkage Integration -N-CH_2-Ar-**	**Conversion (%)**
60	-	-	0.0
160	-	-	0.0
200	1.82	1.7	88.0

Although there is not a direct method of scaling a reaction from the lab-scale CHSR to the pilot-CHSR, there was only an 11% reduction in conversion in pilot-scale reactor at 200 °C versus the lab-scale CHSR. The residence time in the pilot-scale CHSR was approximately 3x longer than the lab-scale reactor but at a 10x throughput throughput of reacting material. With that said, the 11% difference in conversion was attributed to

incomplete solubilization of the paraformaldehyde due to the weaker screw design, or less shear, and the need for increased reaction temperature or residence time.

To evaluate if a weaker screw design resulted in the 11% reduction in conversion, the closest mimic of the lab-scale screw design was built and added to the reactor (Figure 4.12). This screw design creates approximately 3 times the shear strength of the previous screw design (Figure 4.11).

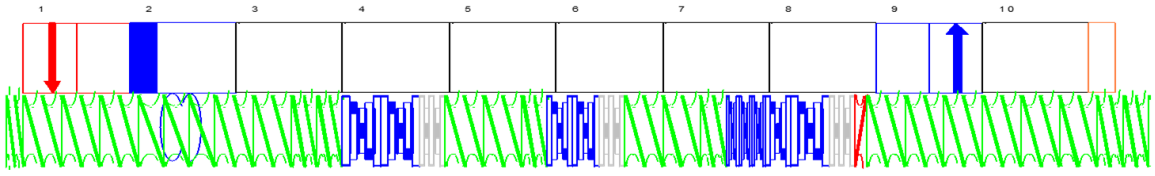

Figure 4.12 Screw design with shear increased with ~ 3x shear strength of Trial 1 screw design

To determine the effect of this screw design, the throughput, molar ratios of phenol:amine:paraformaldehyde, screw speed, and resident time was held constant at 10 lbs/hr, 1:1:4, 200 RPM, and 3 min, respectively. The residence time remained relatively unaffected by the screw design because the viscosity of the feed was too low at the reactor temperatures, 1.7-4.0 Pa.s, unless a dramatic change in kneading blocks and reverse conveying elements were added. Since the aliquots collected at reaction temperatures of 60 °C and 160 °C for the previous screw design could not be characterized due to solubility limitations, the processing temperatures were varied in the reaction zones at 200, 210, and 220 °C. The aliquot collected at 200 °C was a baseline reference to directly compare between the two screw designs to evaluate the effect of shear on MoBOX conversion. Aliquots collected at 210 °C and 220 °C were analyzed to

determine the effect of temperature on the MoBOX conversion using the stronger screw design.

As listed in Table 4.6, essentially the same conversion, approximately 88%, was achieved at 200 °C using the stronger screw design. This provided confidence that the screw design was not effecting the conversion because the mechanical energy provided by both designs was sufficient for the reaction to occur. Similar findings were reported by Moradiya in which 'sufficient' mechanical energy, defined by the number of shear-producing elements in the screw design, was considered a 'critical processing parameter' in achieving high-purity and 100% conversion.[84] The screw designs in this work were supplying similar mechanical energies; the processing temperature had a greater effect on obtaining nearly 100% conversion as shown in Table 4.6.

Table 4.6

Trial 2 processing parameters and conversions collected. Throughput, screw speed, and residence time were held constant at 10 lbs/hr, 200 RPM, and 3 min, respectively.

Zones 6-9 Temperature (°C)	**Linkage Integration -O-CH_2-N-**	**Linkage Integration -N-CH_2-Ar-**	**Conversion (%)**
200	1.75	1.73	87.5
210	1.90	2.00	97.5
220	1.99	1.98	99.3

As compared to the aliquot collected at 200 °C, when the temperature in zones 6-9 was increased to 210 °C a 10% increase in conversion was measured and a 12% increase at 220 °C. These results demonstrated that the conversion was more dependent on the reactor's temperature than the shear in the tested screw designs. Polycondensation reactions are well reported in the patent and scientific literature using twin-screw reactive extrusion synthetic methods.[85] The reduced reaction volume affording improved heat transfer at temperatures above the boiling point of water are believed to drive off water by-products, shift the equilibrium of the reaction in favor of the product, and accelerate the reaction rate.[86, 87] Similarly, the aliquot collected at 220 °C was darker in color and contained no solids content, as shown in Figure 4.13, which was attributed to the increased temperature and high-shear environment improved the evolution of gaseous-like water and excess formaldehyde from the product. Velez-Herrera *et al.* reported similar findings whereby excess formaldehyde and Schiff's base intermediates are removed either by rinsing the product with water or by increasing the reaction temperature to evaporate impurities.[88]

Figure 4.13 Aliquot collected during MoBOX pilot-scale trial with strongest screw design and zones 6-9 temperatures set at 220 °C

Similar to the lab-scale CHSR results, the composition of the aliquot collected when the reaction zones were set to 220 °C was comprised of reduced minor isomer content (i.e. 12%) compared to MoBOX-BR results (i.e. 20%), and the purity was approximately 98% without post-purification. These results are shown in Figure 4.14 in the ^{1}H NMR spectrum of this aliquot without post-processing purification.

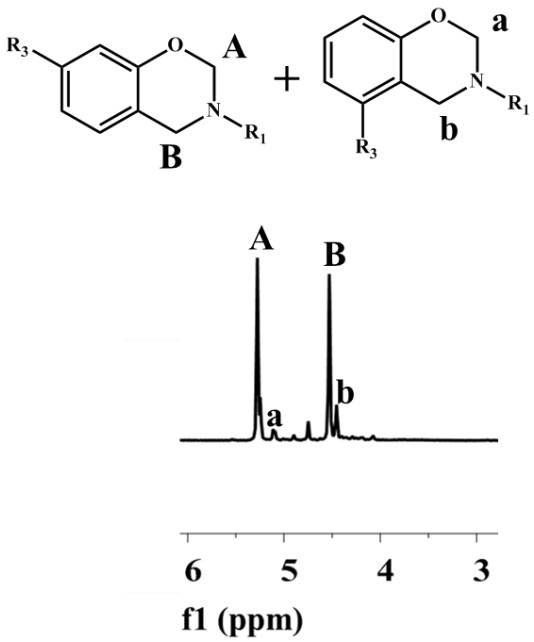

Figure 4.14 ^{1}H NMR spectrum of MoBOX aliquot collected from pilot-scale CHSR with strongest screw design and the temperature for zones 6-9 set to 220 °C

The remaining 2% impurities were believed to be a result of the difficulty experienced in trying to devolatilize the reactor. Since the by-product was in a gaseous phase and the product had a viscosity similar to water at the operating temperature, the vacuum system connected to zone 9 could not be used without removing 15 wt.% of the product from the reactor and reducing the yield. Said impurities were believed to be water, formaldehyde,

and trace amounts of intermediate or Schiff's base. To validate this, an aliquot was collected from the vacuum system and analyzed via ^{1}H NMR spectroscopy and the results are shown in Figure 4.15.

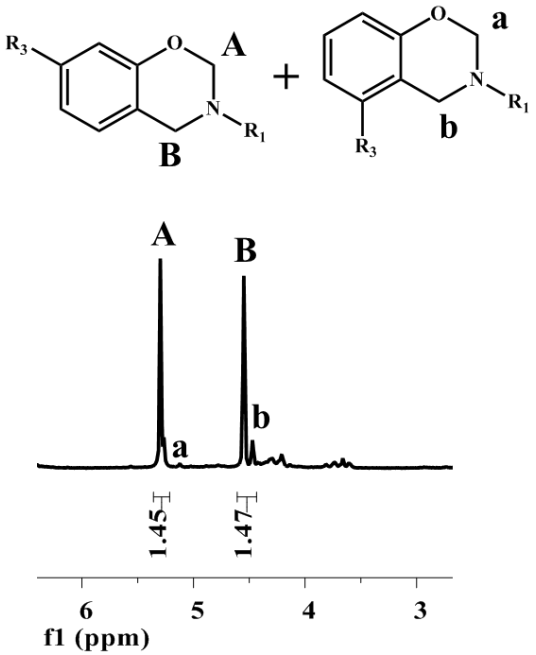

Figure 4.15 Aliquot collected from vacuum system during MoBOX pilot-scale trial

The results indicated that the aliquot collected from the vacuum system shows the presence of water (~1.52 ppm) and formaldehyde (~ 9.3 ppm), along with intermediates based on partially reacted oxazine peaks. Figure 4.15 and Table 4.7 summarizes the proton NMR results.

Table 4.7

Sample collected from vent of reactor. Sample also contained formaldehyde and water.

Sample	Linkage Integration -O-CH_2-N-	Linkage Integration -N-CH_2-Ar-	Conversion (%)
Vent	1.46	1.47	73.3

To overcome difficulties with devolatilization, the vacuum was vented into a snorkel fume hood to contain chemical vapors, and zone 10 temperature was increased to boil off any impurities prior to collecting aliquots at the outlet. The conversion results are given in Table 4.8. There was no effect on the conversion when the vacuum system was vented and when the zone 10 temperature was increased up to 216 °C. Consequently, there was also no effect (i.e. < 2%) on the level of impurities either.

Table 4.8

Trial 3 processing parameters and conversions collected. Throughput, screw speed, and residence time were held constant at 10 lbs/hr, 200 RPM, and 3 min, respectively.

Zones 6-9; 10 Temperature (°C)	**Linkage Integration -O-CH_2-N-**	**Linkage Integration -N-CH_2-Ar-**	**Conversion (%)**
220, 172	1.99	1.98	99.3
220, 207	1.88	2.00	97.0
220, 212	1.87	1.98	97.3
220, 216	1.91	2.00	97.8

As altering the screw designs and processing temperatures tested did not reduce the level of impurities, focus was shifted to the excess paraformaldehyde content. As reported by Velez-Herrera[88] and Wu[89], excess paraformaldehyde is commonly added in twice the excess amount to avoid the formation of an insoluble triazine network that can form between the amine and paraformaldehyde. Similarly, paraformaldehyde was fed in excess for all of the mentioned studies in this work, and therefore required removal from the product.

To elucidate the effect of paraformaldehyde content on the conversion and impurities of MoBOX synthesized via the CHSR method, a stoichiometric study was conducted. Simultaneously, the effect of screw speed, residence time, and the reaction temperatures in zone 6-10 were evaluated to determine the most effective processing

parameters to synthesize MoBOX and reduce the impurities. The processing parameters and subsequent conversion results are listed in Table 4.9. All results will be compared to Lot #1 as this exhibited the best results (i.e. highest MoBOX conversion and purity) obtained prior to the experiment. As shown in the results for Lot #8, when the residence time was double and temperature in zones 6-9 was increased to 225 °C the conversion was reduced by 6% when compared to Lot #1 which was a result of onset of oligomerization. This result highlighted the narrow margin of error balanced between residence time and reactor temperature that differentiates monomer synthesis from polymer synthesis. It is well reported that this narrow margin of error is considered a shortcoming of benzoxazines synthesized via the heterogeneous synthetic method in batch reactors.[46] Furthermore, the residence time was increased for Lot #8 as a result of decreased screw speed. By reducing the screw speed, the shear intensity was decreased, which reduces the mixing capability of the reactor. As a result, these findings highlight the magnitude that shear has on the success of heterogeneous BOX syntheses to homogenize the physical state of the reactants.

Table 4.9

Pilot-scale trial 4 MoBOX conversions calculated via ^{1}H NMR spectroscopy as a function of processing parameters.

Lot #	Zones 6-9, 10 Temperature (°C)	Molar Ratio of Phenol:Amine: PF	Screw Speed (RPM)	Residence Time (min)	-O-CH_2-N- Integration	-N-CH_2-Ar- Integration	Conversion (%)
1	220, 172	1:1:4	200	3	1.99	1.98	99.3
2	220, 172	1:1:2.5	100	5	1.74	1.84	89.5
3	220, 172	1:1:3.2	100	5	1.82	1.90	93.0
4	220, 172	1:1:3.7	100	5	1.88	1.94	95.5
5	220, 172	1:1:3.7	75	6	1.89	1.95	96.0
6	225, 172	1:1:2.5	75	6	1.90	2.00	97.5
7	225, 172	1:1:3.7	75	6	1.91	2.00	97.8
8	225, 172	1:1:4	75	6	1.86	1.90	94.0

When only the molar ratio of phenol:amine:paraformaldehyde was reduced from 1:1:4 in Lot #1 to 1:1:2.5 in Lot #2 as shown in Table 4.9, the MoBOX conversion was reduced from 99.3% to 89.5%. However, when the molar ratio of phenol:amine:paraformaldehyde was 1:1:2.5 and the residence time was double to 6 minutes for Lot #6, the conversion 97.5%. This proved that the MoBOX reaction was sensitive to the stoichiometry and excess paraformaldehyde enabled the fastest reaction rates to be obtained. At moderate levels of paraformaldehyde such as the molar ratios listed for Lot #3, 4, and 7 the conversions ranged from 93-97%, but the residence times

were almost double to achieve these conversions. Furthermore the conversions were not as high as Lot #1 and the impurities were relatively unchanged 1.7-2.0%.

Based on the pilot-scale results, it is still unknown if the level of impurities can be decreased without post-processing purification. The next steps for this work will focus on engineered solutions that entail advanced devolatilization equipment and vent placement.

4.2.2 Difunctional Benzoxazine (DiBOX) Monomer Syntheses

To date, a library of difunctional benzoxazine monomers, DiBOX, have been synthesized using the CHSR method presented in this work. Additional examples of monomers synthesized via CHSR method are listed with structural validations in Appendix A. Similarly to the MoBOX syntheses, the substitution and identity of the substituents on the phenol and amine reagents did not seem to limit the ability to synthesize DiBOX monomers in the CHSR. This data is not provided because the novelty of eliminating the need for post-processing purification and reduction of the minor isomer was also demonstrated in the DiBOX-CHSR syntheses using a meta-substituted phenol, *m*-cresol. For this reason, the following DiBOX sections will focus on the results and findings from syntheses using *m*-cresol, 4,4'-(*p*-phenylenedioxy)dianiline, and paraformaldehyde powder.

4.2.2.1 Difunctional Benzoxazine Batch Reactor (DiBOX-BR) Synthesis

The reaction scheme of difunctional benzoxazine (DiBOX) in this work, depicted in Scheme 4.3, was comprised of reacting *m*-cresol, 4,4'-(*p*-phenylenedioxy)dianiline, and paraformaldehyde in molar ratios of 2:1:8, respectively. To the best knowledge of the

author, only one other reference has been patented on the solvent-less batch reactor synthesis of DiBOX monomers.[44] No publications using a CHSR have been reported.

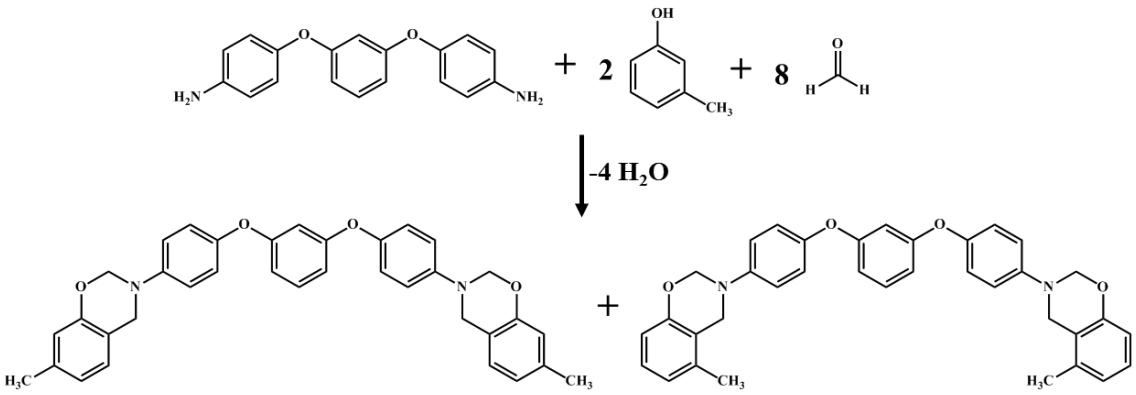

Scheme 4.3 Difunctional benzoxazine reaction

Similar to the MoBOX reaction, the mechanism of benzoxazine formation is still under debate and the scientific and patent literature report that the benzoxazine moiety is synthesized via a two stage reaction that is characterized by the formation of both methylene linkages (i.e. –O-CH_2-N and –N-CH_2-Ar-). Each stage of the reaction is commonly reported to occur at two different temperature ranges.[19, 46] The reaction temperatures used for the DiBOX batch reactor trials in this chapter were chosen based on a patented solvent-free protocol where the reaction parameters for stage 1 was 115 °C for 40 minutes and 150 °C for 4.25 hours.[44] Due to the high solids content (i.e. ~ 71 wt.%), the first stage temperature was selected based on a solubility study where aliquots from the reaction mixture were heated to 65, 95, 115 °C and their solids contents were compared after 20 min at their respective temperature. From this study it was found that after 10 min at 120 °C the reaction mixture was completely homogenized and optically transparent.

This homogenization at 120 °C was substantially faster than at 65 °C and 95 °C where solids white agglomerates were still visible after 20 min at their respective temperatures. This is an important finding for both the batch reactor and CHSR. For both reactors, the reaction rate is dependent on the homogeneity of the reactants.[46, 90] This factor is even more important for batch reactors where all of the reactants were added simultaneously and the solids content is 71 wt.% of the total reactants. The second stage temperature was selected because it was above the melting temperature of all the solid reactants but below the boiling point of *m*-cresol, 203 °C.

Aliquots were collected at each stage of the reaction and analyzed via ^{1}H NMR spectroscopy to determine the conversion of reactants to DiBOX. The results are listed in Table 4.10.

Table 4.10

Conversion results for each stage of reaction of DiBOX via the batch reactor method

Temperature (°C)	**Total Reaction Time (min)**	**Conversion (%)**
115	40	4.0
150	240	96.5
150	240.25	99.5

After 4.25 hours at 150 °C, the DiBOX monomer was successfully synthesized with a purity of 88%. Figure 4.16 shows the ^{1}H NMR spectrum prior to purification. After

purification, the purity was approximately 97% and the yield was 58.9%. This percent yield was below the reported range for benzoxazine batch reactor syntheses as a result of the substantial amount of intermediate and oligomer that was filtered away during purification. It is believed that the lack of reaction efficiency was a result of the 71 wt.% solids content, which contained a distribution of solubility rates because as the solids were solubilized the viscosity of the reaction mixture continued to increase creating additional diffusion limitations for the reactants.

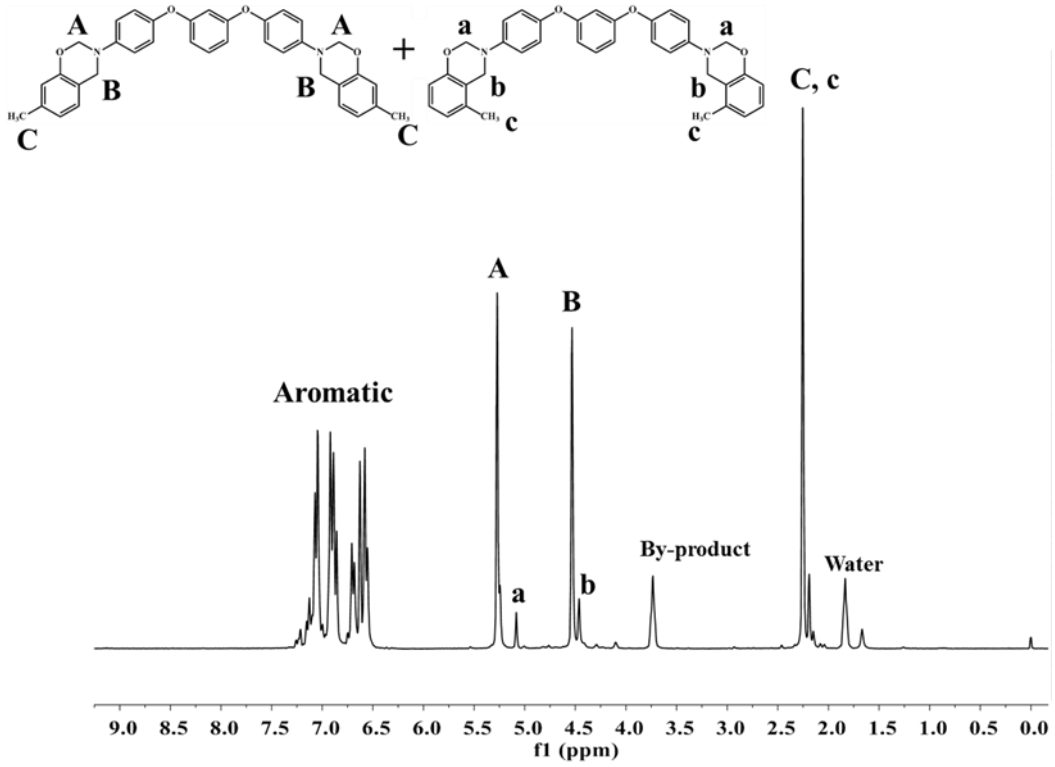

Figure 4.16 DiBOX-BR synthesized using 4,4'-(p-phenylenedioxy)dianiline, m-cresol, and paraformaldehyde in molar ratios of 1:2:8, respectively, without post-processing purification

As expected however, the purified product contained an isomer blend that was comprised of 86% major isomer and 14% minor isomer. Based on data obtained from the batch reactor, the reaction was scaled to the lab-scale CHSR using 150 °C as a starting temperature in the reaction zones, or zones 3-5, in order to compare the batch reactor and CHSR methods.

4.2.2.2 Difunctional Benzoxazine Lab-Scale Continuous High-Shear Reactor (DiBOX-CHSR) Synthesis

To provide a direct comparison between the batch reactor method and the patented continuous high-shear reactor methods, the same reagents and molar ratios were used to make the feedstock that was pumped into the inlet of the reactor, or zone 1, at a throughput of 1.5 lbs/hr using the manual feeding method. To determine the effect of the CHSR design on the kinetics of the reaction and to identify an appropriate temperature to synthesize DiBOX, the same high-shear lab-scale screw design from the MoBOX synthesis was used and the temperature of the reaction zones was varied from 150 – 205 °C. Aliquots from each processing temperature were characterized via ^{1}H NMR spectroscopy to determine the conversions at each temperature and to validate the structure of the final product. Said conversion values are listed in Table 4.11. Firstly, the aliquot collected after 1 min in the CHSR at 150 °C had a conversion 19x that of the aliquot analyzed from the batch reactor after reacting at 150 °C for 200 minutes.

Table 4.11

Lab-scale DiBOX-CHSR conversions per experimental reaction zone temperature

Temperature °C	**Conversion %**
150	77.4
170	80.8
190	91.0
205	99.9

The percent conversion continued to increase as expected with increasing reactor temperature until 99.9% conversion was achieved when the temperature of zones 3-5 was set to 205 °C. Figure 4.17 contains the ^{1}H NMR spectrum obtained from this sample without post-processing purification. Similar to the MoBOX CHSR results, the DiBOX aliquot characterized at 99.9% conversion had a purity of 95% without purification and yield of 71.8%. This yield is within the reported range for benzoxazine syntheses, which is 70-90%.[38] It is believed that the yield was 71.8% because the loss of excess paraformaldehyde and intermediate products evolving with the steam at the outlet of the reactor.

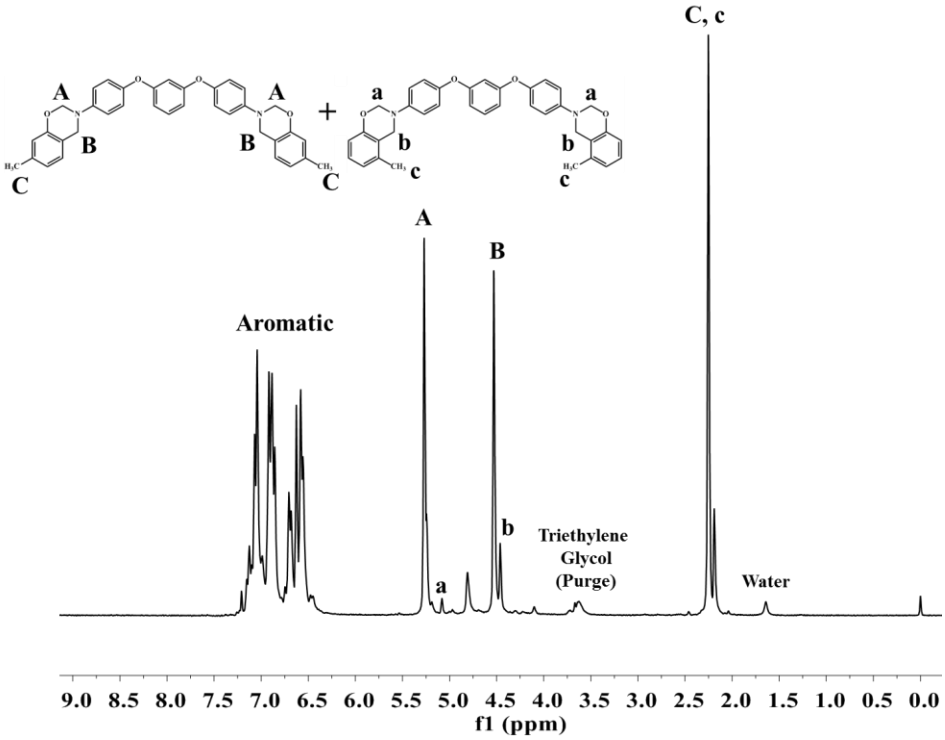

Figure 4.17 DiBOX-CHSR synthesized using 4,4'-(*p*-phenylenedioxy)dianiline, *m*-cresol, and paraformaldehyde in molar ratios of 1:2:8, respectively, without post-processing purification

Furthermore, the product contained an isomer blend of 90% major isomer and 10% minor isomer. This was overall a 4% reduction in the minor isomer content.

As previously mentioned, reaction rates of heterogeneous syntheses are dependent on the physical state and diffusivity of the reactants. Reduced volume of reagents and high-shear environment afforded by the CHSR increased the solubilization rates of the reactants. It is for these reasons that dramatic differences in conversion rates for the batch reactor aliquots versus the CHSR aliquots were achieved, as shown in Table 4.12.

Table 4.12

DiBOX-BR versus DiBOX-CHSR rate of conversion

DiBOX-BR		DiBOX-CHSR	
Temperature (°C)	**Conversion Rate (%/min)**	**Temperature (°C)**	**Conversion Rate (%/min)**
115	0.10	150	77.4
150	0.41	170	80.8
		190	91.0
		205	99.9

The reduced reagent volume, increased physical contact between reagents, and having the ability to utilize a reaction temperature 55 °C above the batch reactor yielded a more homogeneous distribution of reacting phases. Synergistically, these attributes are believed to also explain the drastic increase in reaction rate and increased reaction efficiency or reduced minor isomer content. Although the target of the previous work in this chapter was to synthesize BOX monomers only, the data in Figure 4.9 provided evidence that the reactor could also work for BOX polymerizations.

4.2.3 Alloy Formation & Prepolymer Synthesis via CHSR

After synthesizing MoBOX, an alloy comprised of 30 wt.% liquid MoBOX and 70 wt.% BPABOX were made in the CHSR under high-shear mixing to ensure that both monomers were well mixed. The liquid MoBOX was added as a reactive diluent and its loading was chosen because this is a common industrial benchmark when formulating

benzoxazines with the intent of improving their processability. Since kinetics data were obtained for MoBOX in the CHSR and BPABOX can crosslink if the kinetics were uncontrollable, isothermal rheokinetics data was obtained to characterize the BPABOX prepolymer conversion kinetics, Figure 4.18. This data was critical to determine the effect of time and temperature on the prepolymer conversion as these are controlled variables in the CHSR. Prepolymer conversion values were calculated by normalizing the storage moduli, G', by the maximum storage modulus, G_{max}', which is indicative of the most solid-like or cured nature of the experimental sample.[91]

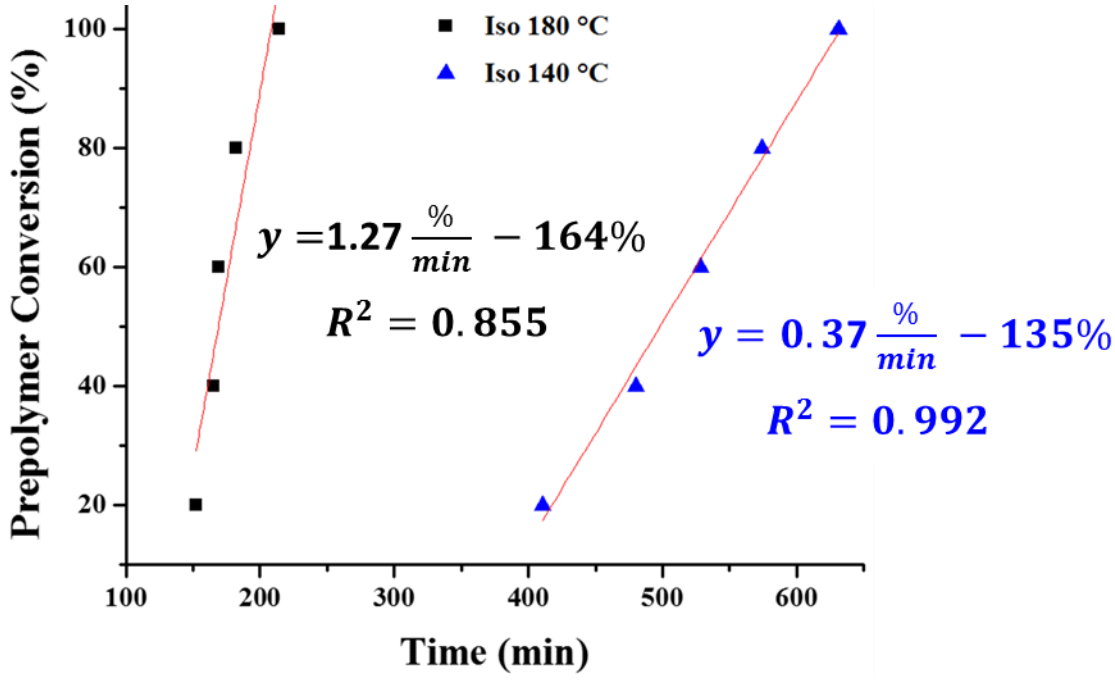

Figure 4.18 Rheokinetics of BPABOX prepolymer conversion versus time

The temperatures chosen for the isothermal study were based on staying below the onset of exotherm for BPABOX, ~ 169 °C, and the temperature from MoBOX CHSR trials that was below the polymerization conditions, 180 °C. The rheokinetics data will not directly

scale to the conversions obtainable in the reactor due to the substantially increased residence time of the material in the rheometer for testing and the lack of shear that is experienced in the reactor. However, the data provides evidence that the conversion could be controlled within the residence time in the CHSR, ~ 1 min, and the data provides points of reference for selecting processing conditions below gelation.

Measurable conversions were not obtainable for BPABOX until reacted in the CHSR at 150 °C in zones 3-5 and more pronounced at 170 °C as shown in Figure 4.19. Increasing conversion at 170 °C for BPABOX was expected as the onset on ring opening was measured at ~ 169 °C via DSC.

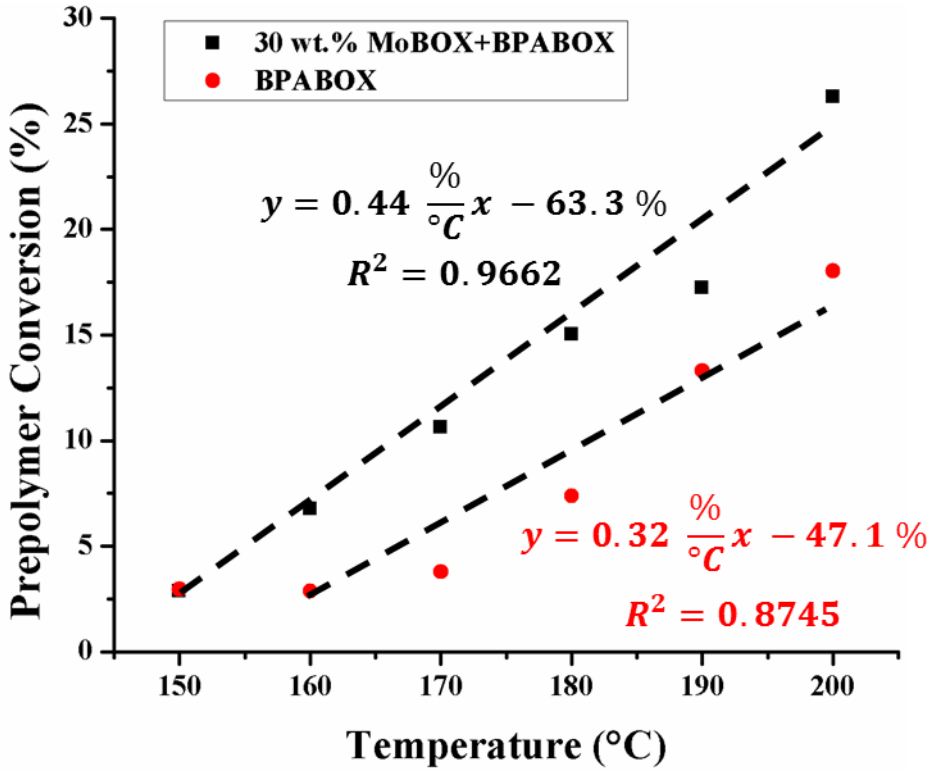

Figure 4.19 Prepolymer conversion after ~ 1 min of residence time versus CHSR temperature of BPABOX and 30 wt.% MoBOX+BPABOX Alloy obtained from DSC

The alloy demonstrated a more linear increase in prepolymer conversion over the temperature range 150 – 200 °C as shown in Figure 4.19. Moreover, the rate of conversion was higher than the neat system, BPABOX. Due to the MoBOX content and its lower thermal activation for polymerization, an increase in phenol content was expected at lower temperatures than neat BPABOX. Phenols are well reported to cause autocatalyzed curing for the polymerization reaction.[92] Synergistically, it is for these reasons that the increase in the rate of prepolymer conversion was observed in the alloy sample. Although control of the prepolymer conversion was achieved using the CHSR method, this approach was not scaled to the pilot-scale reactor. Future work will entail optimizing the thermal profile along the processing section of the reactor to determine the appropriate balance between shear and the time required to melt versus the needed time to react to a targeted prepolymer conversion.

4.3 Conclusions

Previously reported reactor technologies in the scientific and patent literature have been unable to synthesize BOX monomers in 1 min with a throughput of 1.5 lbs/hr at temperatures above approximately 100°C. Furthermore, the reports failed to discover the increased efficiency in reaction kinetics, or favoring the major isomer, by utilizing the continuous high-shear reactor methods presented in this work. Utilization of the continuous high-shear reactor for MoBOX and DiBOX monomer syntheses yielded a high-purity product and eliminated the need for post-processing purification. Reaction rates for the MoBOX and DiBOX CHSR syntheses were 60x and 200x, respectively, greater than their batch reactor syntheses. Due to the reduced reaction volume and high-shear environment of the CHSR in this work, the paraformaldehyde powder was solubilized much faster than

in the batch reactor. This afforded the best probability of having all the reactants in the same phase during the reaction. Consequently, the increased solubilization rates of the reactants, reduced reaction volume, high-shear, and higher temperatures afforded the dramatic difference in conversion rates for the batch reactor aliquots versus the CHSR aliquots. Furthermore, it is for this reason that it is believed the heterogeneous mixture of reactants were able to homogenize and react more efficiently in the CHSR, which resulted in a reduction of the minor isomer and an increase in the kinetically favored product for the MoBOX and DiBOX syntheses.

Although part of this chapter's target was to synthesize monomer only, the data from these experiments provided evidence that the reactor could also work for polymerizations. After synthesizing MoBOX, an alloy comprised of 30 wt.% MoBOX and BPABOX were made in the CHSR under high-shear mixing to ensure that both monomers were well mixed. Since kinetics data were obtained for MoBOX in the CHSR and BPABOX could crosslink if the kinetics were uncontrollable, isothermal rheokinetics data was obtained to characterize the BPABOX conversion kinetics. The isothermal rheokinetics demonstrated that neat BPABOX heated to 180 °C had a rate of prepolymer conversion approximately 3.4 times greater than at 140 °C. This data provided evidence that the conversion could be controlled within the residence time in the CHSR, ~ 1 min, and the data provided points of reference for selecting processing conditions in the lab-scale CHSR. Aliquots varied by processing temperature were measure via DSC, which determined that the rate of conversion was approximately 1.4x higher for the 30 wt. MoBOX+BPABOX alloy than the neat BPABOX. This was attributed to the increase in monofunctional benzoxazine moieties, which increased the autocatalytic content, or

phenol content, that was expected to increase with the ring opening polymerization. Collectively, it is for these reasons that the increase in the rate of prepolymer conversion was observed in the alloy sample.

Synergistically, the attributes demonstrated by the CHSR methods presented in this chapter significantly increase the throughput and reduce the cost of synthesized benzoxazine monomers and prepolymers. Although control of the prepolymer conversion was achieved using the CHSR method, this approach was not scaled to the pilot-scale CHSR. Future work on the BOX monomer syntheses should include optimizing the thermal profile along the processing section of the reactor to determine the appropriate balance between shear and the time required to melt versus the needed time to react to a targeted prepolymer conversion. Additionally, advanced downstream equipment for devolatilization should be investigated to improve the efficiency of removing by-product without removing product for BOX monomer syntheses.

CHAPTER V – EFFECTS OF REACTIVE DILUENT ISOMER STRUCTURE AND LOADING LEVEL ON THE PROPERTIES OF 6,6'-(PROPANE-2,2-DIYL)BIS(3-PHENYL-3,4-DIHYDRO-2H-BENZO[E][1,3]OXAZINE)

5.1 Abstract

Benzoxazines are an emerging class of thermoset chemistries that are under consideration as an attractive alternative to traditional phenolic and epoxy chemistries for high-performance and aerospace applications. Benzoxazine systems offer key advantages over epoxy based systems such as low chemical shrinkage values upon curing and low water absorption while maintaining the advantageous properties of epoxy amine systems such as heat resistance and flame retardance. Despite these advantages multifunctional benzoxazines suffer from processing limitations as they are commonly glassy solids at ambient temperatures. To address these limitations, benzoxazine alloys were prepared using bisphenol-a based difunctional benzoxazine, BPABOX, as the primary glassy solid multifunctional BOX monomer, and comparisons between the 3FBOX and 4FBOX reactive diluents from Chapter 3 were made. More specifically, this chapter demonstrates the effect of monomer structure (i.e. *para* versus *meta* isomers) and loading level of *para*- versus *meta*-substituted fluorophenol based monofunctional BOX, or FBOX, reactive diluent isomers blended with BPABOX on the alloy's processability (viscosity) and performance (structure versus property relationships). For naming purposes, the *para* and *meta* substitution is referencing the fluorine position on the phenol portion of the monomer. Herein, the para-substituted and meta-substituted FBOX diluents will be referenced as 4FBOX and 3FBOX, respectively.

5.2 Results & Discussion

5.2.1 Viscosities & Ring Opening Polymerization Activation Energies

All FBOX+BPABOX alloys were miscible affording homogeneous and transparent highly viscous liquid mixtures. For down-selecting alloys to be used on the knife-and-plate coater on the prepreg pilot line at the University of Southern Mississippi, a viscosity ranging between 5-8 Pa.s was targeted at 120 °C. The effect of FBOX isomer structure and loading on the 120 °C viscosity was measured using parallel plate rheology and the data are listed in Table 5.1.

Table 5.1

Complex viscosities of BPABOX and FBOX+BPABOX alloys at 120 °C

Alloy	**Viscosity at 120 °C (Pa.s)**
BPABOX	10.4
13 wt.% 4FBOX+BPABOX	5.3
30 wt.% 4FBOX+BPABOX	6.6
49 wt.% 4FBOX+BPABOX	3.0
13 wt.% 3FBOX+BPABOX	8.4
30 wt.% 3FBOX+BPABOX	6.9
49 wt.% 3FBOX+BPABOX	2.4

The 3FBOX alloys had a higher viscosity at 13 and 30 wt.% than the corresponding 4FBOX alloys; as shown in Figure 5.1, but all of the alloys were suitable for processing

based on to the targeted viscosity range. Overall, there were minimal differences in the alloy viscosities as a function of FBOX structure. The loading level of the liquid FBOX diluents had an indirect relationship with the alloy viscosity, with increasing diluent loadings in decreasing the 120 °C alloy viscosities (Table 5.1 and Figure 5.1).

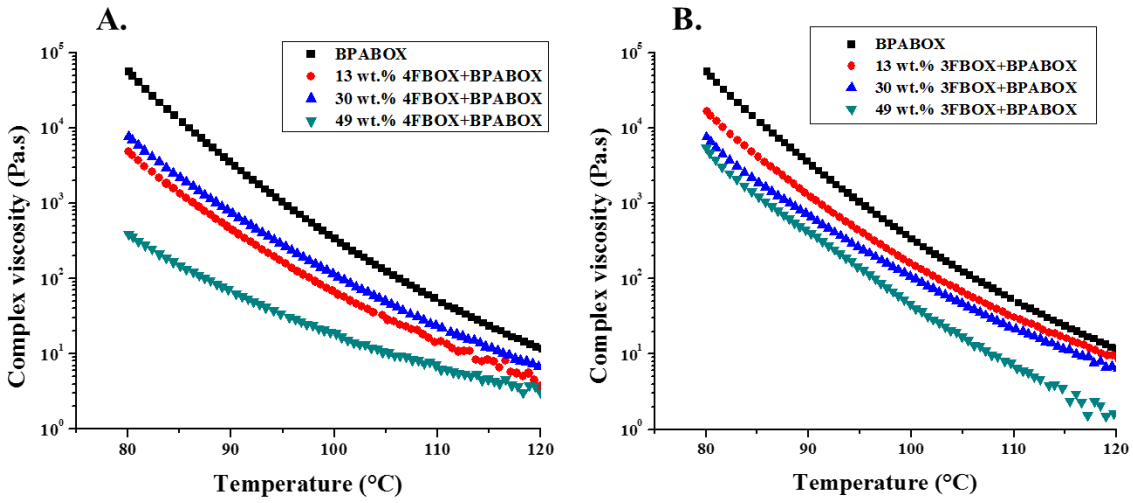

Figure 5.1 Complex viscosity versus temperature results of BPABOX and FBOX alloys

Although the alloys in Table 5.1 could be down-selected based on viscosity, or processability, the effects of isomer structure and diluent loading on the thermal stability and glassy network properties are also of importance.

Using the manufacturer's recommended cure prescription and comparing uncured specimens to their cured counterparts, the degree of cure was calculated to ensure matrix property comparisons were made on specimens having similar degrees of cure. As shown in Table 5.2, the degrees of cure were within approximately 17% between the cured alloys and neat BPABOX.

Table 5.2

DSC data for degree of cure calculations

Alloy	Uncured Exotherm (J/g)	Cured Exotherm (J/g)	Degree of Cure (%)
BPABOX	305.4	87.35	71
13 wt.% 4FBOX+BPABOX	275.9	119.5	57
30 wt.% 4FBOX+BPABOX	256.2	87.02	66
49 wt.% 4FBOX+BPABOX	255.7	99.69	61
13 wt.% 3FBOX+BPABOX	292.2	127.8	56
30 wt.% 3FBOX+BPABOX	249.3	114.5	54
49 wt.% 3FBOX+BPABOX	262.2	111.3	58

The variation in cure percentages are a result of heat transfer and diffusion limitations of the cure kinetics associated with thermoset chemistries. To validate the efficacy of the cure prescription, the T_g, determined from the maximum of the Tanδ peak, of the neat BPABOX sample was 180.83 °C and the Huntsman reported T_g for this cure prescription and analytical method is 180 °C.[93] These findings provided confidence in the sample preparation and cure prescription.

The scarcity of functional groups and diffusion limitations during cure were demonstrated by the results obtained from an isoconversional method developed by Friedman *et al.* and according to the experimental procedure described earlier.[94] Considering that a multitude of ring opening polymerization mechanisms occur during

cure, this model assumes that at every degree of cure, or percent conversion, an Arrhenius-type temperature dependence is present. This attribute is well reported for a variety of benzoxazine chemistries.[94, 95] As a result of this assumption and knowing the assumption is valid, any matrix chemistry regardless of mechanistic complexity can be described by this method. As shown in Figure 5.2 – Figure 5.8, the 1, 5, and 10 °C/min data had excellent fits according to the model where the correlation coefficients ranged from 0.998 to 0.999.

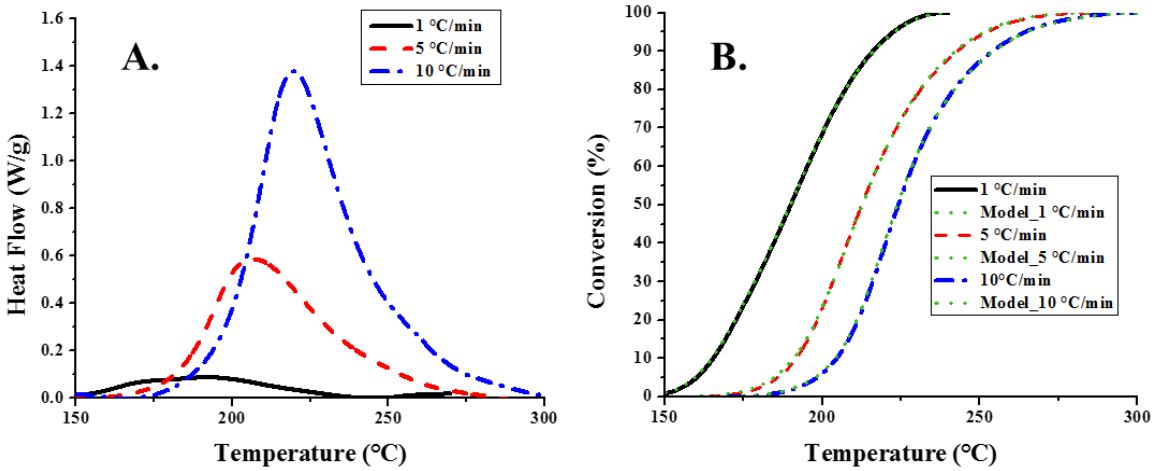

Figure 5.2 Heat flow vs. temperature (A.) and conversion vs. temperature (B.) per heating rate evaluated for BPABOX

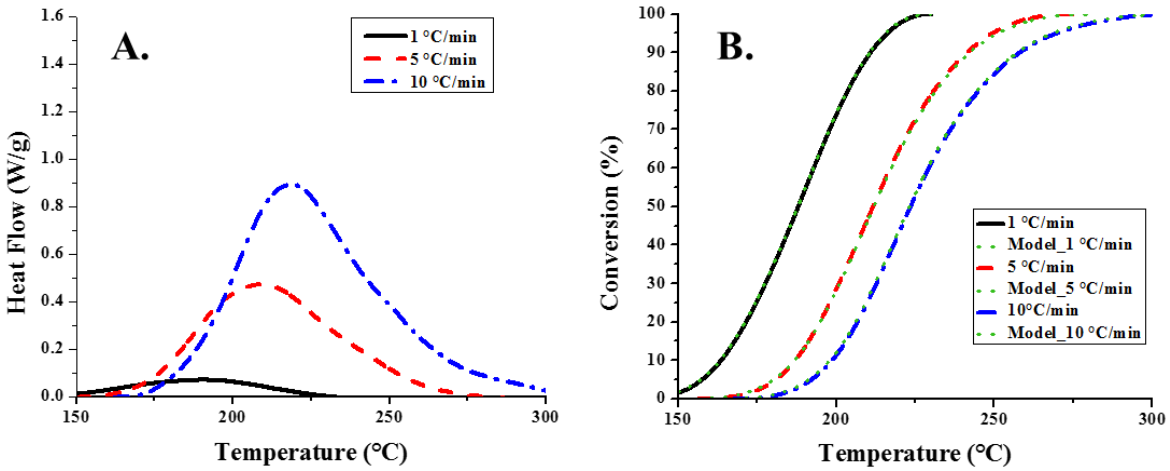

Figure 5.3 Heat flow vs. temperature (A.) and conversion vs. temperature (B.) per heating rate evaluated for 13 wt.% 4FBOX+BPABOX

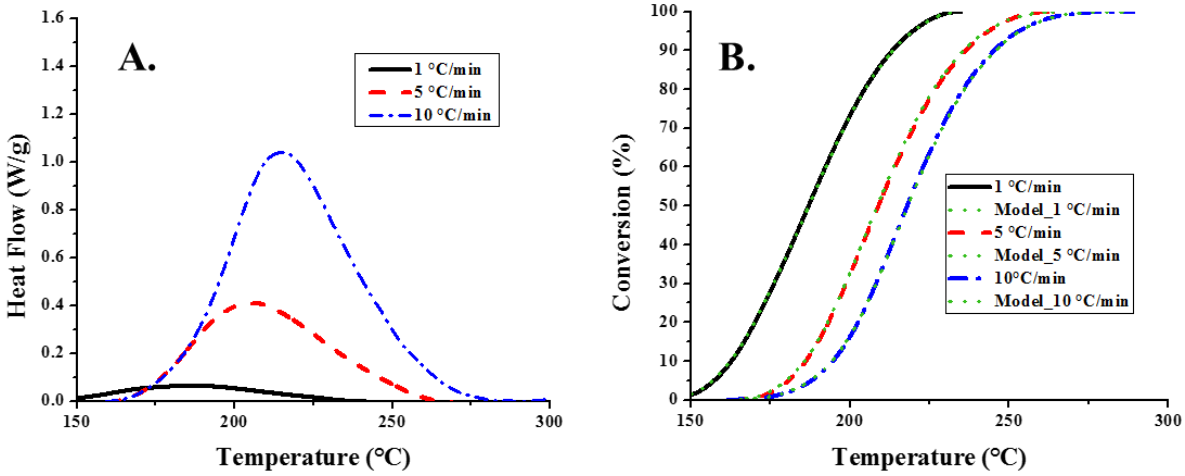

Figure 5.4 Heat flow vs. temperature (A.) and conversion vs. temperature (B.) per heating rate evaluated for 30 wt.% 4FBOX+BPABOX

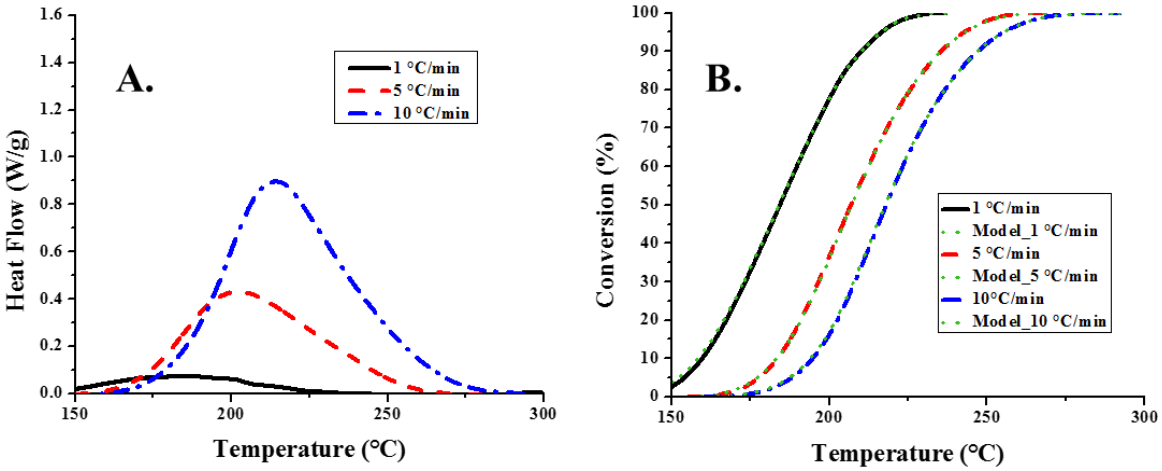

Figure 5.5 Heat flow vs. temperature (A.) and conversion vs. temperature (B.) per heating rate evaluated for 49 wt.% 4FBOX+BPABOX

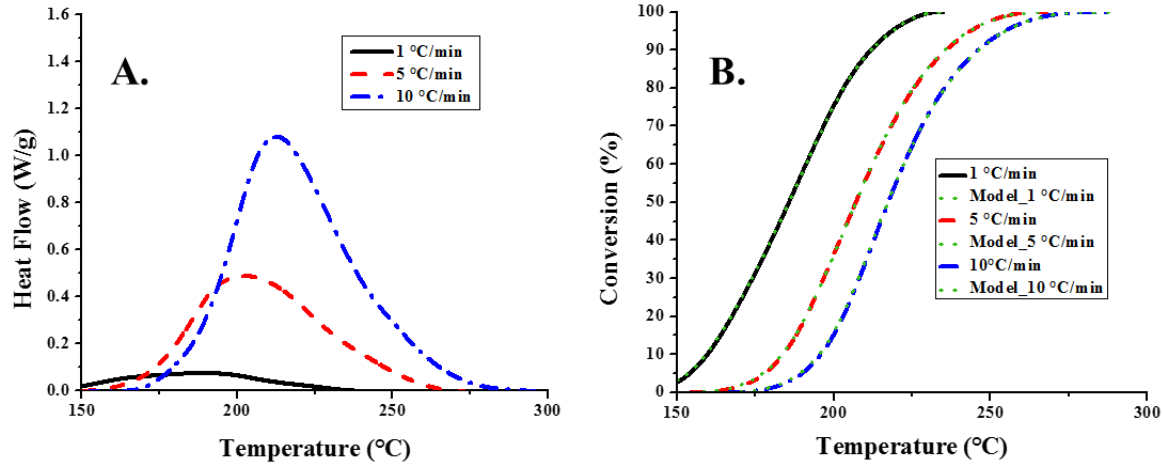

Figure 5.6 Heat flow vs. temperature (A.) and conversion vs. temperature (B.) per heating rate evaluated for 13 wt.% 3FBOX+BPABOX

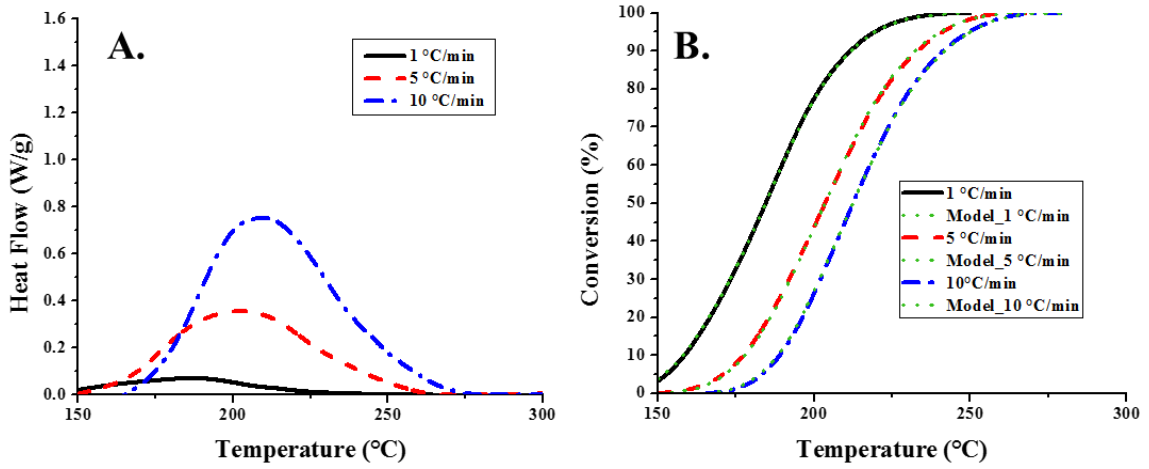

Figure 5.7 Heat flow vs. temperature (A.) and conversion vs. temperature (B.) per heating rate evaluated for 30 wt.% 3FBOX+BPABOX

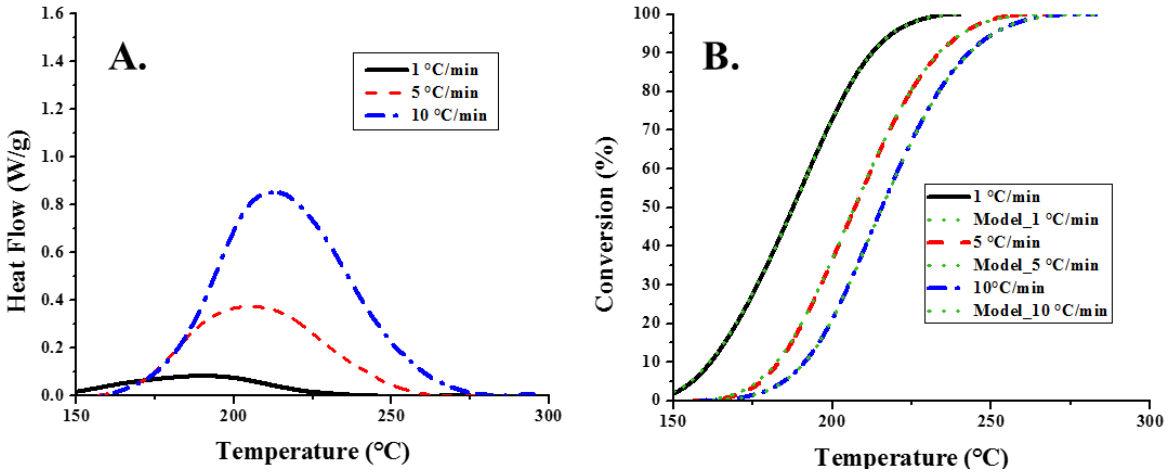

Figure 5.8 Heat flow vs. temperature (A.) and conversion vs. temperature (B.) per heating rate evaluated for 49 wt.% 3FBOX+BPABOX

From these results the activation energies for every alloy and the neat BPABOX were modelled between 10 to 90% conversion as shown in Figure 5.9 and Figure 5.10.

As expected for thermoset chemistries, the theoretical activation energies for the 4FBOX+BPABOX alloys, Figure 5.9, and 3FBOX+BPABOX alloys, Figure 5.10, increased with increasing conversion. Due to the shortage of functional groups with

increasing network conversion coupled with the diffusion limitations due to gelation, the activation energies increased up to approximately 60%.

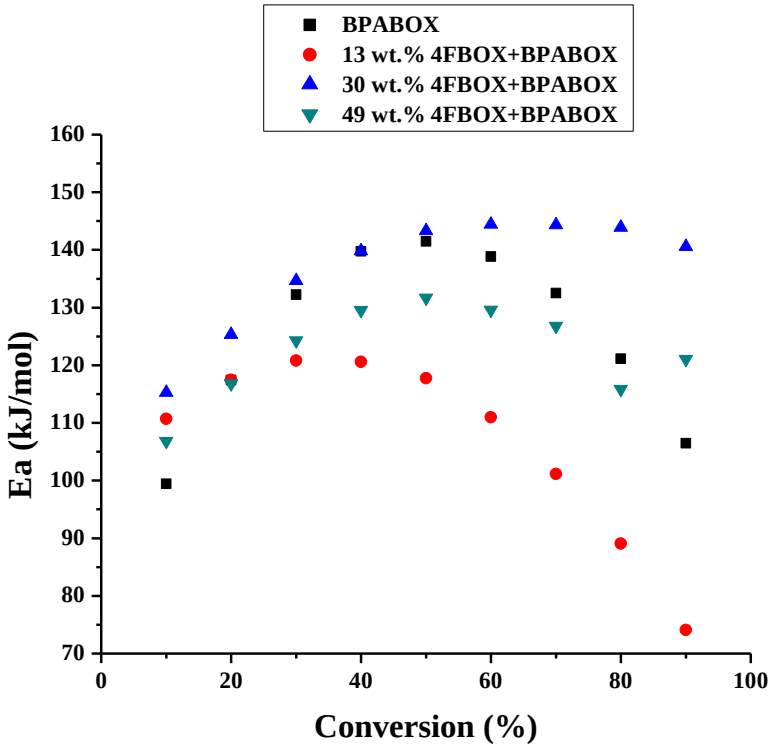

Figure 5.9 Activation energy vs. conversion for BPABOX and 4FBOX+BPABOX alloys

Interestingly, the increase in activation energies for both alloy systems only occurred until approximately 60% conversion according to the model. After 60% conversion the activation energies decreased unexpectedly for a thermoset chemistry, which demonstrated an autocatalytic behavior.

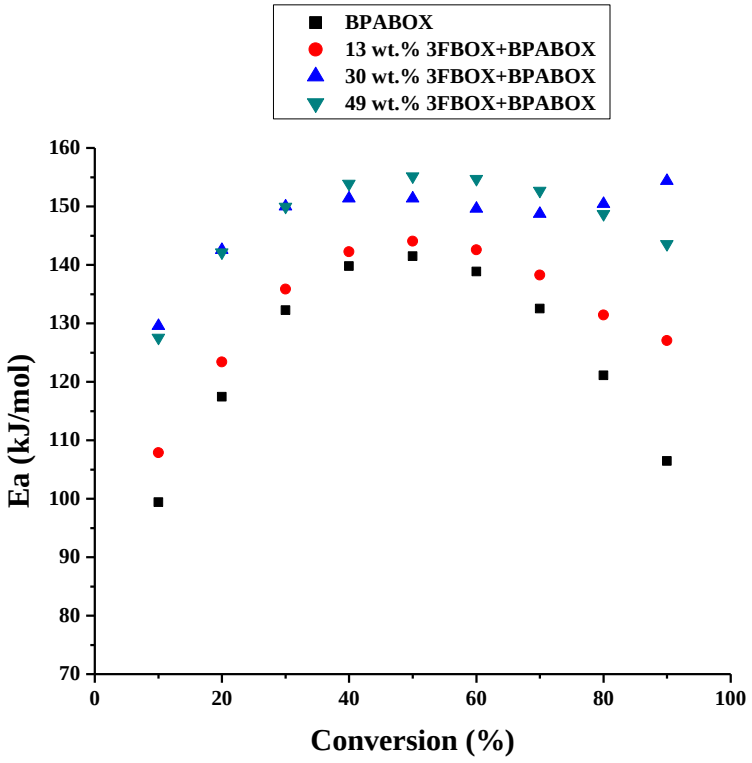

Figure 5.10 Activation energy vs. conversion for BPABOX and 3FBOX+BPABOX alloys

Due to the increase in monofunctional benzoxazine moieties, or reduction in available functional groups in the formulation, an increase in phenol content was expected and phenols are well reported to autocatalyze curing, or the polymerization reaction.[92, 96] The accepted ring opening mechanism is propagated from the reactive site, or the oxazine ring, which is comprised of oxygen and nitrogen in a bent semichair configuration where relief of the ring strain is a driving force for the ring opening polymerization.[95] As the polymerization reaction propagates, hydroxyls are formed as part of the phenolic portion of the BOX monomers. Said hydroxyls initiate via protonation of an oxygen atom in a neighboring BOX moiety, which reacts to form a zwitterionic iminium intermediate that reacts through electrophilic substitution with a neighboring molecule.[97, 98]

Synergistically, it is for these reasons that the increase in the rate of conversion was observed in the alloy samples. Contrastingly, the activation energies of the 3 FBOX+BPABOX alloys early in the reaction are higher than the neat resin, but the 4FBOX+BPABOX alloys were mainly lower. This indicates that 4FBOX provides more of a positive effect on the curing kinetics than 3FBOX by affording a slightly greater shift in temperature for the onset of cure. Furthermore, this was experimentally evidenced by an 8% reduction in the onset of cure temperature, defined by the onset of the exotherm, of the 49 wt.% FBOX alloys compared to BPABOX, Figure 5.11.

Additional insight to the mechanistic behavior of these alloys was provided by the unimodal DSC thermograms overlaid in Figure 5.11. Despite the alloys binary composition (i.e. BPABOX and FBOX reactive diluent) before cure, the presence of one exotherm is indicative that the reaction between BPABOX and the FBOX reactive diluents were occurring simultaneously.

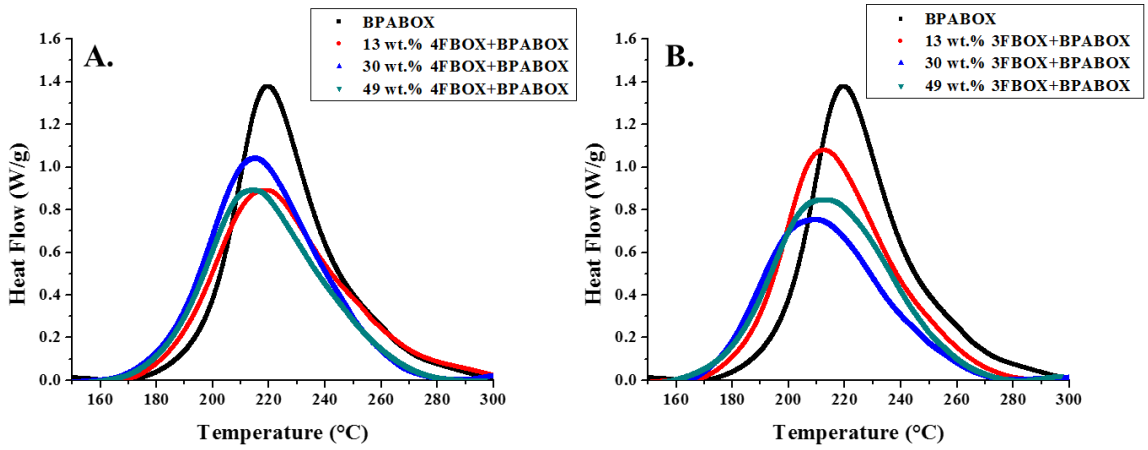

Figure 5.11 Heat flow versus temperature overlays of (A.) 4FBOX and (B.) 3FBOX alloys

Furthermore, the temperatures of the cure reaction, $Exotherm_{max}$, were also slightly shifted to lower temperatures compared to neat BPABOX as shown in Table 5.3.

Table 5.3

DSC Onset and maximum exotherm temperatures of 4FBOX and 3FBOX alloys

Alloy	**$Exotherm_{max}$ (°C)**
BPABOX	218
13 wt.% 4FBOX+BPABOX	217
30 wt.% 4FBOX+BPABOX	213
49 wt.% 4FBOX+BPABOX	211
13 wt.% 3FBOX+BPABOX	209
30 wt.% 3FBOX+BPABOX	211
49 wt.% 3FBOX+BPABOX	213

This was further evidence of the diluents providing an autocatalytic behavior, which was greater for 4FBOX than 3FBOX. In this respect, it was hypothesized that the autocatalytic behavior was greater for 4FBOX than 3FBOX. When the FBOX monomers are ring opened the presence of the fluorine and its electron withdrawing ability can increase the acidity of the phenol; therefore, catalyzing the reaction at conversions approximately greater than 60%. This was evidenced by the lower activation energies of 4FBOX alloys at conversions below 60% compared to the 3FBOX alloys, Figure 5.9 and Figure 5.10.

5.2.2 Thermal Properties

To understand the effects of isomer structure and loading level on the thermal degradation of the 3FBOX+BPABOX versus 4FBOX+BPABOX cured alloys, TGA analyses were conducted and the results are summarized in Table 5.4.

Table 5.4

Thermal stability of cured BPABOX, 3FBOX, 3FBOX, and FBOX+BPABOX alloys

Alloy	Avg. 5% Wt. Loss (°C)	Avg. 10% Wt. Loss (°C)	Avg. Char at 400 °C (%)
BPABOX	303.57 ± 0.92	327.23 ± 1.85	59.7± 1.5
4FBOX	309.76 ± 6.69	335.01 ± 4.74	63.67 ± 2.71
3FBOX	340.77 ± 1.42	377.24 ± 1.51	85.62 ± 0.38
13 wt.% 4FBOX+BPABOX	317.34 ± 0.96	336.88 ± 1.60	61.8 ± 1.5
30 wt.% 4FBOX+BPABOX	318.77 ± 1.69	339.02 ± 0.87	63.3 ± 1.1
49 wt.% 4FBOX+BPABOX	315.40 ± 2.17	341.03 ± 2.87	63.9 ± 2.3
13 wt.% 3FBOX+BPABOX	317.77 ± 5.71	340.64 ± 2.55	68.3 ± 1.0
30 wt.% 3FBOX+BPABOX	316.57 ± 5.52	339.57 ± 1.13	70.3 ± 1.9
49 wt.% 3FBOX+BPABOX	311.22 ± 8.71	339.25 ± 8.22	73.8 ± 0.5

*All specimens were analyzed in triplicate and standard deviation values are 1 standard deviation of the mean

The onset of degradation, as defined by the 5% wt. loss temperature, was increased by 2-5% for all alloys when compared to neat BPABOX. It is believed that the thermal

stability increased only slightly because the neat systems (i.e. BPABOX, 3FBOX, and 4FBOX) were all similar in thermal stability. However, the residual char increased by up to 24% for the alloys. The slight improvement in thermal stability and 24% increase in residual char are attributed to the fluorine content of the diluents. Fluorine groups are known to effectively enhance the thermal stability and char formation of polymers.[99] This attribute of fluorine was well exemplified by the similarity in thermal stability of the linear 3FBOX and 4FBOX polymer systems and the BPABOX thermoset as listed in Table 5.4.

No trends in thermal stability based on the FBOX isomer structure were apparent until 400 °C where the 3FBOX+BPABOX alloys had up to 10% more mass remaining at 400 °C than the 4FBOX+BPABOX alloys. Previous work by Low *et al.* found that degradation, or weight loss, of BOX networks up to 350 °C was a result of chain end and branching.[100, 101] In this respect, it is hypothesized that the 3FBOX alloys in this work were comprised of less branching and free volume than the 4FBOX alloys. Previous work on benzoxazine isomer effects on network properties found that the propagation of *para*-substituted oxazines were more likely to be deactivated during polymerization due to the development of intramolecular 6-membered hydrogen bonded rings than its *meta* and *ortho* isomers.[102-104] In this respect, the presence of more chain ends in the 4FBOX+BPABOX alloys can be determined by thermal and mechanical properties of the cured networks.

5.2.3 Thermomechanical Properties

The effects of reactant diluent isomer structure and loading on the neat BPABOX glassy network properties were studied via DMA. The unimodal nature of the α-

transition peaks around 180 °C of the Tanδ curves in Figure 5.12 provide additional evidence that the alloys were in fact miscible and did not result in phase separation upon cure.

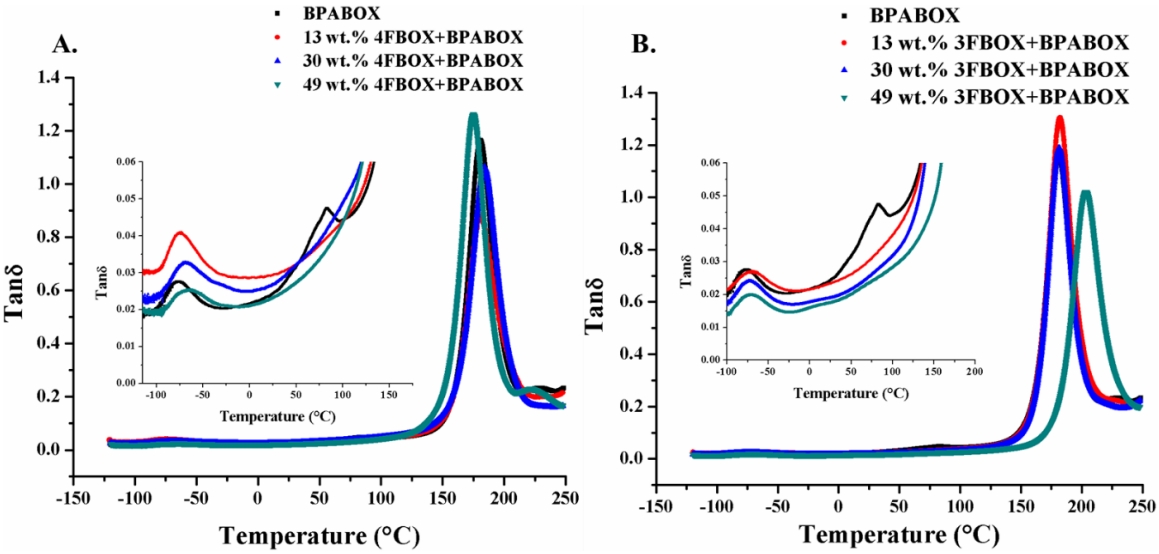

Figure 5.12 DMA data at 1.0 Hz for (A.) 4FBOX and (B.) 3FBOX alloys for T_g, v_e, and M_c determinations. Glass thermal transitions (β and γ) are zoomed in the insets

This was further confirmed by atomic force microscopy where no phase separation or void content was observed in the cured specimens, Figure 5.13.

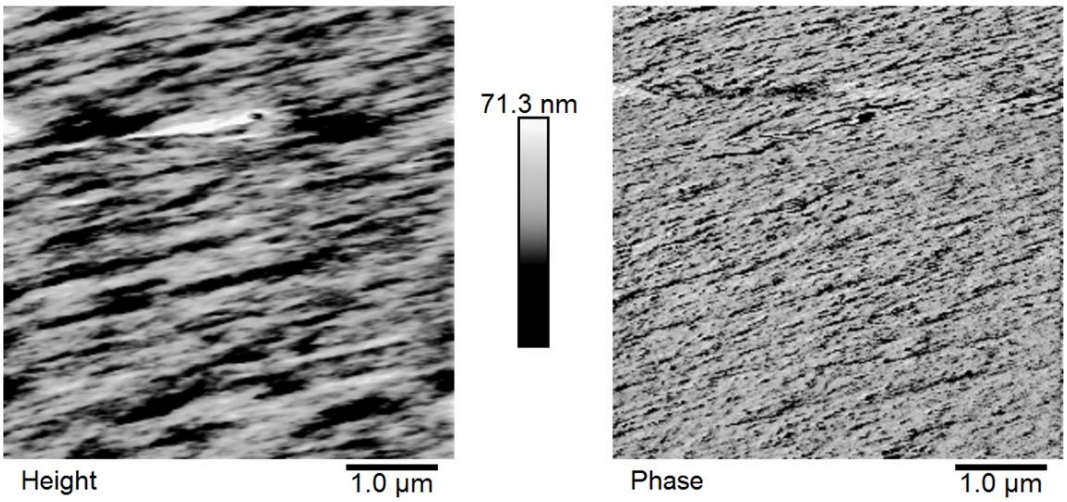

Figure 5.13 AFM phase micrograph of a cured 30% 3FBOX+BPABOX sample

The data from DMA analyses conducted at 1.0 Hz was used to determine the T_g, crosslink density (v_e), and molecular weight between crosslinks (M_c) for each alloy. These values are listed in Table 5.5. Interestingly, the T_g values for both the 3FBOX and 4FBOX alloys remained relatively unchanged with increasing diluent loading as compared to the neat BPABOX until a critical loading, or 49 wt.%. This was unexpected because the magnitude of the α-transition is a measure of the long-range segmental mobility in the cured network. In this respect, it would be expected that said mobility would theoretically increase with increasing monofunctional diluent loading due to the reduction in crosslink density. Consequently, the α-transition, or T_g, was expected to decrease to lower temperatures because said long-range mobility should be easier to achieve at lower temperatures.[105] Contradicting, the crosslink densities calculated from the rubbery moduli, Figure 5.15, remained relatively unchanged despite the increase in molecular weight between crosslinks with diluent loading. Since the T_g values and crosslink densities were unchanged for 4FBOX and 3FBOX alloys to 30 wt.%, the

stiffness of the segments between crosslinks was attributed to the additional fluorine content and increased secondary interactions of the FBOX diluents compared to neat BPABOX.

Table 5.5

T_g, v_e, and M_c results from DMA analyses at 1.0 Hz

Alloy	**ρ_{Avg} (g/cm^3)**	**T_g (°C)**	**$E_r'_{Tg+40}$ (MPa)**	**v_e x10^{-3} (mol/cm^3)**	**M_c (g/mol)**
BPABOX	1.178	180.83	11	2	585
13 wt.% 4FBOX+BPABOX	1.180	180.69	12	2.1	561
30 wt.% 4FBOX+BPABOX	1.192	184.14	11	2	600
49 wt.% 4FBOX+BPABOX	1.198	174.92	8	1.5	798
13 wt.% 3FBOX+BPABOX	1.187	182.02	11	2.1	580
30 wt.% 3FBOX+BPABOX	1.193	181.21	10	1.8	672
49 wt.% 3FBOX+BPABOX	1.189	203.1	12	2	610

It is well reported that the rigidity of polymers can be increased by the addition of fluorinated substituents, which restrict modes of rotation through intermolecular interactions and steric effects.[65, 106, 107] Similarly, the segments between crosslinks in the BOX alloys were stiffened and intermolecular interactions were increased due to the added fluorine, which prevented network plasticization of the BOX alloys up to 30 wt.%. This is further supported by the relatively unchanged glassy moduli of the alloys compared to the neat BPABOX, Figure 5.15. Furthermore, stiffening of the M_c portions

via fluorination was well supported by the measured T_g via of the diluent linear polymer via DMA, which for example was 231.99 °C for neat 3FBOX. Although used for random miscible copolymers, the Fox Equation, or Equation 13, has been used as a method to predict the T_g of bi-component thermoset systems.[20, 108, 109]

$$\frac{1}{T_g} = \frac{w_1}{T_{g,1}} + \frac{w_2}{T_{g,2}} \qquad \text{(Equation 13)}$$

In this equation, the T_g of the bi-component system, $\frac{1}{T_g}$, is predicted based on the weight fractions, w_1 and w_2, and the neat T_g values, $T_{g,1}$ and $T_{g,2}$ of each component. When neglecting the presence of crosslinks and applied to the 3FBOX+BPABOX alloys for example, less than 6% error was calculated between the measured and predicted T_g values as shown in Figure 5.14.

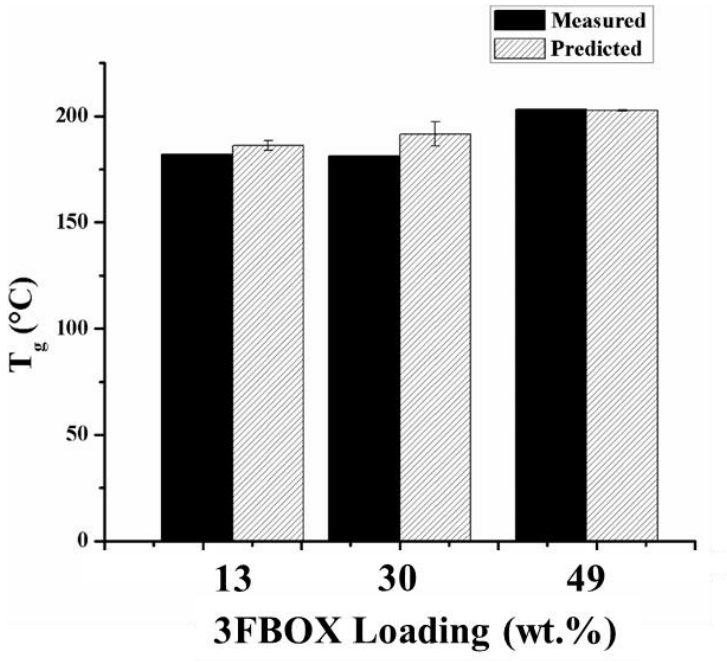

Figure 5.14 Measured versus Predicted Tg values for 3FBOX+BPABOX cured alloys

*Errors bars are representative of the deviations between the measured and predicted values

The excellent agreement between the experimental T_g data and predicted T_g values demonstrates the ability to tailor BOX network properties as a function of comonomer composition with great predictability using the Fox equation. Attempts to polymerize neat 4FBOX DMA samples were made by traditional casting methods (i.e. silicon mold and compression mold) using degassed alloys as described in Chapter II, but the samples were too brittle to remove from the molds and often times shattered while cooling after the cure prescription was complete. Future work should include investigating the effect of ramp rate and polymerization cycle on the volumetric changes of polymerized or cured specimens in this work. To demonstrate the stiffness afforded by fluorinated segments between crosslinks however, the T_g of 3FBOX provided the confidence needed to support this claim.

Additionally, fluorine is strongly withdrawing in electronic nature, which can increase the acidity of adjacent hydrogen atoms and subsequently their hydrogen bonding capabilities.[110, 111] Fluorine's ability to serve as a hydrogen bond acceptor has been under debate[112-114] despite the published evidence.[114-118] Moreover, reports have demonstrated that enhancing the strength of hydrogen bonding can afford physical crosslinks, or through-space hydrogen bonding.[114, 119, 120] It is for this reason that the author also believes the experimental crosslink densities were preserved for all alloys, despite the theoretical reduction in crosslink density with increasing diluent loading up to 30 wt.% and the increase in molecular weight between crosslinks.

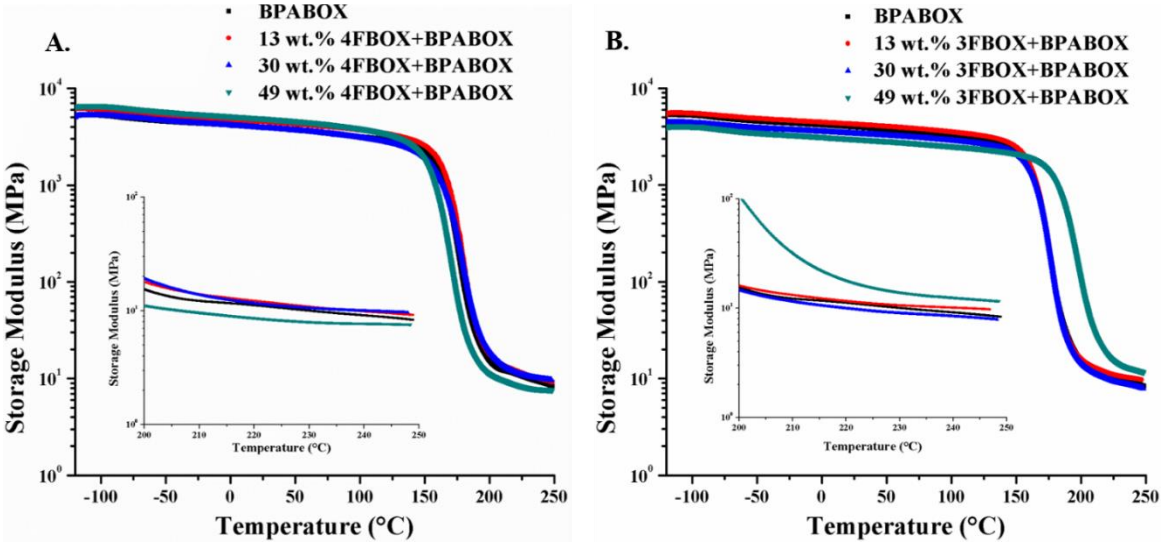

Figure 5.15 Storage moduli overlay of (A.) 4FBOX alloys and (B.) 3FBOX alloys with insets zoomed into their rubbery moduli from DMA data at 1.0 Hz

At the highest diluent loading (49 wt.%) the isomer structure clearly had an effect on the matrix properties. The 4FBOX alloy demonstrated the expected plasticization behavior as indicated by a 6 °C reduction in T_g, whereas the 3FBOX alloy T_g increased

by 22 °C. Misasi *et al.* demonstrated a similar increase in T_g with meta-substituted aryletherketone diamine curatives and epoxy matrices. It was reported that the meta-substituted linkage afforded additional conformations forming kinks or coils, which yielded increased molecular packing, or reduced free volume.[120] Though free volume measurements are not reported in this work, the similar characteristic behavior can be attributed to the elevated rubbery storage modulus of the 3FBOX versus 4FBOX alloy at 49 wt.%, Figure 5.15. Despite the matrix properties attributed to isomer structure effects at 49 wt.%, the other loadings demonstrated no reduction in T_g or storage moduli despite the increase in molecular mobility, or molecular weight between crosslinks. These findings could afford the potential of "toughening", or improving the glassy-state energy dissipation, of the brittle BOX networks without the need to add and disperse fillers or reinforcements. Toughness is quantified by the energy that can be absorbed by a system prior to fracture, which can be associated to the activation energies of glassy-state molecular relaxations, or mobilities.

Molecular relaxations are temperature and frequency dependent motions that follow Arrhenius-type relationships.[121] Activation energies for the primary relaxation (i.e. α) and sub-T_g relaxations (i.e. β and γ) were measured using dynamic mechanical analysis and calculated from the slope of Arrhenius plots by plotting $\mathrm{Log}(\frac{f}{f_0})$ versus $\frac{1000}{T}$. Primary relaxations, or long-range segmental mobility, are characterized by the α-transition. Cooperative motions are characteristic of β-transitions and controlled by symmetry, backbone rigidity, and steric hindrance.[122] Simple motions are characteristic of γ-transitions and controlled by short-range motions such as substituent rotations and

crank-shaft motions.[121] The activation energies for these network relaxations were calculated for each alloy and are summarized in Table 5.6. As expected, the activation energies for the α-transition ($Ea_{T\alpha}$) were relatively unchanged within the error until 49 wt.% where a ~20 kJ/mol decrease in Ea was calculated for the 4FBOX+BPABOX alloy. This finding correlates well with the plasticized T_g reported in Table 5.5, whereas the 3FBOX+BPABOX was hypothesized to increase due to the increase in T_g. It remains unclear why said increase did not occur with repeatability.

Notably, the activation energy for the β-transition ($Ea_{T\beta}$) could only be measured in the neat BPABOX. Ning *et al.* found that a broad β-transition was characteristic in the temperature range between 10 - 100 °C of the neat BPABOX network. The breadth was attributed to defects, or unconsumed chain ends and short-chain branching in the cured network.[16] Similarly, the neat BPABOX network in this work exhibited similar behavior and the incomplete polymerization affording network defects was quantified by its 71% degree of cure, Table 5.2. Previous work reported that the β-transition can become negligible due to increased molecular packing or reduced network defects.[4, 123] Both of these reasons are plausible for the disappearance of the β-transition in all FBOX+BPABOX alloys.

Table 5.6

Activation energies (Ea) calculated from DMA analyses at 0.1, 1.0, 10, and 100 Hz

Alloy	**$Ea_{T\alpha}$ (kJ mol^{-1})**	**$Ea_{T\beta}$ (kJ mol^{-1})**	**$Ea_{T\gamma}$ (kJ mol^{-1})**
BPABOX	89.1	41.6	10.1
13 wt.% 4FBOX+BPABOX	82.1	-	0.6
30 wt.% 4FBOX+BPABOX	86.1	-	0.8
49 wt.% 4FBOX+BPABOX	68.9	-	0.9
13 wt.% 3FBOX+BPABOX	84.5	-	0.8
30 wt.% 3FBOX+BPABOX	81.4	-	0.9
49 wt.% 3FBOX+BPABOX	87.9	-	0.9

*87-99% accounted variance in the regression models

Wang *et al.* reported that the addition of reactive BOX diluents substituted at the meta and para positions on the phenolic portion afforded additional reactive sites causing network defects, or incomplete BPABOX network formation.[4] Despite reports that the benzoxazine polymerization preferentially propagates from the ortho position adjacent to the phenol, Douglas *et al.* demonstrated that the para position is also an available reaction site.[5] Furthermore, halogens are considered deactivating substituents due to inductive electron withdrawing, but they are also capable of resonance donating affording ortho and para directing for electrophilic aromatic substitutions.[124] It is for these reasons that the author hypothesizes that there would be less defects in the 3FBOX versus the 4FBOX alloys, as both the ortho and para positions are unsubstituted on the 3FBOX reactive

diluent. Moreover, the degree of cures for the FBOX+BPABOX alloys were lower than the BPABOX; thus, providing evidence that increased secondary interactions (i.e. hydrogen bonding and π-π stacking) could be increasing molecular-level cohesion in the network and reducing the β-transition.

The activation energies for the γ-transitions ($Ea_{T\gamma}$), however, were 2 orders of magnitude lower for all FBOX+BPABOX alloys than the neat BPABOX. Despite the differences in T_g, or α-transition, between the FBOX isomer alloys at 49 wt.%, no correlation or trend was expected for the γ-transitions. This was expected due to the increase in molecular weight between crosslinks, which afforded increased molecular mobility and short-range interactions. The enhanced glassy-state mobility provided an opportunity to toughen the inherently brittle matrix properties of BPABOX.

5.2.4 Mechanical Properties

Sub-Tg relaxations (i.e. β and γ) are associated with the polymer network's ability to dissipate energy, or resist deformation, in the glassy state and were tested via uniaxial compression.[43] Although DMA and compression testing do not directly scale, trends and comparative reasoning for molecular mobility can be made between the techniques. The room temperature uniaxial compression results are plotted in Figure 5.16 and summarized in Table 5.7.

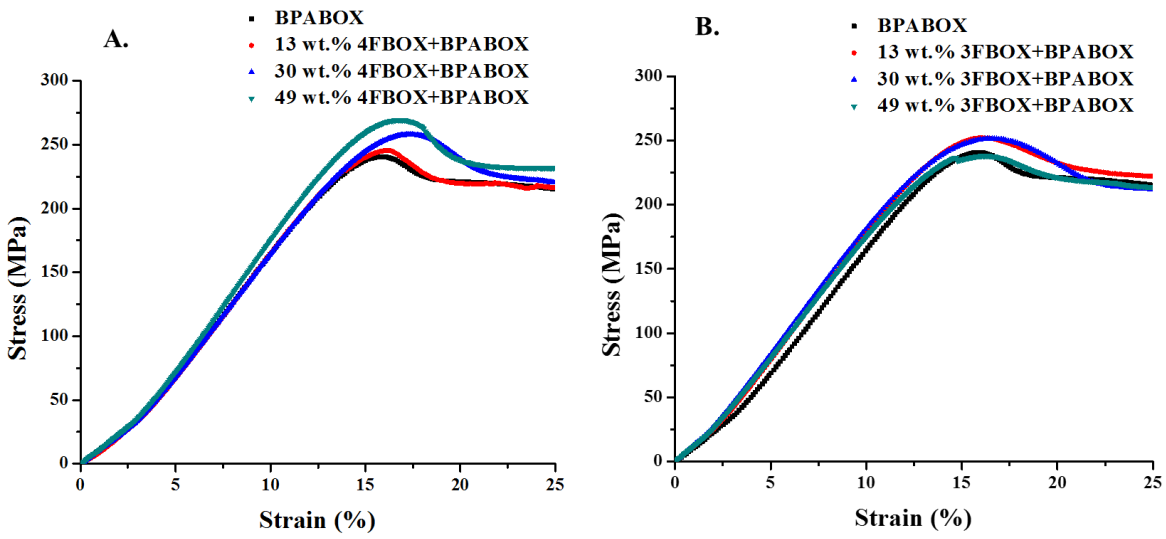

Figure 5.16 Room temperature uniaxial compression stress versus strain results for (A.) 3FBOX and (B.) 4FBOX alloys

The average Young's moduli remained relatively unchanged within the experimental error, which was expected as the glassy storage moduli from DMA testing were also unchanged. The average yield strain increased by ~14-26% for the alloys, but there was no relationship between said increase and the FBOX isomer structure. Mayr *et al.* reported that yield strength in glassy epoxy thermosets decreases with increasing molecular weight between crosslinks due to the reduction of molecular-level units involved in the network while yielding.[125] This finding was associating the dependency of yield strain on crosslink junctions and the structural units between them. Interestingly, all FBOX+BPABOX alloys demonstrated the opposite effect of the findings by Mayr as an increase in yield strength was achieved despite the increase in molecular weight between crosslinks. Similar to the findings in this work, Misasi *et al.* reported an increase in yield strain in aryletherketone amine/epoxy matrices despite an increase in molecular weight between crosslinks.[120] This was attributed to the fact that the number

and chemical composition of crosslink junctions theoretically remained unchanged and provided the potential for energy dissipation without yielding. In this respect, the calculated crosslink densities for all FBOX+BPABOX alloys remained unchanged and their reduced DOC afford the mobility for enhanced secondary interactions and cohesive energy in the cured network. Stronger secondary interactions are clearly demonstrated in Figure 5.16 by the increase in maximum yield stress up for all FBOX alloys as compared to the neat BPABOX.

Table 5.7

Mechanical properties of BOX alloy networks from uniaxial compression

Alloy	**Avg. Young's Modulus (MPa)**	**Avg. Yield Strain (%)**	**Avg. Toughness (MPa)**
BPABOX	1962 ± 6	14.1 ± 0.2	4003 ± 18
13 wt.% 4FBOX+BPABOX	1989 ± 29	16.2 ± 0.5	3986 ± 101
30 wt.% 4FBOX+BPABOX	1949 ± 48	17.6 ± 0.3	4174 ± 89
49 wt.% 4FBOX+BPABOX	2067 ± 73	16.8 ± 0.1	4343 ± 52
13 wt.% 3FBOX+BPABOX	2024 ± 21	15.8 ± 0.8	4304 ± 56
30 wt.% 3FBOX+BPABOX	2051 ± 47	16.0 ± 0.3	4336 ± 55
49 wt.% 3FBOX+BPABOX	1940 ± 49	16.1 ± 0.9	4133 ± 168

*All specimens were analyzed in quadruplicate and standard deviation values are 1 standard deviation of the mean

The influence of the semi-rigid segments between crosslinks resulting from fluorination that enhanced the molecular-level mobility and increased the secondary interactions could provide energy dissipation modes to toughen the inherently brittle neat BPABOX network. Previous work in thiol-trifluorovinyl ether networks demonstrated that semifluorinated linkages provided hydrogen bonding sites that could serve as physical crosslinks.[126] Said physical crosslinks were believed to absorb the energy of mechanical deformation and rupture prior to covalent bonds, which provided a toughened network. Toughness is considered the resiliency of a material to deformation, which can be measured by integrating the area under the stress versus strain curve up to fracture.[50] Toughness results in Table 5.7 for the 3FBOX+BPABOX and 4FBOX+BPABOX alloys demonstrated up to an 8% and 9% increase, respectively, in toughness as compared to the neat BPABOX. The increase in toughness is attributed to the increased secondary interactions and molecular mobility between crosslinks due to the incorporation of the reactive diluents. Furthermore, the author hypothesizes that the increase in modulus and toughness in the 3FBOX+BPABOX alloys compared to the 4FBOX+BPABOX alloys could be due to the increased molecular packing afforded by "sagging" and "filling" of free volume under strain due to the meta-substituted linkages of the 3FBOX diluent. To confirm this hypothesis, free volume measurements on the cured specimens will be the next phase of this work.

5.3 Conclusions

The use of fluorinated monofunctional reactive diluents to prepare BOX alloys allows for a balance of processability while maintaining, or improving, matrix properties were demonstrated in this work. Parallel plate rheology was used to quantify the

processability of the BOX alloys, where temperature ramp experiments showed that the addition of fluorinated reactive diluents improved the processability of the alloys by lowering the viscosity at elevated temperatures to a processable range. TGA results indicated that the addition of the fluorinated monofunctional diluents improved the thermal stability of the BOX matrix due to the enhanced thermal stability of the fluorinated segments compared to neat BPABOX segments. DMA experiments were conducted to study the glassy network properties of the BOX alloys, where a unimodal α - transition peak, observed at 180 °C, provided evidence of homogeneous networks. It was found that an increase in monofunctional diluent loading level did not influence the calculated crosslink density or onset temperature of the α - transition peak. This finding was attributed to the highly fluorinated segments that yielded an increase in stiffness between crosslinks as well as an increase in secondary interactions, which acted as physical crosslinks. Compression testing results demonstrated that the addition of fluorinated mono-functional reactive diluents increased the yield strain and toughness with relatively no influence on Young's moduli when compared to neat BPABOX. These findings suggest that the BOX alloys in this work expand the possible applications for polybenzoxazines by increasing the strain capability of the matrix on the bimolecular level without sacrificing T_g and modulus.

Future work will include investigating the network morphologies of alloys from this chapter and their dependency on ramp rate during cure. Using thermal gravimetric analysis coupled with mass spectroscopy, rheokinetics, and insitu-IR, one could better understand the network architecture as a function of cure time and temperature. This knowledge should be further supported by molecular dynamics simulations from software

supplied by Schrödinger® to explain and predict the effects of network architecture on the bulk mechanical properties.

APPENDIX A – STRUCTURAL VALIDATIONS OF SYNTHESIZED BENZOXAZINES

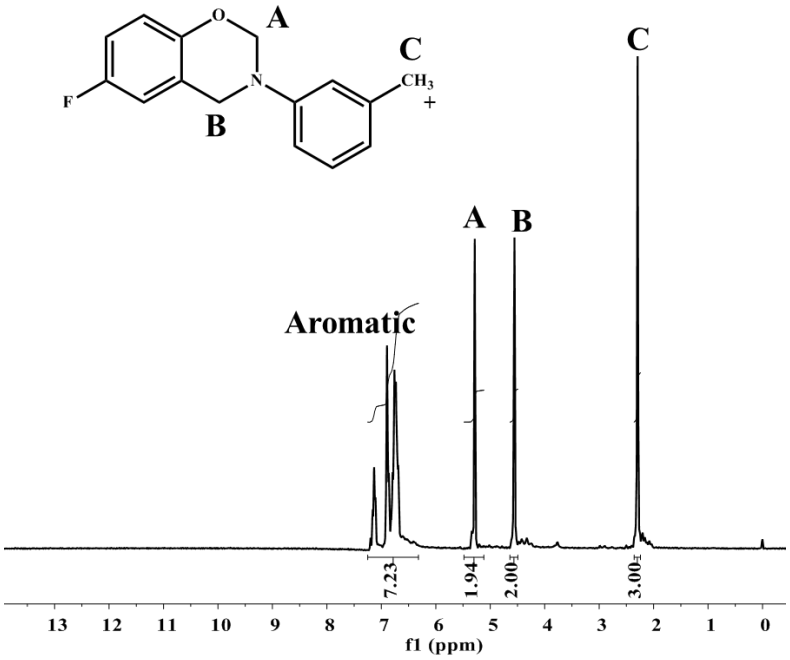

Figure A.1 Proton NMR spectrum of 4FBOX-BR. ^{1}H NMR ($CDCl_3$), ppm: δ= 2.29 (3H, s, CH_3), 4.56 (2H, s, -N-CH_2-Ar-), 5.29 (2H, s, -O-CH_2-N-), 6.90 (7H, m, aromatic)

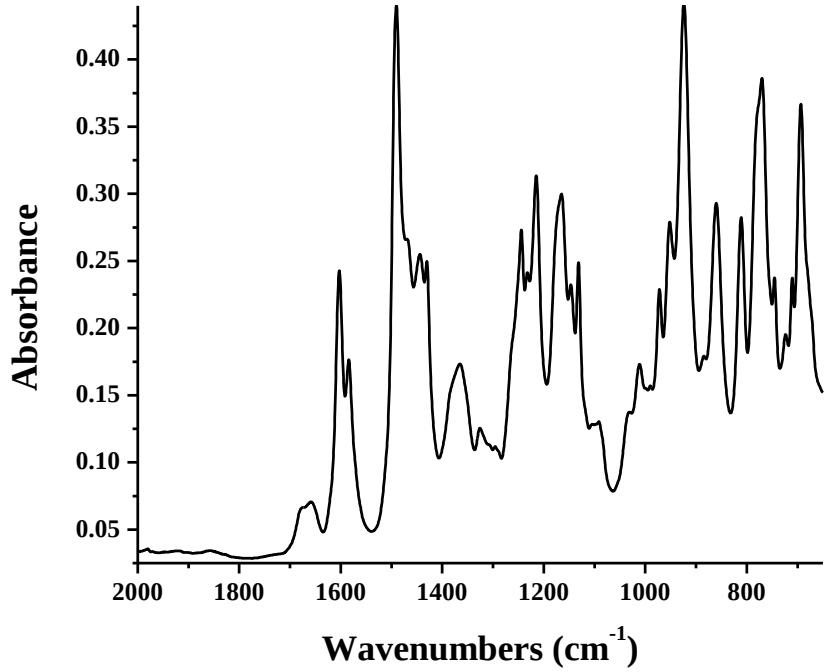

Figure A.2 ATR-FTIR spectrum of 4FBOX-BR. FTIR (KBr) v: asymmetric stretching at 1244 cm^{-1} and symmetric stretching at 1131 cm^{-1} of ether bond in the BOX moiety, BOX moiety at 923 cm^{-1}, and tri-substituted benzene at 860 cm^{-1}

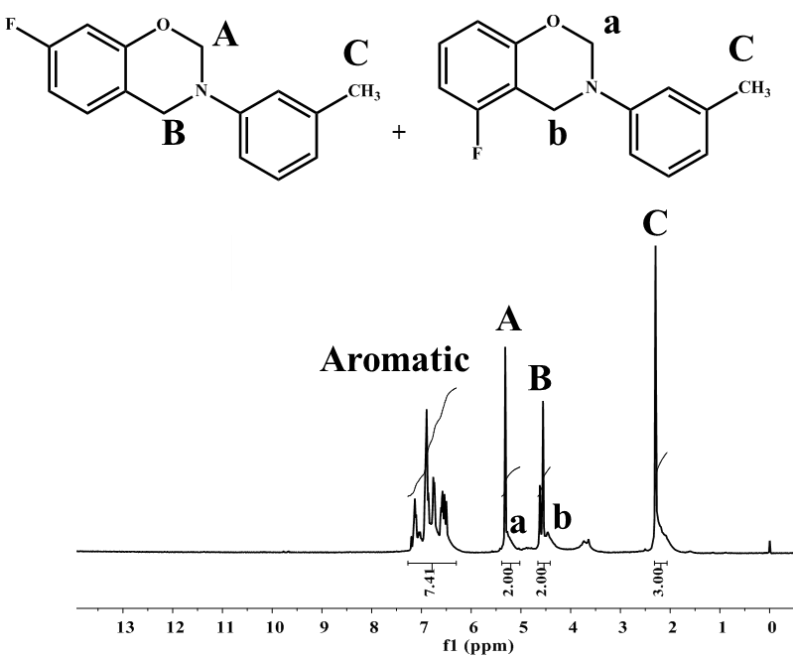

Figure A.3 Proton NMR spectrum of 3FBOX-BR. ^{1}H NMR ($CDCl_3$), ppm: δ= 2.30 (3H, s, CH_3), 4.62 (2H, s, -N-CH_2-Ar-), 5.32 (2H, s, -O-CH_2-N-), 6.90 (7H, m, aromatic)

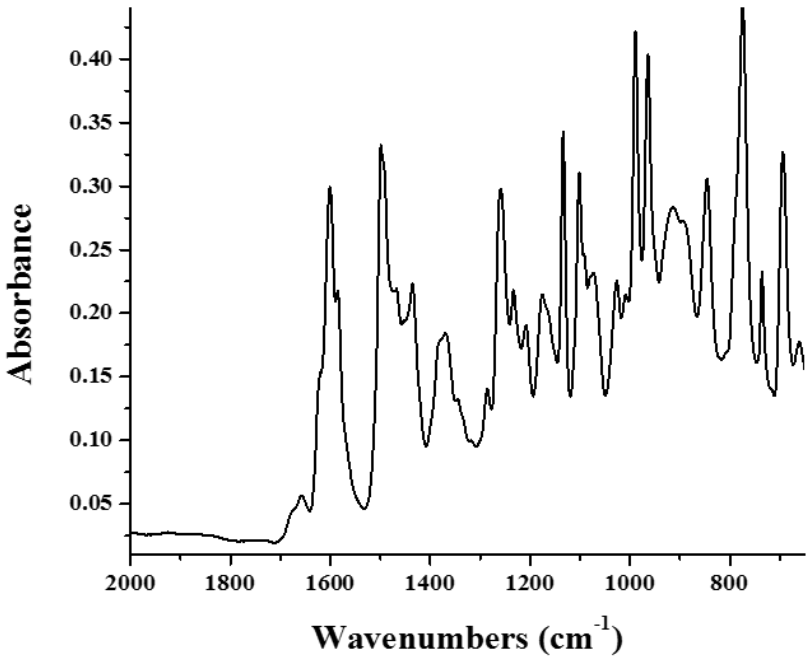

Figure A.4 ATR-FTIR spectrum of 3FBOX-BR. FTIR (KBr) v: asymmetric stretching at 1259 cm^{-1} and symmetric stretching at 1134 cm^{-1} of ether bond in the BOX moiety, BOX moiety at 914 cm^{-1}, and tri-substituted benzene at 846 cm^{-1}

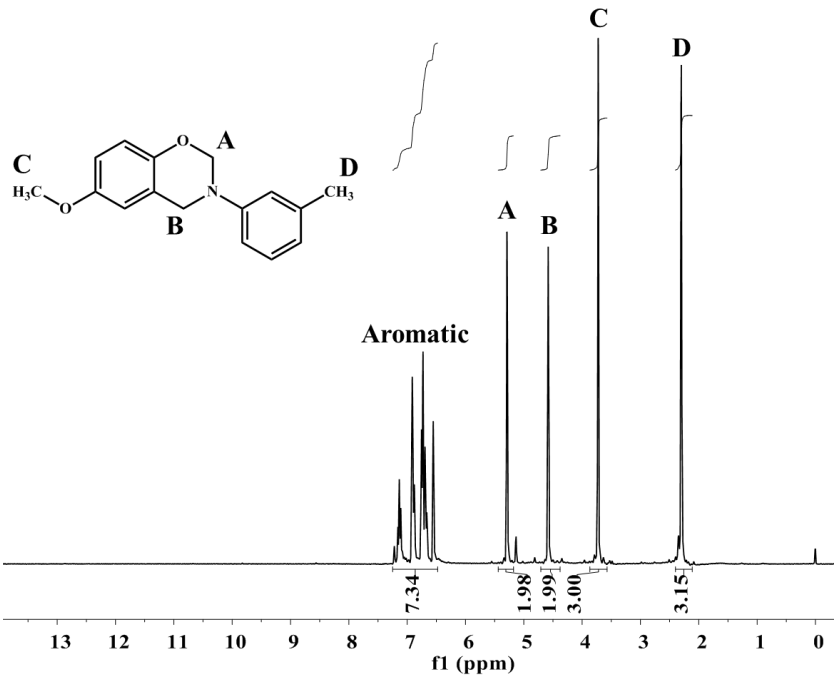

Figure A.5 Proton NMR spectrum of 4MBOX-lab-scale CHSR. ^{1}H NMR ($CDCl_3$), ppm: δ= 2.36 (3H, s, CH_3), 3.78 (3H, s, -O-CH_3), 4.64 (2H, s, -N-CH_2-Ar-), 5.34 (2H, s, -O-CH_2-N-), 6.92 (7H, m, aromatic)

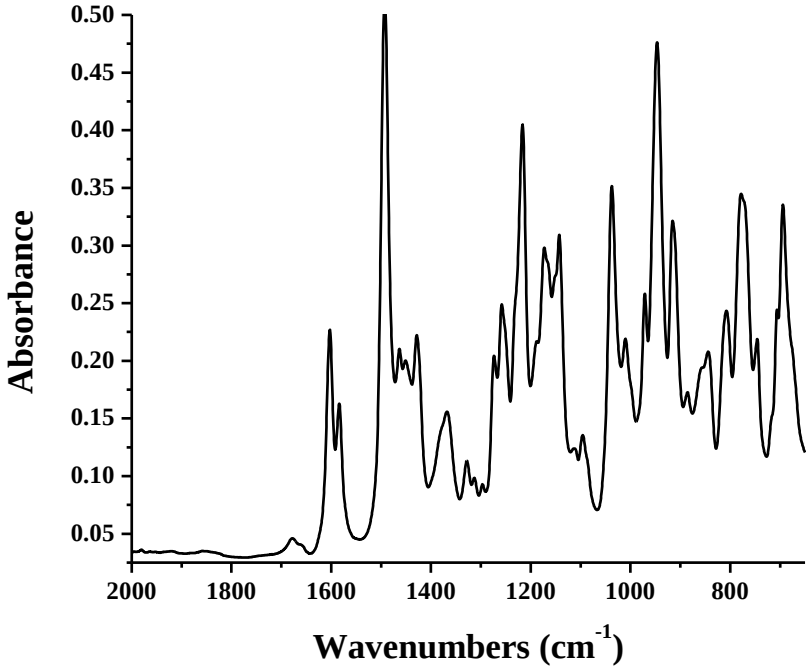

Figure A.6 ATR-FTIR spectrum of 4MBOX-lab-scale CHSR. FTIR (KBr) v: asymmetric stretching at 1493 cm^{-1} and symmetric stretching at 1216 cm^{-1} of ether bond in the BOX moiety, BOX moiety at 947 cm^{-1}, and tri-substituted benzene at 844 cm^{-1}

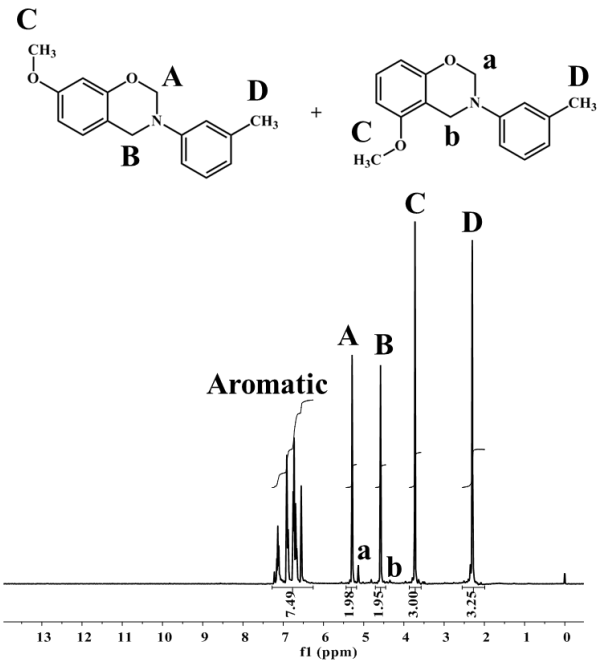

Figure A.7 Proton NMR spectrum of 3MBOX-BR. ^{1}H NMR ($CDCl_3$), ppm: δ= 2.30 (3H, s, CH_3), 3.72 (3H, s, -O-CH_3), 4.58 (2H, s, -N-CH_2-Ar-), 5.29 (2H, s, -O-CH_2-N-), 6.91 (7H, m, aromatic)

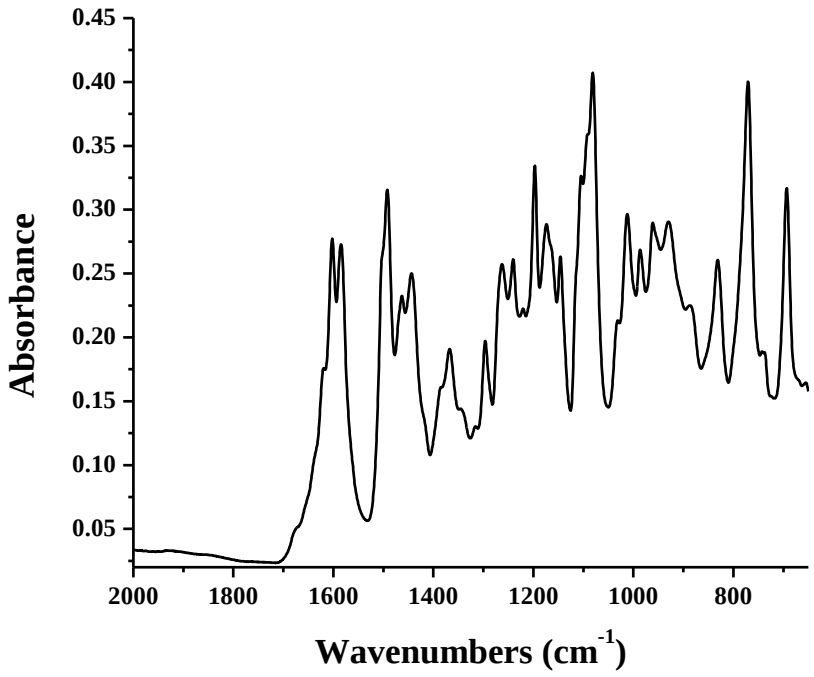

Figure A.8 ATR-FTIR spectrum of 3MBOX-BR. FTIR (KBr) v: asymmetric stretching at 1492 cm^{-1} and symmetric stretching at 1197 cm^{-1} of ether bond in the BOX moiety, BOX moiety at 929 cm^{-1}, and tri-substituted benzene at 831 cm^{-1}

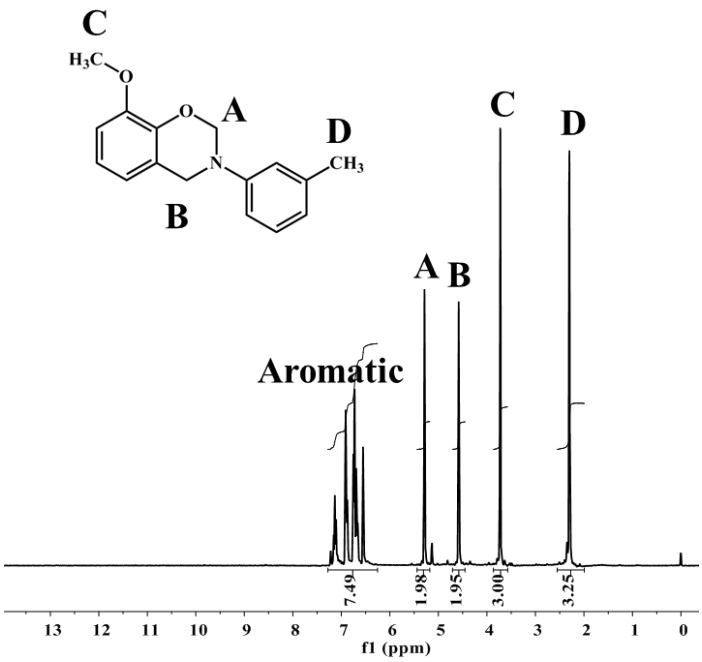

Figure A.9 Proton NMR spectrum of 2MBOX-BR. ^{1}H NMR ($CDCl_3$), ppm: δ= 2.28 (3H, s, CH_3), 3.82 (3H, s, -O-CH_3), 4.60 (2H, s, -N-CH_2-Ar-), 5.41 (2H, s, -O-CH_2-N-), 6.91 (7H, m, aromatic)

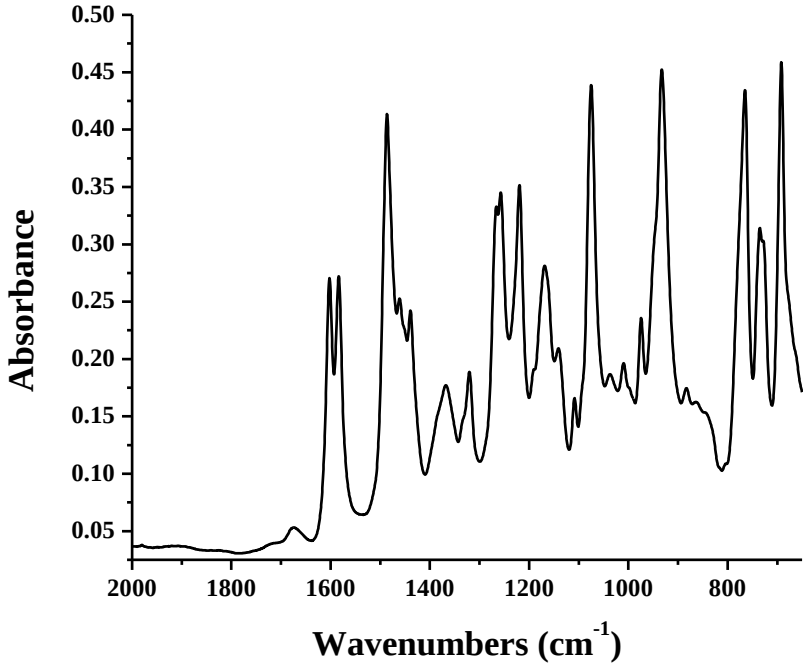

Figure A.10 ATR-FTIR spectrum of 2MBOX-BR. FTIR (KBr) v: asymmetric stretching at 1486 cm^{-1} and symmetric stretching at 1168 cm^{-1} of ether bond in the BOX moiety, BOX moiety at 932 cm^{-1}, and tri-substituted benzene at 765 cm^{-1}

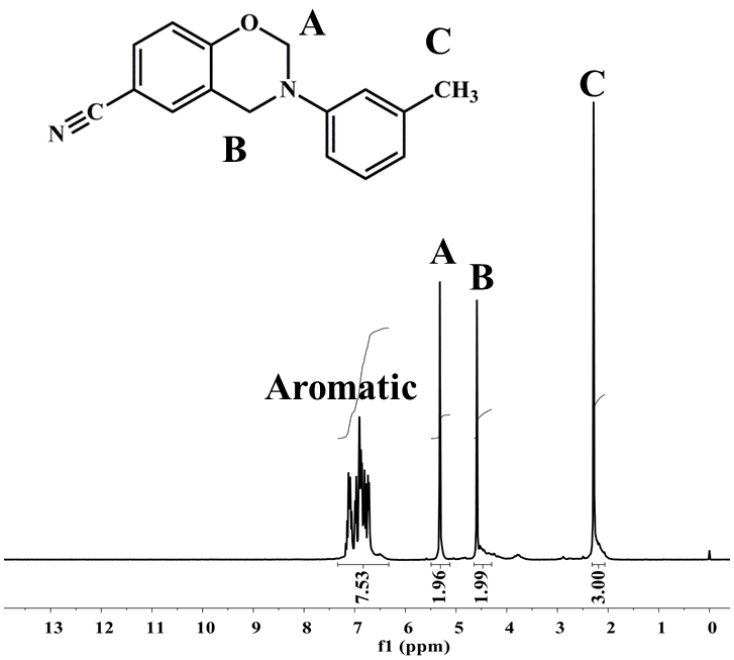

Figure A.11 Proton NMR spectrum of 4CyBOX-BR. ^{1}H NMR ($CDCl_3$), ppm: δ= 2.33 (3H, s, CH_3), 4.64 (2H, s, -N-CH_2-Ar-), 5.43 (2H, s, -O-CH_2-N-), 7.04 (7H, m, aromatic)

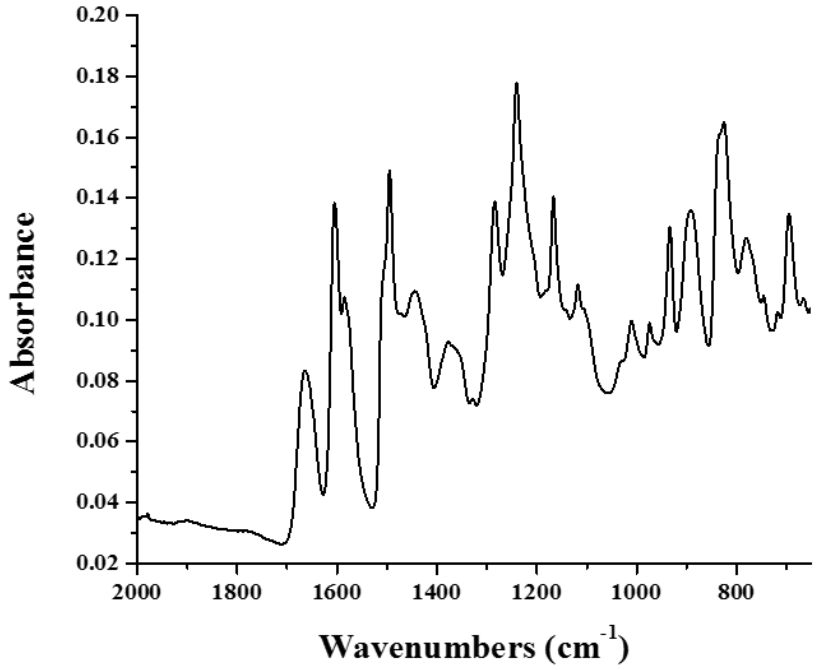

Figure A.12 ATR-FTIR spectrum of 4CyBOX-BR. FTIR (KBr) v: Asymmetric stretching at 1240 cm^{-1} and symmetric stretching at 1178 cm^{-1} of ether bond in the BOX moiety, BOX moiety at 933 cm^{-1}, and tri-substituted benzene at 891 cm^{-1}

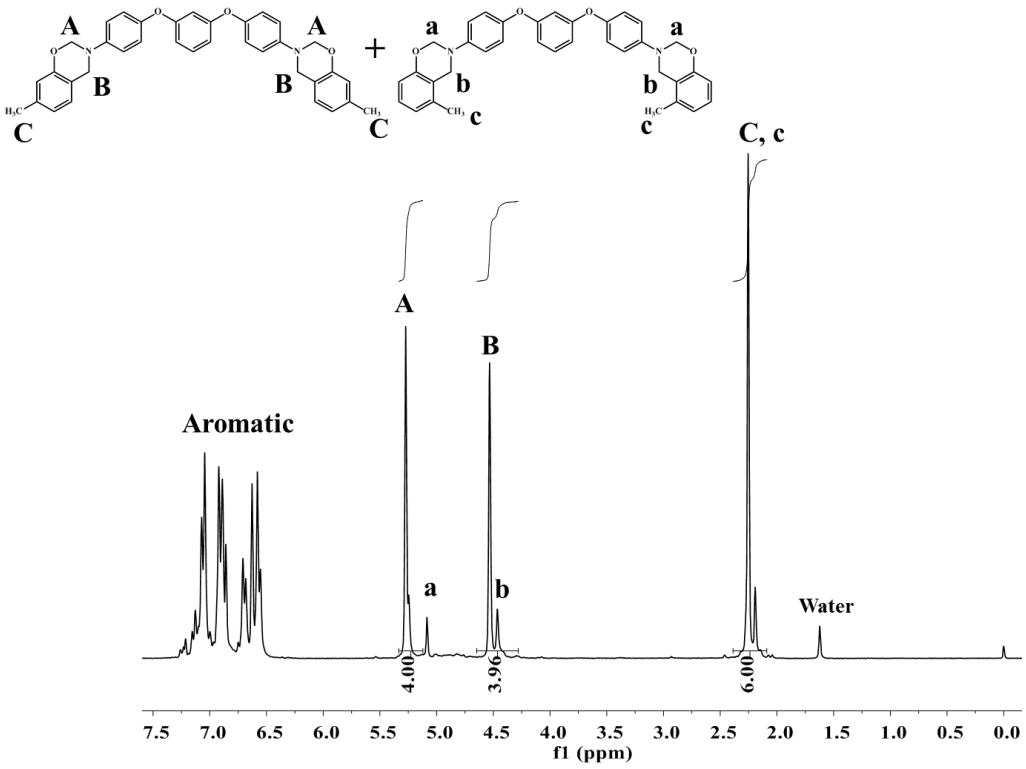

Figure A.13 Proton NMR spectrum of DiBOX-lab-scale CHSR. ^{1}H NMR ($CDCl_3$), ppm: δ= 2.25 (6H, s, CH_3), 4.53 (4H, s, -N-CH_2-Ar-), 5.27 (4H, s, -O-CH_2-N-), 6.92 (18H, m, aromatic)

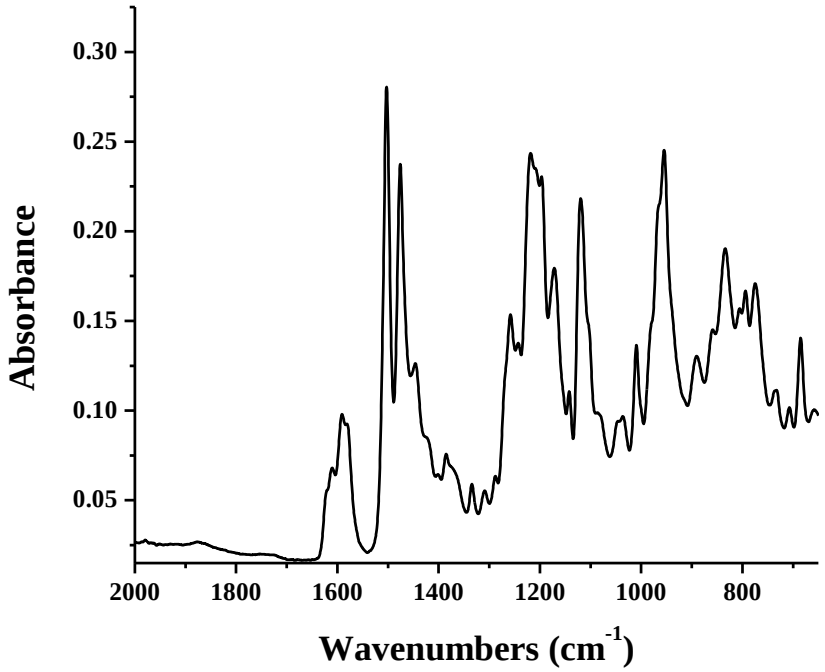

Figure A.14 ATR-FTIR spectrum of DiBOX-lab-scale CHSR. FTIR (KBr) v: asymmetric stretching at 1240 cm^{-1} and symmetric stretching at 1178 cm^{-1} of ether bond in the BOX moiety, BOX moiety at 955 cm

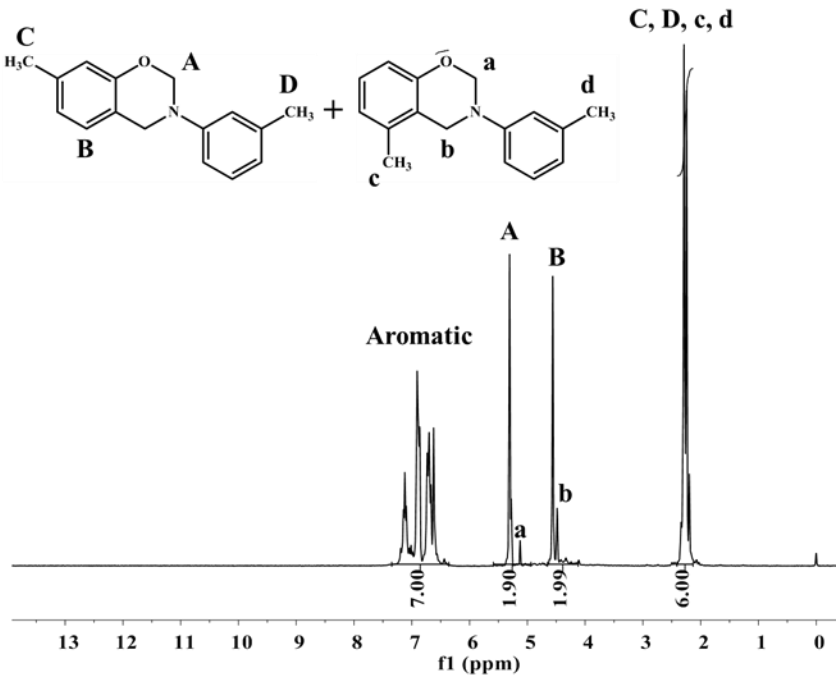

Figure A.15 Proton NMR spectrum of mCmTBOX-lab-scale CHSR. ^{1}H NMR spectrum of mCmTBOX. ^{1}H NMR ($CDCl_3$), ppm: δ= 2.29 (6H, s, CH_3), 4.56 (2H, s, -N-CH_2-Ar-), 5.31 (2H, s, -O-CH_2-N-), 6.86 (18H, m, aromatic)

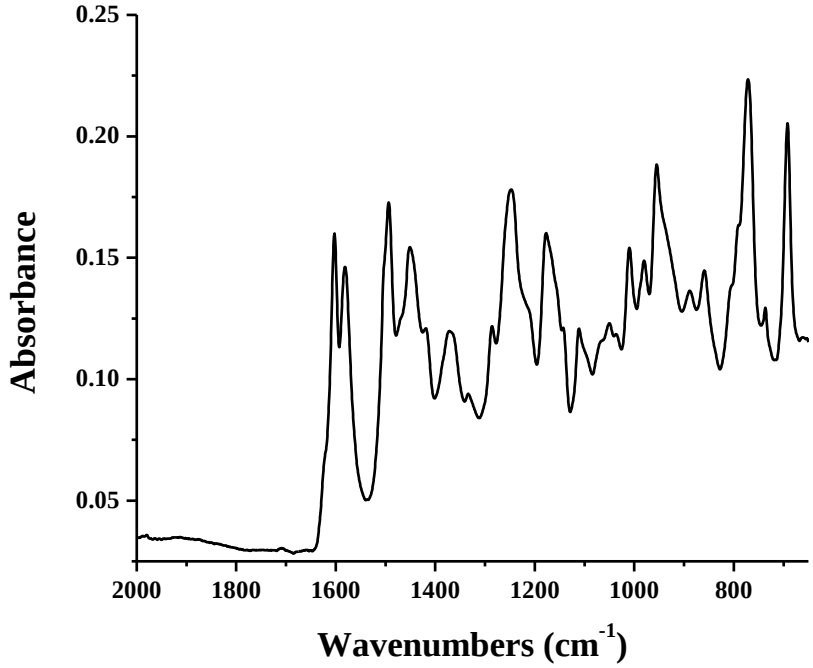

Figure A.16 ATR-FTIR spectrum of mCmTBOX-lab-scale CHSR. FTIR (KBr) v: asymmetric stretching at 1247 cm^{-1} and symmetric stretching at 1177 cm^{-1} of ether bond in the BOX moiety, BOX moiety at 955 cm^{-1}, and tri-substituted benzene at 859 cm^{-1}

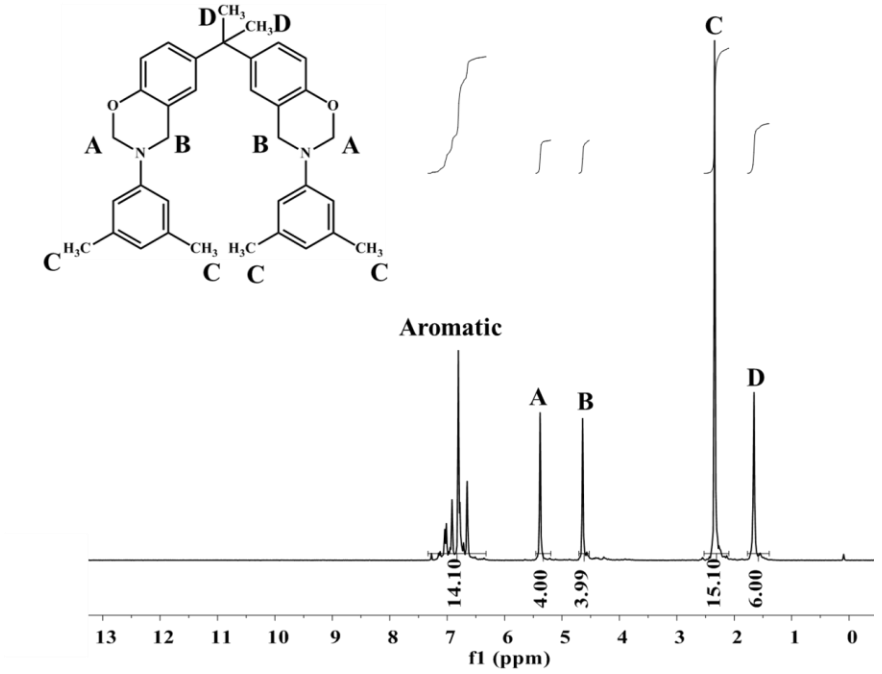

Figure A.17 Proton NMR spectrum of 3,5DMABPABOX-pilot-scale CHSR. ^{1}H NMR spectrum of 3,5DMABPABOX. ^{1}H NMR ($CDCl_3$), ppm: δ= 1.66 (6H, s, germinal $2CH_3$), 2.34 (15H, s, aryl $2CH_3$), 4.64 (4H, s, -N-CH_2-Ar-), 5.38 (4H, s, -O-CH_2-N-), 6.81 (14H, m, aromatic)

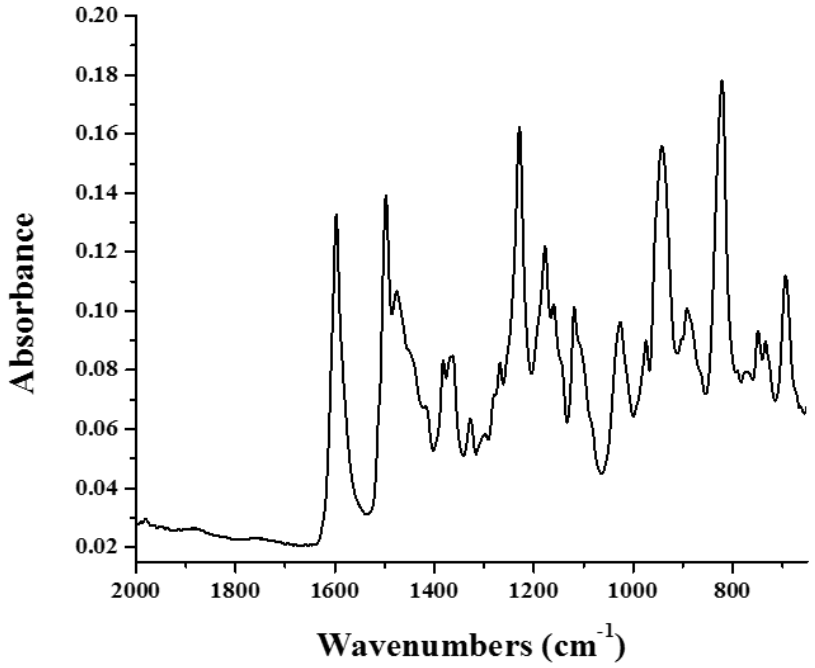

Figure A.18 ATR-FTIR spectrum of 3,5DMABPABOX-pilot scale CHSR. FTIR (KBr) v: asymmetric stretching at 1228 cm^{-1} and symmetric stretching at 1178 cm^{-1} of ether bond in the BOX moiety, BOX moiety at 942 cm^{-1}, and tri-substituted benzene at 1597 and 821 cm^{-1}

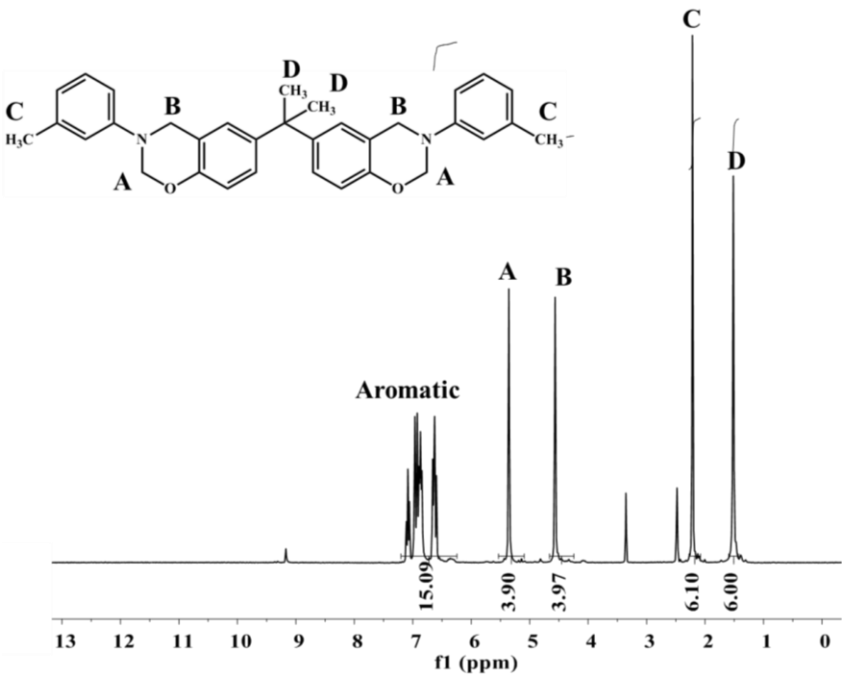

Figure A.19 Proton NMR spectrum of mTBPABOX-lab-scale CHSR. ^{1}H NMR spectrum of mTBPABOX. ^{1}H NMR ($CDCl_3$), ppm: δ= 1.52 (6H, s, germinal $2CH_3$), 2.22 (6H, s, aryl $2CH_3$), 4.57 (4H, s, -N-CH_2-Ar-), 5.36 (4H, s, -O-CH_2-N-), 6.81 (15H, m, aromatic)

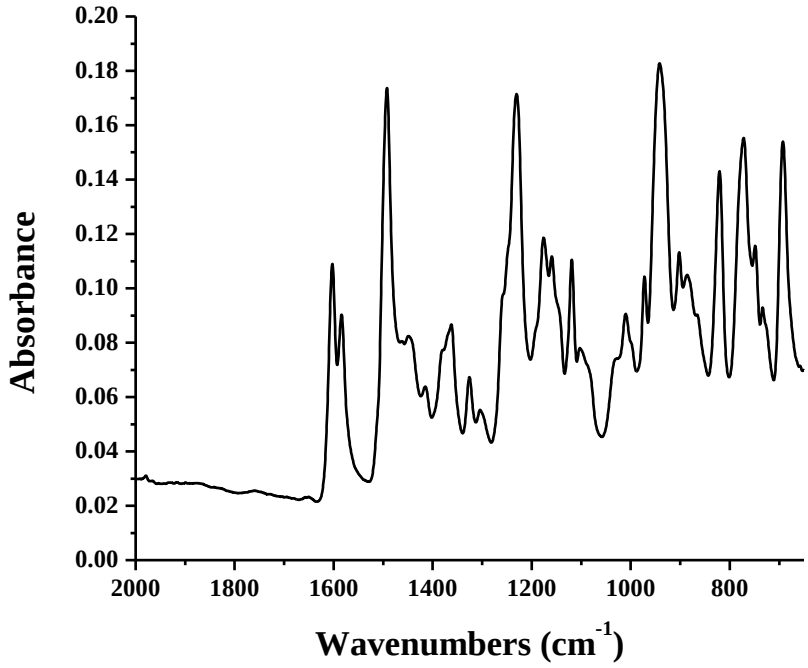

Figure A.20 ATR-FTIR spectrum of mTBPABOX-lab-scale CHSR. FTIR (KBr) v: Asymmetric stretching at 1230 cm^{-1} and symmetric stretching at 1175 cm^{-1} of ether bond in the BOX moiety, BOX moiety at 941 cm^{-1}, and tri-substituted benzene at 1492 and 821 cm^{-1}

REFERENCES

1. Strong, A. B., *Fundamentals of composites manufacturing : materials, methods and applications*. 2nd ed.; Society of Manufacturing Engineers: Dearborn, Mich., 2008; p xiii, 620 p.

2. Rimdusit, S.; Jongvisuttisun, P.; Jubsilp, C.; Tanthapanichakoon, W., *Journal of Applied Polymer Science* **2009,** *111* (3), 1225-1234.

3. Rimdusit, S.; Tiptipakorn, S.; Jubsilp, C.; Takeichi, T., *Reactive and Functional Polymers* **2013,** *73* (2), 369-380.

4. Wang, Y.-X.; Ishida, H., *Journal of Applied Polymer Science* **2002,** *86* (12), 2953-2966.

5. Allen, D. J.; Ishida, H., *Polymer* **2009,** *50* (2), 613-626.

6. Agag, T.; Geiger, S.; Alhassan, S. M.; Qutubuddin, S.; Ishida, H., *Macromolecules* **2010,** *43* (17), 7122-7127.

7. Holly, F. W.; Cope, A. C., *Journal of the American Chemical Society* **1944,** *66* (11), 1875-1879.

8. Higginbottom, H. P. Polymerizable compositions comprising polyamines and poly(dihydrobenzoxazines). 1988.

9. Higginbottom, H. P.; Drumm, M. F. Process for deposition of resin dispersions on metal substrates. 1988.

10. Burke, W. J.; Weatherbee, C., *Journal of the American Chemical Society* **1950,** *72* (10), 4691-4694.

11. Burke, W. J., *Journal of the American Chemical Society* **1949,** *71* (2), 609-612.

12. Burke, W. J.; Stephens, C. W., *Journal of the American Chemical Society* **1952,** *74* (6), 1518-1520.

13. Burke, W. J.; Bishop, J. L.; Glennie, E. L. M.; Bauer, W. N., *The Journal of Organic Chemistry* **1965,** *30* (10), 3423-3427.

14. Schreiber, H. 1973.

15. Schreiber, H. Polymeric resins derived from 1-oxa-3-aza tetraline group-containing compounds and cycloaliphatic epoxides. 1986.

16. Ning, X.; Ishida, H., *Journal of Polymer Science Part A: Polymer Chemistry* **1994,** *32* (6), 1121-1129.

17. Ishida, H. A., T, *Handbook of Benzoxazine Resins*. Elsevier: Amsterdam, 2011; Vol. 1.

18. Brunovska, Z.; Liu, J. P.; Ishida, H., *Macromolecular Chemistry and Physics* **1999,** *200* (7), 1745-1752.

19. Ward, S.; Harriman, M. Benzoxazines and Compositions Containing the Same. 2013.

20. Baranek, A. D. Design and synthesis of flexible and functional polybenzoxazine thin films. Ph.D., The University of Southern Mississippi, Ann Arbor, 2013.

21. Yeganeh, H., Chapter 21 - Polybenzoxazine/Polyurethane Alloys. In *Handbook of Benzoxazine Resins*, Agag, H. I., Ed. Elsevier: Amsterdam, 2011; pp 389-403.

22. Kimura, H.; Ohtsuka, K.; Matsumoto, A., Chapter 24 - Poly(Benzoxazine/Bisoxazoline). In *Handbook of Benzoxazine Resins*, Agag, H. I., Ed. Elsevier: Amsterdam, 2011; pp 429-441.

23. Zhang, C.; Wang, L.; Yu, R.; Zheng, S., Chapter 25 - Morphology and Properties of Polybenzoxazine Blends. In *Handbook of Benzoxazine Resins*, Agag, H. I., Ed. Elsevier: Amsterdam, 2011; pp 445-455.

24. Wunsche, A. German Patent 131,392. 1901.

25. Easton, R. W. British Patent 109,663. 1916.

26. Easton, R. W. U.S. Patent 1,468,379. 1923.

27. S.B. Brown, C. M. O., Reactive Extrusion. In *Encyclopedia of Polymer Science and Engineering*, John Wiley: New York, 1988; Vol. 14, p 169.

28. Xanthos, M., *Reactive extrusion : principles and practice*. Hanser Publishers ; Distributed in the USA and Canada by Oxford University Press: Munich ; New York New York, 1992; p xv, 304 p.

29. Prat, L.; N'Diaye, S.; Rigal, L.; Gourdon, C., *Chemical Engineering and Processing: Process Intensification* **2004,** *43* (7), 881-886.

30. Titier, C.; Pascault, J.-P.; Taha, M., *Journal of Applied Polymer Science* **1996,** *59* (3), 415-423.

31. Finnigan, B.; Martin, D.; Halley, P.; Truss, R.; Campbell, K., *Polymer* **2004,** *45* (7), 2249-2260.

32. Cai, C.; Shi, Q.; Li, L.; Zhu, L.; Yin, J., *Radiation Physics and Chemistry* **2008,** *77* (3), 370-372.

33. Shokoohi, S.; Arefazar, A.; Naderi, G., *Materials & Design* **2011,** *32* (3), 1697-1703.

34. Moad, G., *Progress in Polymer Science* **1999,** *24* (1), 81-142.

35. Andersen, P. G.; Lechner, F., *Proc. SPE* **2013**.

36. Fang, H.; Ma, X.; Feng, L.; Wang, K.; Cao, B., *APP Journal of Applied Polymer Science* **2008,** *108* (6), 3652-3661.

37. Tzoganakis, C., *Advances in Polymer Technology* **1989,** *9* (4), 321-330.

38. Ishida, H., Chapter 1 - Overview and Historical Background of Polybenzoxazine Research. In *Handbook of Benzoxazine Resins*, Agag, H. I., Ed. Elsevier: Amsterdam, 2011; pp 3-81.

39. Huang, M. T.; Ishida, H., *Polymers and Polymer Composites* **1999,** *7* (4), 233-247.

40. Jubsilp, C.; Takeichi, T.; Rimdusit, S., *Journal of Applied Polymer Science* **2007,** *104* (5), 2928-2938.

41. Shaw, D. E.; Deneroff, M. M.; Dror, R. O.; Kuskin, J. S.; Larson, R. H.; Salmon, J. K.; Young, C.; Batson, B.; Bowers, K. J.; Chao, J. C.; Eastwood, M. P.; Gagliardo, J.; Grossman, J. P.; Ho, C. R.; Ierardi, D. J.; Istv; #225; Kolossv, n.; #225; ry; Klepeis, J. L.; Layman, T.; McLeavey, C.; Moraes, M. A.; Mueller, R.; Priest, E. C.; Shan, Y.; Spengler, J.; Theobald, M.; Towles, B.; Wang, S. C., *Commun. ACM* **2008,** *51* (7), 91-97.

42. Gu, Y.; Li, M., Chapter 3 - Molecular Modeling. In *Handbook of Benzoxazine Resins*, Agag, H. I., Ed. Elsevier: Amsterdam, 2011; pp 103-110.

43. Hiemenz, P. C.; Lodge, T. P., *Polymer Chemistry, Second Edition*. CRC Press: 2007.

44. Ishida, H. Process for preparation of benzoxazine compounds in solventless systems. 1996.

45. Frazee, A. S.; Wiggins, J. S. Continuous High Shear Reactor Melt Processing Methods to Synthesize Heterocyclic Monomers and Compositions Thereof. 2015.

46. Ishida, H.; Liu, J.-P., Chapter 2 - Benzoxazine Chemistry in Solution and Melt. In *Handbook of Benzoxazine Resins*, Agag, H. I., Ed. Elsevier: Amsterdam, 2011; pp 85-102.

47. Zhang, H.; Lu, Z., *e-Polymers* **2010,** *10* (1), 1578-1586.

48. Anders, M.; Lo, J.; Centea, T.; Nutt, S., *SAMPE Journal* **2016,** *52*, 44-55.

49. Flory, P. J., *Polymer* **1979,** *20* (11), 1317-1320.

50. Callister, W. D.; Rethwisch, D. G., *Materials Science and Engineering: An Introduction, 8th Edition*. Wiley: 2009.

51. *Materials Studio*, Version 8.0; San Diego, CA, 2014.

52. Andersen, H. C., *The Journal of Chemical Physics* **1980,** *72* (4), 2384-2393.

53. Parrinello, M.; Rahman, A., *Journal of Applied Physics* **1981,** *52* (12), 7182-7190.

54. Leimkuhler, B.; Noorizadeh, E.; Theil, F., *Journal of Statistical Physics* **2009,** *135* (2), 261-277.

55. Patrone, P. N.; Dienstfrey, A.; Browning, A. R.; Tucker, S.; Christensen, S., *Polymer* **2016,** *87*, 246-259.

56. Gupta, J.; Nunes, C.; Jonnalagadda, S., *Molecular Pharmaceutics* **2013,** *10* (11), 4136-4145.

57. Li, C.; Strachan, A., *Journal of Polymer Science Part B: Polymer Physics* **2015,** *53* (2), 103-122.

58. Bicerano, J., *Prediction of polymer properties*. CRC Press: 2002.

59. Trewin, A., *Chromatographia* **2010,** *71* (1), 175-175.

60. Barker, J. A.; Henderson, D., *Reviews of Modern Physics* **1976,** *48* (4), 587-671.

61. Leach, A. R., *Molecular Modelling: Principles and Applications*. Prentice Hall: 2001.

62. Chandler, D., *Introduction to Modern Statistical Mechanics*. Oxford University Press: 1987.

63. Chandler, D.; Weeks, J. D.; Andersen, H. C., *Science* **1983,** *220* (4599), 787.

64. Rigby, D.; Roe, R.-J., *J. Chem. Phys. The Journal of Chemical Physics* **1988,** *89* (8), 5280.

65. Rigby, H. A.; Bunn, C. W., *Nature* **1949,** (164), 583-585.

66. Mahfud, R. A. S. SYNTHESIS, EVALUATION AND MOLECULAR DYNAMIC SIMULATIONS OF NOVEL ANIONIC POLMERIC SURFACTANTS BASED ON POLYBENZOXAZINES. Case Western Reserve University, 2014.

67. Ozisik, R.; Doruker, P.; Mattice, W. L.; von Meerwall, E. D., *Computational and Theoretical Polymer Science* **2000,** *10* (5), 411-418.

68. Li, T.; Raizen, M. G., *Annalen der Physik* **2013,** *525* (4), 281-295.

69. Boon, J. P., *Molecular hydrodynamics / Jean Pierre Boon, Sidney Yip*. McGraw-Hill: New York ; London, 1980.

70. Mason, T. G., *Rheologica Acta* **2000,** *39* (4), 371-378.

71. Einstein, A., *Ann. Phys* **1906,** *19* (2), 289-306.

72. Frenkel, D.; Smit, B., Chapter 4 - Molecular Dynamics Simulations. In *Understanding Molecular Simulation (Second Edition)*, Academic Press: San Diego, 2002; pp 63-107.

73. Fayos, R.; Bermejo, F. J.; Dawidowski, J.; Fischer, H. E.; González, M. A., *Physical Review Letters* **1996,** *77* (18), 3823-3826.

74. Lopes Jesus, A. J.; Rosado, M. T. S.; Leitão, M. L. P.; Redinha, J. S., *The Journal of Physical Chemistry A* **2003,** *107* (19), 3891-3897.

75. Toxvaerd, S., *Condensed Matter Physics* **2015,** *18* (1).

76. Arya, G., *The Journal of Physical Chemistry B* **2009,** *113* (48), 15760-15770.

77. Levenspiel, O., *Chemical reaction engineering*. 3rd ed.; Wiley: New York, 1999; p xvi, 668 p.

78. Martin, C., Twin Screw Extrusion for Pharmaceutical Processes. In *Melt Extrusion: Materials, Technology and Drug Product Design*, Repka, M. A.; Langley, N.; DiNunzio, J., Eds. Springer New York: New York, NY, 2013; pp 47-79.

79. Gesser;, H. D.; Emond;, H. H., *Chemical Kinetis, in G. Pannetier, P. Souchay (Eds.)*. Elsevier: New York, NY, 1967.

80. Yoon, K. J.; Carr, M. E.; Bagley, E. B., *Journal of Applied Polymer Science* **1992,** *45* (6), 1093-1100.

81. Liu, J. P. Ph.D. Thesis. Case Western Reserve Univrsity, Cleveland, OH.

82. Michaeli, W.; Grefenstein, A., *Advances in Polymer Technology* **1995,** *14* (4), 263-276.

83. Kye, H.; White, J. L., *Journal of Applied Polymer Science* **1994,** *52* (9), 1249-1262.

84. Moradiya, H.; Islam, M. T.; Woollam, G. R.; Slipper, I. J.; Halsey, S.; Snowden, M. J.; Douroumis, D., *Crystal Growth & Design* **2014,** *14* (1), 189-198.

85. Crawford, D. E., *Beilstein Journal of Organic Chemistry* **2017,** *13*, 65-75.

86. J, K.; T, T., Method for making polyetherimides. Google Patents: 1974.

87. Rauwendaal, C. J., *Polymer Engineering & Science* **1981,** *21* (16), 1092-1100.

88. Velez-Herrera, P.; Ishida, H., *Journal of Fluorine Chemistry* **2009,** *130* (6), 573-580.

89. Wu, J.; Xi, Y.; McCandless, G. T.; Xie, Y.; Menon, R.; Patel, Y.; Yang, D. J.; Iacono, S. T.; Novak, B. M., *Macromolecules* **2015,** *48* (17), 6087-6095.

90. Agag, T.; Jin, L.; Ishida, H., *Polymer* **2009,** *50* (25), 5940-5944.

91. Santhosh Kumar, K. S.; Reghunadhan Nair, C. P.; Ninan, K. N., *Thermochimica Acta* **2006,** *441* (2), 150-155.

92. Ručigaj, A.; Alič, B.; Krajnc, M.; Šebenik, U., *Express Polymer Letters* **2015,** *9* (7).

93. Guide, H. S., *Huntsman Corporation: Basel, Switzerland* **2009**.

94. Friedman, H. L., *Journal of Polymer Science Part C: Polymer Symposia* **1964,** *6* (1), 183-195.

95. Jubsilp, C.; Takeichi, T.; Rimdusit, S., Chapter 7 - Polymerization Kinetics. In *Handbook of Benzoxazine Resins*, Agag, H. I., Ed. Elsevier: Amsterdam, 2011; pp 157-174.

96. Dunkers, J.; Ishida, H., *Journal of Polymer Science Part A Polymer Chemistry* **1999,** *37* (13), 1913-1921.

97. Ranjith, S.; Thenmozhi, S.; Manikannan, R.; Muthusubramanian, S.; Subbiahpandi, A., *Acta Crystallographica Section E: Structure Reports Online* **2009,** *65* (Pt 3), o581-o581.

98. Kolanadiyil, S. N.; Minami, M.; Endo, T., *Macromolecules* **2017**.

99. Imai, Y.; Shibasaki, Y.; Takeuchi, H.; Park, K. H.; Kakimoto, M.-A., *High Performance Polymers* **2002,** *14* (3), 253-260.

100. Low, H. Y.; Ishida, H., *Journal of Polymer Science-B-Polymer Physics Edition* **1998,** *36* (11), 1935-1946.

101. Yee Low, H.; Ishida, H., *Polymer* **1999,** *40* (15), 4365-4376.

102. Laobuthee, A.; Chirachanchai, S.; Ishida, H.; Tashiro, K., *Journal of the American Chemical Society* **2001,** *123* (41), 9947-9955.

103. Chirachanchai, S.; Laobuthee, A.; Phongtamrug, S., *Journal of Heterocyclic Chemistry* **2009,** *46* (4), 714-721.

104. Liu, J.; Ishida, H., *Macromolecules* **2014,** *47* (16), 5682-5690.

105. Van Krevelen, D. W.; Te Nijenhuis, K., Chapter 13 - Mechanical Properties of Solid Polymers. In *Properties of Polymers (Fourth Edition)*, Elsevier: Amsterdam, 2009; pp 383-503.

106. Teng, H., *Applied Sciences* **2012,** *2* (2), 496.

107. Boufflet, P.; Han, Y.; Fei, Z.; Treat, N. D.; Li, R.; Smilgies, D.-M.; Stingelin, N.; Anthopoulos, T. D.; Heeney, M., *Advanced Functional Materials* **2015,** *25* (45), 7038-7048.

108. Fox, T. G., *J. Appl. Bull. Am. Phys. Soc.* **1956,** *1*, 123-128.

109. McNair, O. D.; Sparks, B. J.; Janisse, A. P.; Brent, D. P.; Patton, D. L.; Savin, D. A., *Macromolecules* **2013,** *46* (14), 5614-5621.

110. Moody, J. D.; VanDerveer, D.; Smith Jr, D. W.; Iacono, S. T., *Organic & Biomolecular Chemistry* **2011,** *9* (13), 4842-4849.

111. Alkorta, I.; Rozas, I.; Elguero, J., *Journal of Fluorine Chemistry* **2000,** *101* (2), 233-238.

112. O'Hagan, D., *Chemical Society Reviews* **2008,** *37* (2), 308-319.

113. Zhong, W.; Liang, J.; Hu, S.; Jiang, X.-F.; Ying, L.; Huang, F.; Yang, W.; Cao, Y., *Macromolecules* **2016,** *49* (16), 5806-5816.

114. Liu, Y.; Wang, R.; An, Q.; Su, X.; Li, C.; Shen, S.; Huo, G., *Macromolecular Chemistry and Physics* **2017,** *218* (15), 1700079-n/a.

115. Murray-Rust, P.; Stallings, W. C.; Monti, C. T.; Preston, R. K.; Glusker, J. P., *Journal of the American Chemical Society* **1983,** *105* (10), 3206-3214.

116. Dunitz, J. D.; Taylor, R., *Chemistry – A European Journal* **1997,** *3* (1), 89-98.

117. Takemura, H.; Kotoku, M.; Yasutake, M.; Shinmyozu, T., *European Journal of Organic Chemistry* **2004,** *2004* (9), 2019-2024.

118. Takemura, H.; Kaneko, M.; Sako, K.; Iwanaga, T., *New Journal of Chemistry* **2009,** *33* (10), 2004-2006.

119. Kwei, T. K., *Journal of Polymer Science: Polymer Letters Edition* **1984,** *22* (6), 307-313.

120. Misasi, J., **2015**.

121. Cukierman, S.; Halary, J.-L.; Monnerie, L., *Polymer Engineering & Science* **1991,** *31* (20), 1476-1482.

122. Starkweather, H. W., *Macromolecules* **1981,** *14* (5), 1277-1281.

123. Knowles, K. R. Effect of Chain Rigidity on Network Architecture and Deformation Behavior of Glassy Polymer Networks. Dissertation, University of Southern Mississippi, http://aquila.usm.edu/dissertations/1316, 2017.

124. Smith, M. B.; March, J., Aromatic Substitution, Electrophilic. In *March's Advanced Organic Chemistry*, John Wiley & Sons, Inc.: 2006; pp 657-751.

125. Mayr, A. E.; Cook, W. D.; Edward, G. H., *Polymer* **1998,** *39* (16), 3719-3724.

126. Donovan, B. R.; Ballenas, J. E.; Patton, D. L., *Macromolecules* **2016,** *49* (20), 7667-7675.